RICE UNIVERSITY

Ultra-short, Single-walled Carbon Nanotube Capsules for Diagnostic Imaging and Radiotherapy

by

Michael Lee Matson

A THESIS SUBMITTED
IN PARTIAL FULFILLMENT OF THE
REQUIREMENTS FOR THE DEGREE

Doctor of Philosophy

APPROVED, THESIS COMMITTEE:

Lon J. Wilson, Chair
Professor of Chemistry

Andrew R. Barron
Charles W. Duncan, Jr. –
Welch Chair of Chemistry and
Professor of Materials Science

Enrique V. Barrera
Professor of Mechanical Engineering
and Materials Science

HOUSTON, TEXAS
DECEMBER 2011

ABSTRACT

Ultra-short, Single-walled Carbon Nanotube Capsules for Diagnostic Imaging and Radiotherapy

by

Michael Lee Matson

This thesis is centered on the Gadonanotubes (GNTs), an ultra-high-performance magnetic resonance imaging (MRI) contrast agent material discovered in our laboratories in 2005. The GNTs are a new paradigm in MRI contrast agent design with small clusters of Gd^{3+} ions within ultra-short carbon nanocapsules (ca. 50 nm) cut from full-length single-walled carbon nanotubes. Here, the factors underlying the performance efficacy of the GNTs have been investigated for the first time by variable-field (-50,000 Oe to 50,000 Oe at 2K) and variable-temperature (2K to RT at 100 Oe) magnetic susceptibility measurements using a Magnetic Property Measurement System (MPMS, based on a SQUID magnetometer). Additionally, experiments focused on the effects of hydroxylation of the GNTs' exterior surface regarding water-solubility are examined. Finally, the use of the GNTs as potential replacements for traditional metal-chelating/sequestering agents is explored. More specifically, the internal Gd^{3+}-ion clusters of the GNTs have been radiolabeled: (1) with $^{153}Gd^{3+}$ ions to test Gd^{3+}-ion stability to simulated biological challenge, (2) with $^{225}Ac^{3+}$ ions to generate a new concept for a GNT-based agent for α-radiotherapy, and finally (3) with $^{64}Cu^{2+}$ ions to produce the first bimodal MRI/PET (PET = positron emission tomography) imaging agent derived from the GNTs.

DEDICATION

To Grandma Lamb for her love and encouragement.

ACKNOWLEDGMENTS

First, I would like to thank my committee members: Drs. Barron, Barrera, and Wilson for taking the time to help me through this process. Second, I would like to thank all the members of the Wilson research group who helped me over the past few years. Of special note: Keith, who has played the role of an experienced older brother, always ready for advice or a pick-me-up when the research dragged, Jey, who has been the most trustworthy friend I could ask for throughout all of grad school, Lees, my little sister in the lab who kept me focused despite numerous calls for my attention, and Brandon, who kept the youthful spirit alive in the lab and was the most capable undergraduate assistant a grad student could hope for. Next, I would like to thank all of my collaborators who helped these projects come together: Emilia Moroson, Ron Goldfarb, Eva Sevick, Ali Azhdarinia, Anna Moore, Mike Tweedle, Krishan Kumar, David Sheinberg, Carlos Villa, Jens Rosenberg, and Samuel Grant, to only list a few. Without the support of these outstanding scientists, none of my projects would have come to fruition. Next, I would like to thank my brothers and sisters at the Stafford Fire Department, and finally, I would like to thank my family who were a rock of support I could count on. Samantha, Morgan, and Coop, words cannot express my gratitude. I love you all.

Just for Fun:

At the "Center" of Nanotechnology

Dr. Curl (of Rice University) and Sir Kroto (now of Florida State University, then of University of Sussex) with the late Dr. Richard Errett Smalley (also of Rice University) who won the 1996 Nobel Prize in Chemistry for their "discovery of

buckminsterfullerene."

Pictured: Dr. Robert (Bob) Floyd Curl, Jr. (left) and Sir Harold (Harry) Walter Kroto (right).

Scrabble Dictionary

Currently, the scrabble dictionary does not recognize "nanotube" as a legitimate word. This needs to be changed!

Pictured: Words with Friends app denying submission of "nanotube" in play.

TABLE OF CONTENTS

LIST OF FIGURES

CHAPTER ONE

CHAPTER TWO

CHAPTER THREE

CHAPTER FOUR

APPENDIX VII: COPPER PROPERTIES

LIST OF TABLES

CHAPTER TWO

CHAPTER THREE

CHAPTER FOUR

APPENDIX III: GADOLINIUM PROPERTIES

APPENDIX IV: GADONANOTUBOLS

APPENDIX XI: 1.5 T AND 3.0 T MRI PHANTOM RAW DATA

APPENDIX X: RAW DATA FOR ^{124}I EXPERIMENT

PREFACE

I wish to preface this thesis by noting that much of the material included in the literature review found in Chapter One comes from a published review article [1] and book chapter [2] for which I am the first author.

CHAPTER ONE: INTRODUCTION

"If we can reduce the cost and improve the quality of medical technology through advances in nanotechnology, we can more widely address the medical conditions that are prevalent and reduce the level of human suffering."

~ Ralph Merkle, American Nanotechnologist

INTRODUCTION

One of the exciting trends in modern drug design is the merging of traditional diagnostics (drugs that define a disease state) and therapeutics (drugs that treat a disease state) into a new field of multi-functional platforms known as "theranostics."[3,4] This form of integrated medicine allows physicians the unique ability to diagnose disease while simultaneously monitor therapeutic response. Aside from saving the patient valuable time and money, the physician has the ability to customize the patient's treatment regimen based on diagnostic feedback.

Just as a compounding pharmacist uses a gelatin capsule to deliver multiple drugs unique to a specific patient, this thesis examines the continued development of ultra-short carbon nanotube capsules (US-tube nanocapsules) as nanoscale molecular capsules for medical imaging, specifically magnetic resonance imaging (MRI) and positron emission tomography (PET), as well as therapeutic agents (specifically, α-particle therapy).[5] Stemming from a single-walled carbon nanotube (SWNT) precursor, US-tube

nanocapsules maintain a bio-inert carbon exterior surface prime for chemical derivitization for biocompatibility and cellular targeting.[5-7] Furthermore, US-tube nanocapsules have shown ability to permeate cell membranes and accumulate within cells; this accrual will enhance efficacy of both diagnostic and therapeutic agents.[8] Finally, US-tube nanocapsules have previously been studied as diagnostic agents following the encapsulation of Gd^{3+} ions for MRI contrast enhancement, known as "Gadonanotubes" (GNTs),[9] and I_2 *(s)* for X-ray Computed Tomography (CT) contrast enhancement,[10] as well as therapeutic agents through encapsulation of ^{211}AtCl for α-radionuclide therapy.[11] For these reasons, the US-tube nanocapsules have potential for becoming the platform from which numerous future theranostic agents can be constructed.

This thesis explores the US-tube nanocapsules in further detail: specifically, the magnetic properties of the nanocapsules loaded with lanthanide ions, attempts at hydroxylation of the nanocapsules' exterior, retention studies of both lanthanide ions and actinide ions, and their ability to encapsulate both Gd^{3+} and Cu^{2+} ions to prove useful as a bimodal MRI/PET imaging agent.

CARBON NANOSTRUCTURES

Definition

This chapter begins with an overview of carbon nanostructures, such as the US-tube nanocapsules, that exhibit the unique properties explored in this thesis. First, a proper

definition for nanotechnology must be established, as the media and popular culture commonly fails to properly define the term. For example, the web-based collaborative Wikipedia defines nanotechnology as: "Nanotechnology (sometimes shortened to "nanotech") is the study of manipulating matter on an atomic and molecular scale."[12] For the scope of this thesis, however, the following definition for Nanotechnology will be utilized: "the study of any man-made device or material, with at least one dimension under 100 nm, which exhibits unique or enhanced properties made possible by the nanoscale size."[1] This definition is employed as it more accurately confines the field of chemistry into what is (or is not) classified as "nanotechnology;" the more general definition of simply manipulating matter on a molecular scale would categorize almost all chemistry as nanotechnology. This added distinction of "unique or enhanced properties" offered by carbon nanotubes will be revisited multiple times throughout this thesis.

Fullerenes

Although fullerenes (**Figure 1**) are not a focus of this thesis, they are introduced here for three primary reasons:

(1) fullerenes are a natural, chronological introduction to carbon nanotubes due to similar synthetic pathways.

(2) endohedral metalofullerenes are used as sources of comparison to the GNTs in **Chapters Two** and **Appendix IV**.

(3) fullerenes were discovered (here) at Rice University in 1985.[13]

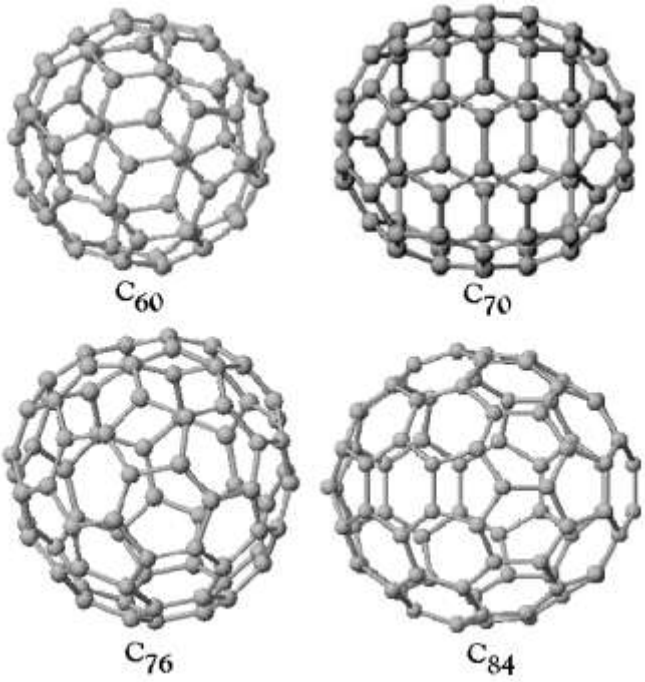

Figure 1: Representative fullerene molecules (adapted from [2]).

While traditional modeling of fullerenes renders beautiful structures (**Figure 1**), traditional naming regimens aren't as attractive. For example, following the systematic naming of the International Union of Pure and Applied Chemistry (IUPAC) Rule A-32 for bridged, cyclic hydrocarbons (also known as the von Baeyer System) renders C_{60} (**Figure 1 upper-left**) as:[14]

> *Hentriacontacyclo[29.29.0.0.^{2,14}.0^{3,12}.0^{4,59}.0^{5,10}.0^{6,58}.0^{7,55}.0^{8,53}.0^{9,21}.0^{11,20}.0^{13,18}.0^{15,30} .0^{16,28}.0^{17,25}.0^{19,24}.0^{22,52}.0$^{23.50}$.0^{26,49}.0^{27,47}.0^{29,45}.0^{32,44}.0^{33,60}.0^{34,57}.0^{35,43}.0^{36,56}.0^{37,41}.0^{38,54} .0^{39,51}.0^{40,48}.0^{42,46}]hexaconta-1,3,5(10),6,8,11,13(18),14,16,19,21,23,25,27,29(45), 30,32(44),33, 35(43),36,38(54),39(51),40(48),41,46,49,52,55,57,59-triacontaene.*

Luckily, the discovers of C_{60} offered a more eloquent name that is still in use today: "buckminsterfullerene."[13] Named after the American architect who popularized the geodesic dome in the 1960's (**Figure 2**),[15] buckminsterfullerene ("buckyball" for short) is traditionally reserved specifically for the C_{60} molecule. "Fullerenes" is now commonly

used to describe the entire class of closed cage molecules consisting of only three coordinate carbon atoms.[16,17] Fullerene classification is further guided by Euler's theorem, which states that for a closed structure to be purely composed from pentagons and hexagons, it must contain twelve pentagons. This limits the smallest fullerene to a C_{20} structure and renders C_{60} the smallest stable fullerene according to the Isolated Pentagon Rule (IPR), which states the most stable fullerenes have pentagons that do not contact each other.

Figure 2: The Montréal Biosphère by Buckminster Fuller for the 1967 International and Universal Exposition (Open-Source from [18]).

Synthesis of Fullerenes

Fullerenes have been discovered both in naturally-occurring carbon-rich rocks like shungite of Shunga, Russia,[19] and following powerful, geological events like wild fires along the K-T boundary in New Zealand,[20] lightning strikes,[21] and meteor strikes.[22] However, despite their natural existence, it wasn't until the mid-1980's that they were first discovered by a collaborative team of scientists at Rice University.[13]

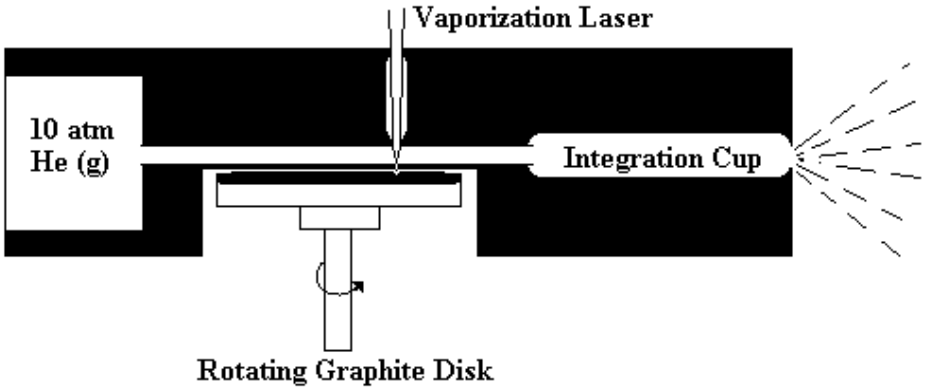

Figure 3: Schematic diagram of the pulsed supersonic nozzle used to produce fullerenes (adapted from [13]).

The original synthesis of C_{60} focused a pulsed neodymium-doped yttrium aluminum garnet (Nd:YAG) laser on a solid disk of graphite under high-density helium gas flow,[13] as shown in **Figure 3**. Collaboration between Profs. Richard Smalley and Bob Curl and the astrophysicist Prof. Harry Kroto of Sussex University began, using this technology to recreate the atmosphere of early red stars in an attempt to identify and better understand their unique infrared (IR) emission.[13,16,23] From the resulting soot from this experiment, fullerenes (C_{60}/C_{70}) were discovered. Later, scientists determined that lanthanum ions (La^{3+}) atoms could be entrapped inside of these fullerenes by doping the graphite disk with La salts,[24] creating a new material known as metallofullerenes (denoted La@C_{60}). The gadofullerenes (Gd@C_{60}) discussed later in this chapter are another form of lanthanide-ion-based metallofullerenes.

Macroscopic quantities of fullerenes were first generated using resistive heating between two graphite rods in a Krätschmer arc reactor.[25] Simply applying a voltage between these two rods produced fullerene-enriched (~4% C_{60}/C_{70}) carbon soot. Modified to use an arc welder with alternating current (AC) as a power supply, the Wudl reactor,[26] also known

as a "contact-arc" apparatus,[16] is the most commonly used resistive heating method use in the laboratory for its ease of construction and relatively low cost.[27] The primary alternative to the Wudl reactor in a laboratory setting is the arc-discharge technique, a similar technique which separates the carbon rods by a 4 mm fixed gap to allow an electric arc to form.[28] Other methods of fullerene synthesis include: solar furnaces,[29] hydrocarbon pyrolysis,[30] inductive heating,[31] coalescence reactions,[32] the combustion synthesis method,[33] and even simply lighting candles.[34]

Single-walled Carbon Nanotubes

An arc-discharge apparatus, similar to the one used for fullerene synthesis, also synthesizes hollow, cylindrical structures that resemble a single sheet of graphene rolled up seamlessly into a tube.[35-37] These structures, as shown in **Figure 4**, are called single-walled carbon nanotubes (SWNTs). With a high aspect ratio and large surface area, SWNTs possess interesting optical, mechanical, electrical and thermal properties.[38-42] This section will briefly describe: (A) the synthetic techniques used on the precursor SWNTs utilized within this thesis, (B) the various techniques used to purify these materials, and (C) the multiple available SWNT-characterization methods available.

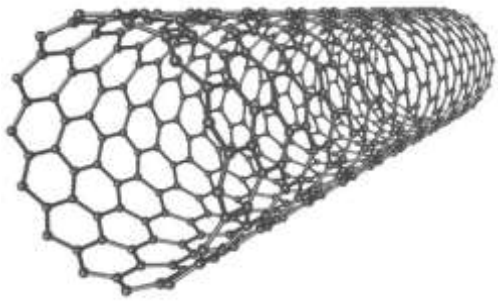

Figure 4: Ball-and-stick model of a single-walled carbon nanotube (SWNT) (adapted from [2]).

Syntheses of SWNTs

This thesis utilizes SWNTs manufactured by three unique methods: (1) electric arc-discharge (2) chemical vapor deposition (CVD), and (3) the high-pressure carbon monoxide process (HiP_{CO}). The laser ablation method used for fullerene production in the section above is also commonly used for SWNT production, yet not analyzed within this thesis.[43-45] Each of these methods yields SWNTs of varying dimensions and chiralities (a term used to describe the chiral vector that represents how the SWNT is oriented relative to an infinite graphene sheet as shown in **Figure 5**).

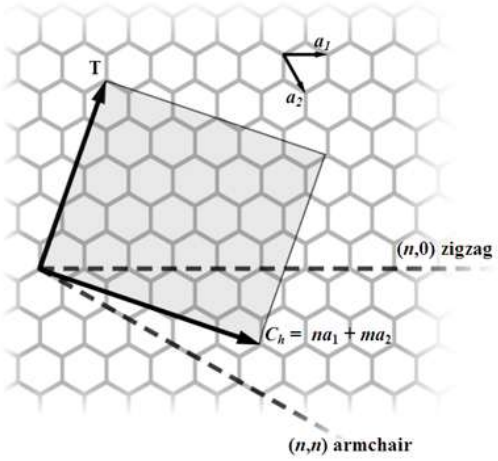

Figure 5: Diagram representing SWNT chirality using the (*n,m*) naming scheme. T represents the axis of the SWNT, *n* and *m* are the chiral indices that make up the C_h vector, and a_1 and a_2 are unit vectors (public domain from [46]).

The first reported technique for the synthesis of SWNTs was the electric arc-discharge technique.[36,47] Small quantities of metal particles (Fe, Co, etc) at the cathode of the arc results in the synthesis of SWNTs, multi-walled carbon nanotubes (MWNTs),[35] and fullerenes. The vaporization of metal atoms into the gas phase stabilizes the elongating fullerene structures in the vapor phase resulting in SWNT production.[47] Advancements in the use of mixed-metal catalysts such as Co-Ni, Co-Pt, Ni-Y, and Ni-CO results have

resulted in significant improvement in yield and purity of SWNTs produced by this process.[48]

SWNTs can also be synthesized using a CVD technique known as CoMoCat® by SouthWest NanoTechnologies Inc., shown in **Figure 6**. CoMoCat® derives its name from its use of cobalt-molybdenum (Co-Mo) catalyst particles for the Boudouard disproportionation reaction of CO feed stock:[49,50]

$$2\ CO\ (g) \rightarrow 2\ CO_2\ (g)\ +\ C\ (s)$$

This technique is a continuous-flow technique, as opposed to a "batch method,"[51-53] which allows an ease of scalability that in turns lowers the cost significantly. Molybdenum trioxide (MoO_3) stabilizes the Co^{2+} ion for reaction with eventual reduction by the CO. Following the reduction, the nanoscale clusters of now metallic Co (under 2.0 nm) act as the catalyst for SWNT growth.

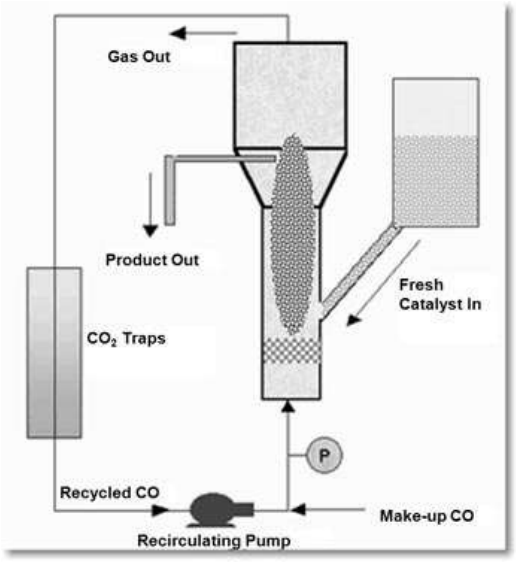

Figure 6: CoMoCat® fluidized bed SWNT reactor (adapted from [54]).

Finally, studies found within this thesis also employ SWNTs produced by the HiP_{CO} process, made on Rice's campus in the reactor shown in **Figure 7**. Like in the CoMoCAT® process, CO is the feed stock; however, HiP_{CO} uses iron pentacarbonyl ($Fe(CO)_5$) as catalyst.[55,56] This method produces SWNTs in high yield (>90 %) with high purity (no amorphous carbon coating).

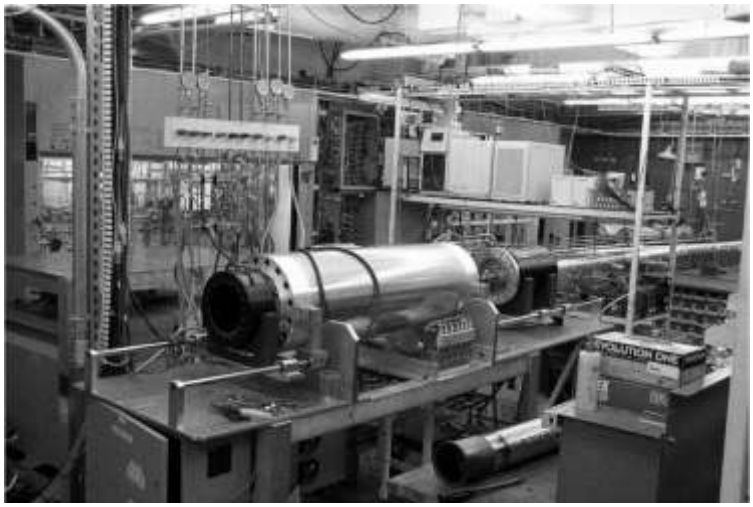

Figure 7: HiP_{CO} SWNT reactor at Rice University.

In summary, the three precursor SWNTs used throughout this thesis are: (1) Arc-produced SWNTs, (2) CoMoCAT® produced SWNTs, and (3) HiP_{CO} produced SWNTs. Of these, unless specifically noted otherwise, the SWNTs will be Arc-produced as these were the most cost-effective form of SWNTs available. Perhaps the most significant difference between these techniques for the scope of this thesis is their average internal diameter: 0.8 nm for HiPCO-produced SWNTs, 1.0 nm for CoMoCAT-produced SWNTs, and 1.4 nm for electric-arc-produced SWNTs (Ni:Y catalyst). This thesis will demonstrate that this key difference is negligible for the projects herein; however, future works, as described in **Chapter 5**, will likely show bias towards HiP_{CO} synthesized tubes.

The smaller diameter of HiP_{CO}-produced SWNTs results in greater structural strain,[57] which correlates to more facile functionalization routes of the US-tube nanocapsules sidewalls. This feature will become important when functionalizing the US-tube nanocapsules with medical targeting moieties in the future.

Purification of SWNTs

To remove the metal catalyst nanoparticles and amorphous carbon impurities of the produced SWNTs, numerous purification techniques have been employed including: hydrothermal treatment,[58,59] microfiltration and chromatographic separation,[60-63] inorganic nanoparticles purification,[64-66] and gas-phase oxidative procedures.[57,67-69] The purification of large batches of SWNTs was first reported by oxidation in strong acids (3-5 M nitric acid).[70] Many reports have been published since with different temperatures, reaction times and acid conditions.[71] These oxidizing agents convert metal catalyst particles into their corresponding metal oxides, which are larger in volume than their metal counterparts. This results in the disruption of the carbon sheath surrounding the metal particles and the subsequent leaching of metal catalyst impurities.[72] Along with the metal catalyst particles, the oxidation process also removes a majority of the carbonaceous impurities. The relative chemical inertness of SWNT materials permits much harsher oxidation conditions than are tolerated by other carbonaceous materials such as fullerenes, graphitic shells, and amorphous carbon. For biomedical applications, the presence of carbonaceous impurities and metal catalyst particles will result in undesirable inhomogenity and potential metal-mediated toxicity, respectively.[73,74] Acid treatment was the purification method employed throughout this thesis for arc-ablation-

synthesized and CoMoCAT-synthesized SWNTs.

A special situation is encountered with HiP_{CO} SWNTs due to their increased reactivity. To account for this situation, a purification protocol involving liquid Br_2 has been shown to be very effective in removing the metal catalytic impurities from HiPco SWNTs without compromising their sidewall structure.[75] This technique was used exclusively for the purification of HiPco SWNTs within this thesis.

Characterization of SWNTs

Common analytical techniques for the characterization of SWNTs include: Raman spectroscopy, near infrared (NIR) spectroscopy, thermal gravimetric analysis (TGA), and electron microscopy techniques (TEM, SEM, etc.).

SWNTs have four signature peaks in the Raman spectrum useful for characterization,[57,76,77] as shown in **Figure 8**: (1) The radial breathing mode (RBM) (150-300 cm^{-1}, diameter dependent) gives information about the diameter and packing of the SWNTs. (2) The tangential mode (G-band; from 1515 cm^{-1} to 1590 cm^{-1}) gives information about the sp^2-hybridized carbons and can be useful in determining purity. (3) The disorder mode (D-band; from 1280 cm^{-1} to 1320 cm^{-1}) is a measure of the sidewall defects, amorphous carbon, and degree of functionalization, etc. (4) The G' mode is the second overtone of the D-band, yet has a name that stems from being the second strongest peak in graphite. As this mode is diameter dependent, it is most often used to examine SWNT sample diameter.

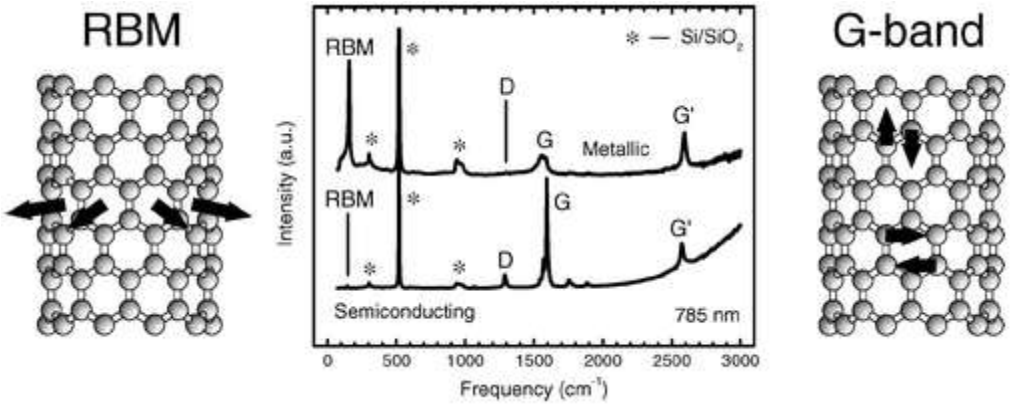

Figure 8: Representative Raman spectra for SWNTs. Shown are characteristic spectra for both metallic and semiconducting HiPCO-produced SWNTs using a 785 nm laser excitation. Inserts on left and right represent atomic displacement occurring from vibration modes (adapted from [78]).

NIR spectroscopy can also been used to characterize SWNT materials.[79,80] Metallic and semiconducting SWNTs can be separately identified,[81] and this technique can also be used to check for functionalization as functionalized SWNTs do not fluoresce in the NIR region. This loss of fluorescence is due to a disruption of the SWNT electronic structure; the same is true for the US-tube capsules described below, therefore NIR won't be employed within this thesis.

TGA is one of the most widely used methods to check for the purity and the extent of functionalization, since carbonaceous materials and organic substituents decompose at a lower temperature than SWNTs. However, TGA cannot differentiate between different forms of carbonaceous materials such as amorphous carbon and organic functional groups. Hence, quantification of functional groups by TGA depends on the pre-functionalization purity of SWNT materials and the use of other characterization methods, as well. Other techniques, such as X-ray photoelectron spectroscopy (XPS) and

nuclear magnetic resonance (NMR) spectroscopy, can also be used to identify functional groups covalently attached to SWNTs.[7] Microscopy techniques such as transmission electron microscopy (TEM), scanning electron microscopy (SEM) and atomic force microscopy (AFM) have been widely used for the visualization of SWNT materials to study their structural properties. However, electron microscopy techniques use a small, localized fraction of the sample, and hence, such measurements have to be repeated multiple times at different sampling sites to generalize the observation.

US-TUBE NANOCAPSULES

Introduction

The overarching scope of this thesis involves the ability for ultra-short SWNTs (US-tubes nanocapsules, **Figure 9**) to encapsulate medically-active ions; therefore, a brief introduction to this modified-SWNT material is required. Numerous techniques have been utilized for the shortening of SWNTs, including applying a voltage pulse to the tip of a scanning tunneling microscope (STM);[82,83] fluorination followed by oxidation with piranha and ammonium persulfate solutions;[84] and treatment with oleum (100% H_2SO_4 with excess SO_3) and nitric acid.[85,86] Herein, we cut SWNTs into US-tube nanocapsules of 20-80 nm in length by fluorination followed by pyrolysis at 1000 °C in an inert Ar atmosphere.[5] A more detailed synthesis is described below**.**

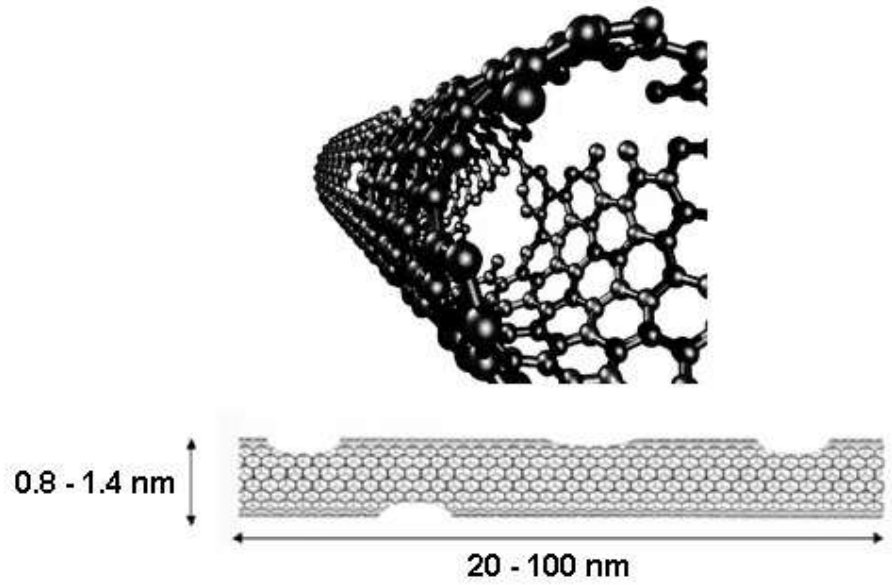

Figure 9: Pictorial representations of US-tube nanocapsules.

The synthesis of this material is included in this "background" chapter for two reasons: (1) the US-tube nanocapsules are used in every chapter of the thesis, and (2) it should be clearly noted that this synthesis is not a unique contribution, but rather a well-established prcoedure. Three separate apparatus for the fluorination of SWNTs were used within this thesis (two are displayed in **Figure 10**, while the third was owned by a private corporation, Nanoridge Materials). Optimizing the conditions of each instrument renders a final material, in all cases, that behave similarly to one another. Also, it should be noted that electric-arc-synthesized and CoMoCAT-synthesized SWNTs behaved identically in the three fluorinating apparatus, while more reactive HiP_{CO} SWNTs required less reaction time (in all three apparatus) to have the same fluorination effect.

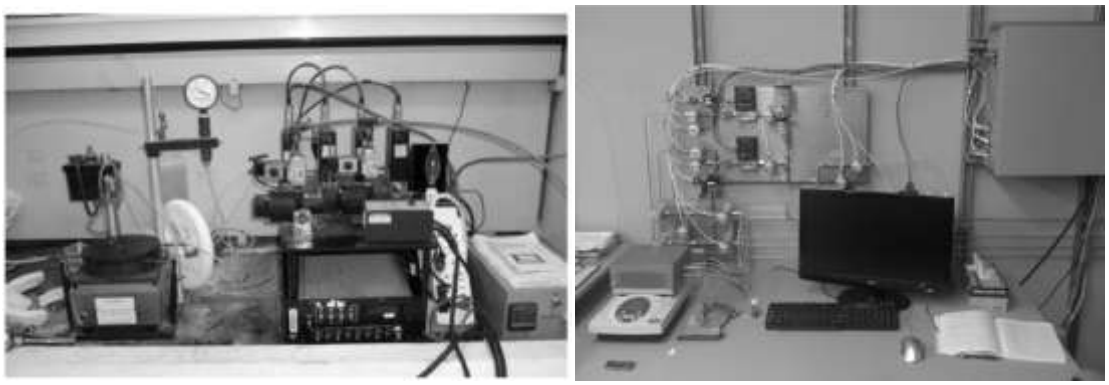

Figure 10: Example fluorination apparatus. Left is the custom fluorination built by the late Prof. Margrave, and right is the current fluorination apparatus at Rice named the John L. Margrave Fluorination Facility in honor of Prof. Margrave.

Synthesis of US-Tube Nanocapsules

US-tube nanocapsules were prepared following previously-established synthetic methods (**Figure 11A→B**).[5] This synthesis will follow the conditions optimized for the John L. Margrave Fluorination Facility at Rice University for two commercially-available SWNT materials: CoMoCat® SWNTs (SWeNT® CG200 Grade, SouthWest NanoTechnologies Inc., Norman, OK) and electric-arc discharge SWNTs with Ni/Y catalyst (AP Grade, CarboLex, Inc., Lexington, Kentucky). To determine the protocol for fluorination of HiP_{CO} SWNTs in the reactor, simply decrease the reaction time by 40%.

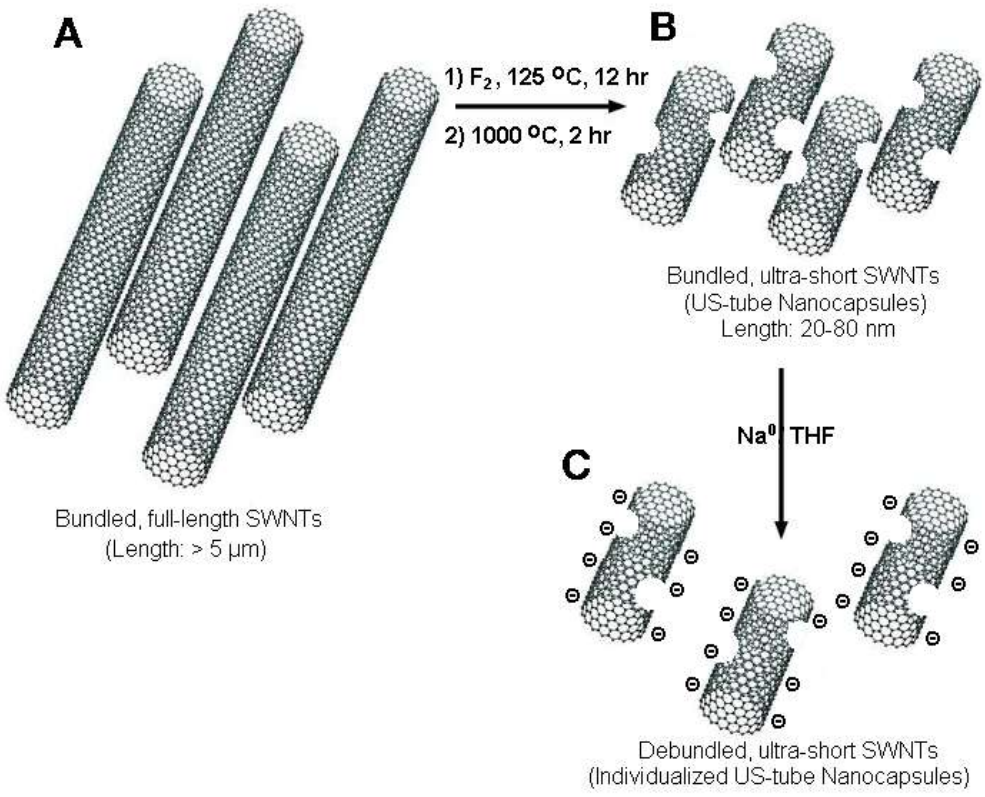

Figure 11: Synthesis of US-tube nanocapsules.

US-tube nanocapsules were prepared following the literature fluorination/pyrolysis method.[5,87,88] Approximately 1.0 g of raw, full-length SWNTs was split between two Monel boats and inserted into a fluorination apparatus (**Figure 10**). After purging the system with He gas for 45 minutes while raising the system temperature to 125 ^{o}C, the SWNTs were exposed to a fluorinating gas mixture (2.7% argon-diluted F_2) at 125 °C for 12 hr (7 hr for HiP_{CO} SWNTs). SWNTs synthesized from electric arc ablation techniques were predominantly used in this thesis for their relatively large diameter (1.3-1.5 nm),[9] a property originally hypothesized to be important when considering loading potential (capacity for internalization). Once the system was allowed to return to room temperature and all unreacted F_2 gas has purged the system, fluorination was confirmed

via weight increase (approximately 25-30%) and increase in the relative intensity ratio of the Disordered Mode peak around 1300 cm^{-1} (representative of sp^3-hybridised carbon) to the G-Band Mode around 1590 cm^{-1} (representative of sp^2-hybridised carbon), known as the D:G ratio, using Raman spectroscopy.[89]

A Renishaw Raman microscope using a 633 nm excitation laser employing an 1800 l/mm grating, available through Rice's Shared Equipment Authority (SEA), was utilized for collection of Raman spectra. All spectra were obtained on oven-dried samples that were mounted on a glass microscope slide using double-sided tape. Once the sp^2-hybridized carbon atoms of the carbon nanotube sheath become sp^3-hybridized when bound to fluorine, a visible shift occurs in the resulting Raman spectra. The proposed mechanism for this fluorination reaction is a (1,4) addition.[90] Moreover, the higher deformation energy of separating the fluorine attachments to the SWNT sheath provide an energetically-favored condition of forming banded structures,[90] which original scanning tunneling microscope (STM) images support, as shown in **Figure 12**.

Figure 12: STM image of a carbon nanotube fluorinated at 250°C for 12 h (bright areas represent fluorine atoms, 860 Å by 180 Å, adapted from [91]).

Immediately following removal from the reactor (to prevent unwanted dehalogenation), the fluorinated SWNTs were heated to 1000 ^oC in a tube furnace under inert argon gas for 3 hr. Cutting is made possible due to the fluorine deposition occurring in a banded

structure (**Figure 12)**, circling the nanotube and leaving approximately 20-80 nm of relatively unfunctionalized nanotube between these bands. Volatile fluorocarbons, in the form of carbon tetrafluoride (CF_4) and carbonyl fluoride (COF_2), are driven off the tubes rendering US-tubes approximately 20-80 nm in length (**Figure 11B**).[9,11,92] The few fluorine depositions along these US-tube nanocapsule segments, however, result in defect sites in the US-tube nanocapsule sidewalls that will facilitate the loading ions and small molecules.[93] Successful pyrolysis is confirmed via weight decrease (approximately 33%) and a large decrease in the D/G ratio using a Renishaw Raman microscope. This decrease occurs as many of the sp^3-hybridized carbons left the US-tube nanocapsules in the form of volatile fluorocarbons as described above.

Removal of metal catalyst impurities occurs via bath sonication in 100 mL of concentrated HCl for one hour.[35] These purified US-tube nanocapsules are gravity-filtered using a coarse ('C') fritted glass filter, being washed several times with 150 mL aliquots of HPLC grade deionized water until the pH of the filtrate becomes ~7.0. Finally, these tubes will be left in an 80 ^{o}C oven to dry overnight. The removal of catalyst is confirmed via SEA's Phi Quantera X-ray Photoelectron Spectroscopy (XPS) spectrometer, as well as weight loss.

Debundling of US-tube Nanocapsules

These purified US-tube nanocapsules must be debundled to maximize the surface area allowing for a maximum loading of payload. Due to strong van der Waals interactions between these US-tube nanocapsules, a force of approximately 0.5 eV exists for every

nanometer of full-length carbon nanotube.[74] These US-tube nanocapsules will be debundled following chemical Birch reduction using sodium metal in tetrahydrofuran (THF).[7] The US-tube nanocapsules are be added to dry, distilled THF with an equal mass of Na^0 at a maximum of 60.0 mg of US-tube nanocapsules. Following one hour of bath sonication, the reaction will be quenched by the addition of deionized (DI) water. The US-tube nanocapsules are washed following the same filtration and drying method used for the purification. Debundling of the resulting US-tube nanocapsules is confirmed via a Digital Instruments IIIa Nanoscope Atomic Force Microscopy (AFM) instrument. Individualized US-tubes, or nanocapsules, should show lengths from 20-80 nm and a height ca. 1.2-1.6 nm, as shown in **Figure 13**.

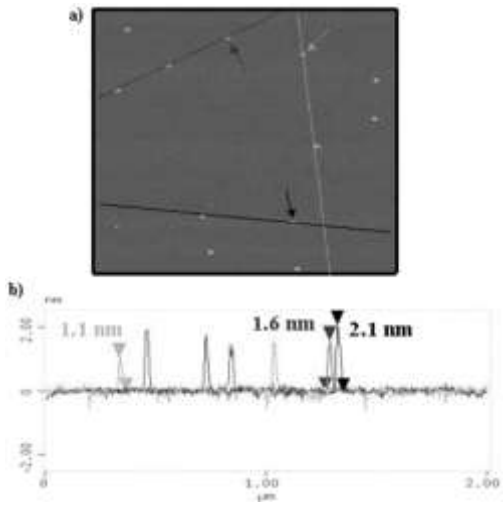

Figure 13. Atomic Force Microscopy data for US-tube nanocapsules. **(a)** An AFM height image of nanocapsules. **(b)** *z*-scan resolution height analysis of (a). (adapted from [7]).

This debundling process is very important for the US-tube nanocapsules for *in vivo* applications as they have been shown to safely escape the reticuloendothelial system and be excreted through the kidneys and bile ducts in mouse models.[74] Additionally, US-tube

nanocapsules display neither fibrinous deposits nor ascite retention within peritoneal cavities. Finally, the US-tube nanocapsules show no acute toxicity *in vivo.*[74]

THESIS SUMMARY

This main body of this thesis is subdivided into three primary chapters that revolve around the US-tube nanocapsules previously described. The first of these chapters focuses on the magnetic properties that underlie the high-performance efficacy of the GNTs (an MRI contrast agent based upon the US-tube nanocapsules). The second of these chapters examines the stability of the Gd^{3+}-ion clusters of the GNTs under simulated physiological challenges utilizing the radionuclide ^{153}Gd. Additionally, this chapter explores the synthesis of GNTs with embedded $^{225}Ac^{3+}$ ions as a new, highly-potent α-radiotherapy agent. The final chapter investigates the use $^{64}Cu^{2+}$ ions to produce the first bimodal MRI/PET imaging agent derived from the GNTs, the ^{64}Cuprogadonanotubes (^{64}CuGNTs).

CHAPTER TWO: MAGNETIC PROPERTIES OF GADONANOTUBES

"Oh no! Not the magnet!!!"

~ Bender Bending Rodriguez of *Futurama*

INTRODUCTION

The main purpose of **Chapter Two** is to examine the magnetic properties of the Gadonanotubes (US-tube nanocapsules with internalized Gd^{3+} ions, GNTs, **Figure 14**):

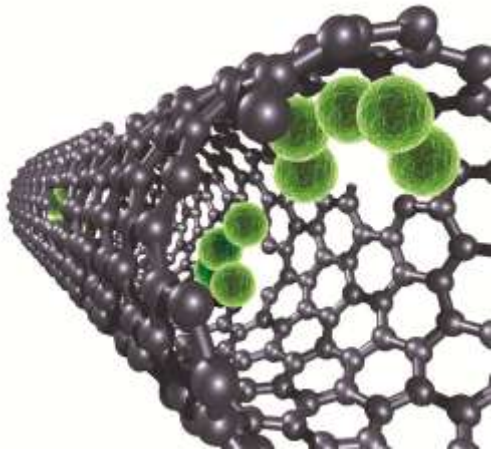

Figure 14: Pictorial representation of a Gadonanotube. Green spheres represent Gd^{3+} ions, drawn roughly to scale (anions omitted for clarity).

An in-depth examination of the magnetic state of both the nanoscale catalyst particles of SWNTs and the internalized Gd^{3+} ions of the GNTs using a Magnetic Property Measurement System (MPMS) based on a Superconducting Quantum Interference Device (SQUID) magnetometer was required. The GNTs were originally characterized as being superparamagnetic, and it was proposed that their high-performance contrast agent (CA) capability was related to superparamagnetic Gd^{3+}-ion clusters within US-

tubes.[9] The originally reported GNTs were derived from single-walled carbon nanotubes (SWNTs) produced by an electric-arc discharge process.[48] The studies reported herein include US-tubes nanocapsules (as described in **Chapter 1**) derived from both SWNTs produced by the high-pressure carbon monoxide process (HiP_{CO}) and electric-arc discharge process (Arc), GNTs from each precursor, and lutetium (Lu^{3+}) analogs of the GNTs (Lutetonanotubes, or LNTs). Lu^{3+} ion was selected as it has identical solution chemistry to Gd^{3+} solutions, yet is diamagnetic. Ultimately, the GNTs were determined to be a system comprised of two separate magnetic contributions: (1) a diamagnetic carbon nanotube sheath with remnant nanoscale metal catalyst particles that are superparamagnetic, resulting in a superparamagnetic US-tube nanocapsule and (2) paramagnetic Gd^{3+}-ion clusters within the nanocapsule. These contributions are displayed pictorially in **Figure 15**:

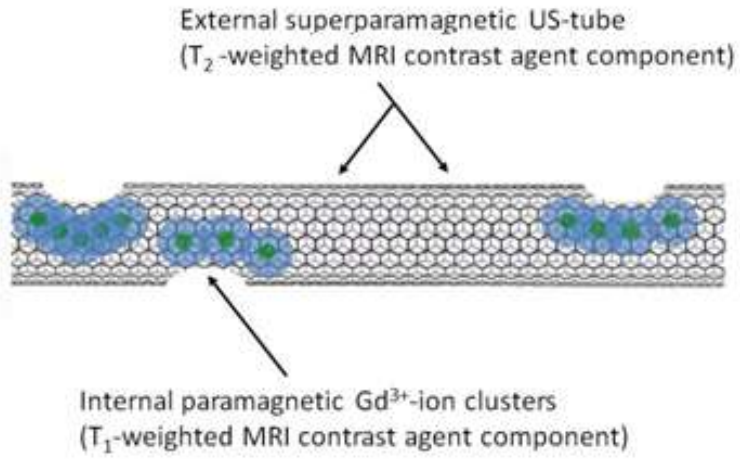

Figure 15. Magnetic contributions to the Gadonanotubes.

BACKGROUND INFORMATION

Prior to introducing this chapter's study on the magnetic properties of US-tube nanocapsules, GNTs, and LNTs, this section describes critical background information on the fundamental properties of magnetic resonance imaging (MRI), as well as provides a description of CAs with similar properties compared to the GNTs and a short synopsis of the magnetic properties that will be discussed further throughout the chapter.

Magnetic Resonance Imaging

First, this section briefly introduces to the physical properties that underlie an MRI scanner, as well as clarifies the key distinctions between T_1- and T_2-weighted images, as the GNTs are a unique, simultaneous mixture of both a T_1 and a T_2 CA.

Introduction to MRI

Physicians cannot always diagnosis a patient purely by the signs and symptoms the patient presents. Visualization of a patient's internal structures is often required to determine appropriate treatment strategies and follow-up therapies. MRI has proven to be an effective diagnostic tool used by physicians around the world for this visualization. MRI evolved from the principles of Nuclear Magnetic Resonance (NMR) and essentially images water within the human body, a great target for imaging considering human fat-free body weight (FFWW) contains 73.2% water.[94] Clinical MRI scanners use strong homogenous magnetic fields to align proton spins found in a patient, perturb these spins using specific radio frequency (RF) pulse sequences dependent on the strength of the

instrument's magnet, and measure the time it takes the spins to equilibrate, a process known as relaxation,[95] as shown in **Figure 16**:

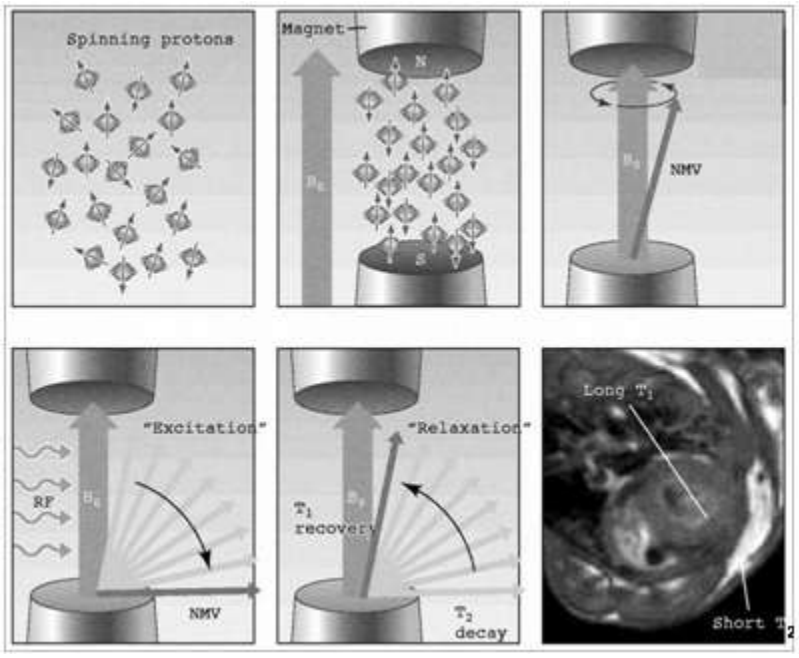

Figure 16: Fundamental MRI Principles (adapted from [96]).

Mathematical algorithms filter the relaxation data, apply tomographic reconstruction, and finally render a grayscale image. With spatial resolution under 100 μm in preclinical systems and 1 mm in human subjects,[97] MRI has advanced beyond even high-resolution computed tomography's (CT's) 2-3 mm clinical resolution without the need for Röntgen equivalents (rem) of ionizing radiation. More importantly, MRI has the advantage of enhanced contrast resolution, allowing superior soft tissue contrast. Additionally, MRI has a wider diagnostic range of detection than most other medical imaging modalities, allowing for both physiological and metabolic studies.[98] Finally, MRI is effectively a multimodal diagnostic within itself. By viewing a proton spin as a vector comprised of

both longitudinal and transverse components, MRI has the capability to measure the relaxation time of each individual component, T_1 and T_2 respectively.

MRI Fundamentals

MRI is based on NMR principles that earned Drs. Felix Block and Edward Mills Purcell the Nobel Prize in Physics for 1952. In short, an external magnetic field (B_0) used in MRI aligns the wealth of randomly-oriented nuclear spin of water protons in human body in a process known as excitation that ultimately creates a current in sensitive detector coils.[96] This excitation results in a Boltzmann distribution of low-energy spins parallel to the field and high-energy spins anti-parallel to the field.[99] The low-energy state dominates, and the summation of the individual nuclear spins results in a net magnetization vector (NMV). This NMV precess around B_0 at a frequency known as the Larmor frequency (ω), given by the expression:

$$\omega = \gamma B_0$$

where γ is the gyromagnetic ratio specific for hydrogen (please note, γ will also be used to describe γ radiation in **Chapters 3 and 4**).

An external radiofrequency (RF) pulse equal to ω (known as the resonant frequency) is applied in a direction perpendicular to the B_0 and causes the NMV to goes from being aligned with B_0 to the being perpendicular to B_0. The process by which these nuclear spins return to the Boltzman distribution prior to perturbment by the RF pulse is known as relaxation. This process is subdivided into spin-lattice (T_1) and spin-spin (T_2) relaxation. T_1 relaxation is a process by which the NMV returns to alignment with B_0 by

releasing the energy obtained from the RF pulse to the surrounding lattice. The time required for this relaxation to occur (T_1) is dependent upon the mobility of the surrounding lattice (lattices of higher mobility cause a longer T_1). Fluids have the longest T_1, followed by water-based tissue, fat-based tissue, and finally solids, respectively. In a 1.5 T clinical MRI scanner, subcutaneous fat will have a T_1 of approximately 343 ms, nearly four times faster than the more mobile tissue of the uterus with a T_1 of approximately 1,309 ms.[100]

While T_1 relaxation focuses on the return to status quo, T_2 relaxation concentrates on the process of decoherence of the nuclear spins that compose the NMV. Immediately following the RF pulse, the nuclear spins have instantaneous phase coherence, yet local interactions with neighboring nuclear spins (hence 'spin-spin') and fluctuations in the local magnetic field cause the nuclear spins to gradually dephase. The time required for this perpendicular magnetization to relax is denoted as T_2. Since every tissue in the body has its own T_1 and T_2, radiologists can choose specific instrument parameters that will create resultant MRI scans which depend predominantly on only one of the two relaxation times; T_1–weighted images cause areas of short T_1 to appear bright, while T_2–weighted images cause areas of short T_2 to appear dark. T_2–weighted images are often used for physiological studies such as fluids (blood plasma, cerebrospinal fluid, etc) since the fluid will appear hyperintense compared to surrounding tissues. The application of the physics of NMR to biomedical imaging has been so important to the field of medicine, that Drs. Paul C. Lauterbur and Peter Mansfield were jointly awarded a Nobel Prize, the 2003 Nobel Prize in Medicine, for their work with MRI.

MRI Contrast Agents

Next, a brief introduction of both T_1 and T_2 MRI CAs, the units of comparison of MRI CA efficacy known as relaxivity, Gd^{3+}-ion-based CAs in current clinical use, and two novel Gd^{3+}-ion-containing, carbon-based nanostructures: the gadofullerenes and the GNTs is presented.

Introduction

MRI alone can yield insufficient diagnosis when cancerous tissue resembles surrounding tissue, such as gliomas,[101] brain metastasis,[102] meningiomas,[103,104] and pituitary tumors.[105] For enhanced image contrast, radiologists use passive CAs, such as paramagnetic $MnCl_2$ and toxic Gd^{3+} ion safely chelated or encapsulated within bio-inert molecules,[95,106-108] as well as superparamagnetic CAs like small particles of iron oxide (SPIO).[109] Of the 27.5 million MRI procedures performed annually in the United States, 43% used a CA as part of the imaging procedure.[110] CAs in conventional radiography provide a direct effect; for example, radiocontrast agents used in computed tomography will directly scatter photons due to their high electron density. The CAs used for MRI, however, provide indirect contrast by altering the T_1 and T_2 of nuclei in close proximity.[111]

Paramagnetic CAs, or CAs that only display magnetic properties when a magnetic field is introduced, cause a decrease in both the T_1 and the T_2 of surrounding protons. This results in a whiter spot on longitudinal MRI scans (T_1-weighted scans) and a darkening on transverse scans (T_2-weighted scans). Conversely, ferromagnetic materials, or magnetic materials that retain magnetic polarization after the magnetic field is removed, will cause

a "dramatic decrease" in T_2 values, yet have little effect on T_1 values.[112] Finally, a special magnetic state occurs when ferromagnetic materials exist as isolated, single domain nanoparticles. While still retaining 'magnetic memory,' these materials can actually misalign with the magnetic field due to thermal fluctuations, causing them to behave like paramagnetic materials. This special state is known as superparamagnetism and, like ferromagnetism, can cause a significant decrease in T_2 values while having little effect on T_1 values. Generally physicians prefer T_1 CAs, as it easier to distinguish features in a brightened image versus a darkened image.

Unpaired electrons have magnetic dipoles 650 times larger than those of unpaired protons (hydrogen nuclei), so ionic transition metals with a large number of unpaired electrons are the most obvious candidates for MRI contrast enhancement. Of all T_1 CAs, chelated Gd^{3+}-ion compounds are by far the most-widely used in clinical practice due to the gadolinium ion's seven unpaired electrons, making it the most paramagnetic, stable metal ion known (**Table 1**). Additionally, this helps contribute to the large intrinsic magnetic moment of the Gd^{3+} ion and long electron spin-relaxation time (the time electron spins will jointly stay aligned with the magnetic field).

The problem that originally arose, however, with using Gd^{3+} ion as a CA is its toxicity:

> "These metals are moderately to highly toxic. The symptoms of toxicity of the rare earth elements include writhing, ataxia, labored respiration, walking on the toes with arched back and sedation. The rare earth elements exhibit low toxicity by ingestion exposure. However, the intraperitoneal route is highly toxic while the subcutaneous route is poison to moderately toxic." ~ Gadolinium Nitride (GdN) MSDS

For this reason, chemical chelating agents were designed to sequester the toxic Gd^{3+} ions (discussed in greater detail in **Chapter 3**).

Table 1: Electronic configuration and corresponding magnetic moment data for selected paramagnetic ions (adapted from[95]).

Atomic N	Ion	3d	4f	Magnetic moment (Bohr magneton)
24	Cr 3+			3.8
25	Mn 2+	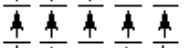		5.9 (weak field)
26	Fe 3+			5.9 (weak field)
29	Cu 2+	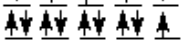		1.7-2.2
63	Eu 3+			(6.9)
64	Gd 3+			7.9
66	Dy 3+			(5.9)

Relaxivity

To compare the concentration-dependent efficacies of CAs, a standard known as "relaxivity" (units: $mM^{-1}s^{-1}$) is used, with typical values around 4 $mM^{-1}s^{-1}$ for commercially available CAs at 37 ^{o}C (physiological temperature) and 1.5 Tesla field strength (standard for many clinical MRI instruments).[113] A relaxivity value, *r*, is derived from the following relationship:

$$\frac{1}{Ti,\ \text{observed}} = \frac{1}{Ti,\ \text{solvent}} + r_i\,[M^{n+}],\ i = 1, 2$$

where $[M^{n+}]$ corresponds to the molar concentration of metal ion (mmol/L).[114] Relaxivity is also dependent on the magnetic field strength and temperature, so most calculations of $r_{1,2}$ values are reported holding these parameters constant at 1.5 T and 37 °C, respectively. Higher relaxivity values for a CA increases the relative contrast offered per unit of CA, thus lowering the dose required for imaging. A lower dose, in turn, increases patient safety. Moreover, CAs with much improved $r_{1,2}$ values are required for cellular

and molecular imaging applications.[115,116]

MRI CAs on the nanoscale have a twofold advantage: (1) nanoscale materials have a large surface-area-to-volume ratio and (2) nanoscale materials are small enough to cross cell membranes to allow for an accumulation of a CA within cells. Firstly, since relaxation enhancement occurs at the surface of MRI CAs, having a larger surface area to volume ratio equates to potentially higher-performance. Higher performance CAs can conceivably decrease dose (and, hence, toxicity risks) and costs.[117] Moreover, cell internalization of MRI CAs can allow for imaging of intracellular processes and for magnetic cell labeling, important roles for both *in vitro* cell separation and *in vivo* cell tracking studies.[118]

The highest recorded relaxivity at clinical field strength (1.5 T) and a temperature of 40 ^{o}C is found with the GNTs at a value of 170 $mM^{-1}s^{-1}$.[9] By this measure, the GNTs dramatically outperform current Gd^{3+}-ion-based clinical agents at 4.3 $mM^{-1}s^{-1}$ for Magnevist and 3.6 $mM^{-1}s^{-1}$ for Prohance under similar conditions.[108] The difference in T_1- weighted contrast that occurs between Gd-DTPA (Magnevist) and the GNTs can be seen in **Figure 17.** These record values are likely caused, in part, by the fast flow rate of water through a carbon nanotube.[119] The US-tube nanocapsules have proven an effective T_2 agent as well.[120] The combination of Gd^{3+} ions and superparamagnetic clustering, therefore, develops the GNTs into a CA capable of enhancing both T_1- and T_2-weighted images.[121]

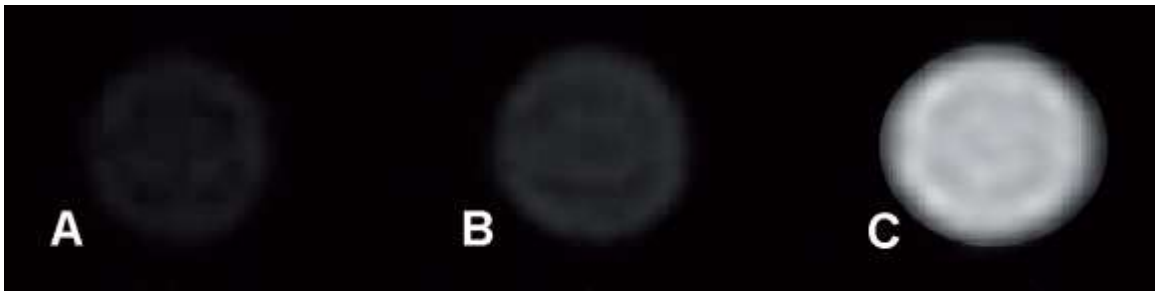

Figure 17. T_1-weighted MRI phantoms of (A) DI water, (B) Gd-DTPA (Magnevist™) and (C) the GNTs obtained using a 1.5 T Philips MR imager. $[Gd^{3+}]$ = 0.04 mM for B and C (adapted from [122]).

Relaxation can arise between a CA to surrounding water molecules through two primary mechanisms: (A) an inner-sphere mechanism where water molecules bond directly to the metal ion causing a direct proton relaxation or (B) an outer-sphere mechanism where the random translation diffusion of water protons surrounding the CA, though not directly bound to the metal ion, cause indirect proton relaxation.

Gadolinium

Gd^{3+} ion is the most common metal ion used for MRI CA design, because it contains the greatest number of unpaired *f* electrons (seven) and the electrons are distributed symmetrically about the atom.[114] This distribution results in a symmetrical electronic ground state and a favorably long electron-spin relaxation time. Moreover, the magnetic moment (μ) of the Gd^{3+} ion is:

$$\mu^2 = 63\mu_B^2$$

where μ_B is the Bohr magneton (a solitary electron magnetic dipole moment).[114] For these reasons, the Gd^{3+} ion provides appreciable relaxivity; however, the aquated Gd^{3+} ion is extremely toxic (see "Gadolinium Toxicity" in **Chapter 3** for more information).

Because of this toxicity, Gd^{3+} ion requires chelation or encapsulation to sequester its toxicity for *in vivo* use, with encapsulation usually being a preferred method as it completely prevents dissociation of the metal ion *in vivo.*

Chelated Gd^{3+} ions traditionally decrease the relaxation times of surrounding water protons through a combination of both inner- and outer-sphere mechanisms.[123] Inner-sphere proton relaxation mechanisms involve bonding of water molecules to the Gd^{3+} ion. No direct binding of water to Gd^{3+} ion is needed for an outer-sphere relaxation mechanism.

Gadofullerenes (GFs)

Leading to the discovery of the GNTs was another potential MRI CA based on carbonaceous nanomaterials, endohedral gadofullerenes (Gd^{3+}-ion-containing fullerene cages, or GFs).[1] Note: for the remainder of this thesis, the @ symbol will represent "within;" therefore $Gd@C_{60}$ would represent a Gd atom within a fullerene molecule. Only a week after C_{60}'s discovery, the same laboratory determined that a single lanthanide ion could be trapped within the fullerene's hollow interior.[24] GFs are synthesized by soaking carbon rods in Gd^{3+}-ion salt solutions prior to carbon-arc ablation. The Gd atoms donate three electrons to the electronegative carbon cage to become trivalent (Gd^{3+}) ions, resulting in electron spin density on the fullerene surface.

The encapsulated Gd^{3+} ion in GFs can only act through an outer-sphere mechanism as the carbon cage prevents any direct bonding of the Gd^{3+} ion with surrounding water

molecules. Despite lacking an inner-sphere mechanism, water-solubilized GFs ($Gd@C_{60}[C(COOH)_2]_{10}$ and $Gd@C_{60}(OH)_x$) have proven to be significantly more efficacious than current clinically-approved CAs (relaxivity values approaching 20 fold greater).[124] The paramagnetic carbon cage of a water-soluble GF molecule causes simultaneous relaxation of many water molecules on its surface resulting in the largest outer-sphere relaxation process of any known Gd^{3+}-ion-based CA, likely owed to the large, paramagnetic surface area-to-volume ratio.[125]

Nuclear Magnetic Relaxation Dispersion (NMRD) measurements are valuable for determining relaxation mechanisms and dynamic processes influencing MRI CA relaxivity. The classical Solomon, Bloembergen and Morgan (SBM) theory of proton relaxation only fits the GF CA NMRD profile when treating the GFs as slow tumbling molecules in solution.[123,126] Water-solubilized GFs exhibit a rotational tumbling time in nanoseconds (1.2 ns). The NMRD profile of GFs at different temperatures has shown that the molecular tumbling rate is most likely the relaxivity-limiting step.[125] Relaxivity of the GFs is also influenced by pH, with a decreasing pH causing an increase in relaxivity. Theoretically, a decrease in pH causes an increase in the aggregate size; an increase in aggregate size slows the tumbling time.[125]

Relaxivity of the GFs is also affected by salt concentration.[123] High salt concentration breaks up GF aggregates, which results in faster tumbling times. This disaggregation is dependent not only on the ionic strength of the solution, but also on salts with hydrogen bonding capacity such as phosphate.

GFs have been effectively used for magnetically labeling of cells. Specifically, anionic $Gd@C_{60}[C(COOH)_2]_{10}$ reduced the T_1 of labeled mesenchymal stem cells (MSC) and NIH3T3 cells to allow for distinct differentiation between labeled and unlabeled cells.[127] Additionally, a special class of GFs known as Hydrochalarones, a surface-modified $Gd_3N@C_{80}$ containing three Gd^{3+} ions bound to a central nitride ion,[128-130] have demonstrated *in vivo* tolerance and provided excellent MRI enhancement.[131]

Although GFs seem attractive agents for contrast enhancement in MRI, difficulties with synthesis such as poor yields and complicated steps of purification have not yet been successfully overcome, making gadofullerenes unlikely candidates for widespread clinical use in the near future.

Gadonanotubes (GNTs)

The fluorination/pyrolysis cutting process used prepare US-tube nanocapsules results in defect sites in the sidewalls of the US-tubes that can allow internalization of both small molecules and ions.[9-11] Gd^{3+} ions are internalized within US-tube nanocapsules as clusters of less than ten Gd^{3+} ions as confirmed by TEM.[9] The darkly-contrasted areas in the TEM were analyzed using energy dispersive X-ray spectroscopy (EDS) and shown to be electron-rich Gd^{3+}-ion clusters. These Gd^{3+}-ion doped US-tube nanocapsules are denoted as gadonanotubes (GNTs, **Figures 14 and 15**). Both the US-tube nanocapsules and the subsequent GNTs have been shown to be superparamagnetic from superconducting quantum interference device (SQUID) measurements.[9,121]

Relaxometry studies reveal that GNTs have efficacies 40 times larger than any current clinically-approved MRI CA.[9,122] The r_1 values of GNTs have been reported as high as 174 mM^{-1} s^{-1} per Gd^{3+} ion at 60 MHz and 37 ^{o}C. For comparison: the relaxivity values for GFs range between 20 - 100 mM^{-1} s^{-1} and commercially-available Magnevist™ (Gd-DTPA) is ca. 4 mM^{-1} s^{-1} under the same conditions.[9] Furthermore, the GNTs produce an MR signal intensity about 200 times greater than Magnevist™ for the same Gd^{3+}-ion concentration in T_1-weighted MRI images (**Figure 16**). Finally, the GNTs show a remarkable dependence on pH and exhibit exceedingly high relaxivities at physiologically-relevant pH. GNT relaxivity values nearly double from pH 7.4 to 7.0 (65 $mM^{-1}s^{-1}$ to 105 $mM^{-1}s^{-1}$) and nearly triple from pH 7.4 to 6.7.[132] This pH-sensitivity could potentially detect small, metastasized cancerous lesions, as tumors have a lower pH ($\leq$ 0.5 pH units) in their immediate vicinity compared to normal tissue.[133]

In an attempt to understand the mechanisms involved in proton relaxation occurring for GNTs, an NMRD study was performed.[134] The shape of the resulting NMRD plot, however, is unlike that of any other reported CA. The SBM theory of paramagnetic relaxation used to explain the GFs has not proven successful at modeling the GNTs. This is likely due to nanoscale confinement of the naked/aquated Gd^{3+}-ion clusters within the GNTs complimented by the ballistic flow of water in-and-out of the sidewall defects and through the Gd^{3+}-ion clusters.[135] Another Nanotechnology effect occurs because of the nanoscale catalyst particles within the US-tube nanocapsules which renders excellent T_2-weighted MRI CAs (with or without Gd^{3+} ions!).[121] Theoretically, the T_1-enhancing Gd^{3+}-ion clusters combined with the external, T_2-enhancing US-tube nanocapsule creates

an MRI CA capable of dual-weighted MR imaging enhancement.

Moreover, the unparalleled relaxivity values for the GNTs at both current clinical and lower field strengths make the GNTs attractive materials for a universal MRI CA. The GNTs show fairly constant relaxivities at various high-field strengths, which may provide a major advantage for GNTs as higher-field MRI continues to gain popularity in clinical settings.[136] Additionally, the GNTs exceptionally good performance at very low field-strengths, as required for microtesla imaging, may help overcome the poor signal-to-noise ratio characteristic of low-field imaging.[137,138]

The exterior carbon surface of the US-tube nanocapsules can further be functionalized for water solubility and biocompatibility.[10,139] Various moieties (water-solubilizing agents, biocompatible coverings, antibodies, peptides, etc.) can be attached to the external surface of the US-tube nanocapsules for active targeting of specific cell types. For example, cyclic RGD, a peptide sequence noted for selective binding to metastatic cancer cells,[140] has been covalently attached to GNT sidewalls.[141] Similar to lipophilic, water-soluble GFs,[127] water-soluble GNTs (specifically, GNTs covalently functionalized with DL-serine) readily cross cell membranes and accumulate inside cells.[142] This accumulation allows for the possibility of both molecular MR imaging and magnetic cell labeling for *in vivo* cellular trafficking.

Magnetism

This section introduces the properties of magnetism; specifically, the units and methods of measurement, the types of magnetism commonly encountered, including diamagnetism, paramagnetism, ordered magnetism, and a special type of magnetism, superparamagnetism, that arises from nanoscale magnetic domains.

Units

A short note on the units used in **Chapter 2:** while the rest of this thesis will use Système international (SI) units, this chapter uses Gaussian centimeter, gram, second (CGS) units to describe magnetism (**Table 2).**[143]

Table 2. Magnetic terms, units, and conversion factors.[143]

Term	Symbol	SI Unit	CGS Unit	Conversion Factor
Magnetic induction	B	Tesla (T)	Gauss (G)	$1\ T = 10^4\ G$
Magnetic field	H	A/m	Oersted (Oe)	$1\ A/m = 4\pi/10^3\ Oe$
Magnetization	M	A/m	emu/cm^3	$1\ A/m = 10^{-3}\ emu/cm^3$
Permeability of free space	μ_0	H/m	dimensionless	$4\pi \times 10^{-7}\ H/m = 1$

The reason that CGS units have been selected primarily stems from the values the Magnetic Property Measument System (MPMS) reports: CGS units of emu (electromagnetic units). Additionally, the unique relationship between M (magnetization), H (magnetic field), and B (magnetic induction):

$$B = \mu_0 (H+M) \qquad [SI]$$

$$B = H + 4\pi M \qquad [CGS]$$

where μ_0 is the permeability of free space with a value of $4\pi \times 10^{-7}$ H/m in SI units and a value of unity in CGS units. For this reason, when using CGS units, B and H values (but

not units) can be used interchangeably; this is not true for SI units.[143] For example:

0.5 Gauss = 50 μT [B fields]

0.5 Oe = 39.8 A/m [H fields]

Magnetic Measurements

A better understanding of the magnetophysics of the GNTs should help understand the source of the the amazing relaxivity values the GNTs possess as an MRI CA. For the scope of this thesis, two primary magnetic measurements will be employed on the MPMS: (1) magnetization as a function of temperature or M(T) and (2) magnetization as function of the applied magnetic field or M(H).[144] An M(T) measurement is made by fixing the value of H; similarly, an M(H) measurement is made by fixing the temperature. If the M(H) curve is linear, a useful quantity known as magnetic susceptibility (or the measure of magnetization of a material in response to the applied magnetic field, χ) can be determined for the material with:

$$\chi = \frac{M}{H}$$

Types of Magnetism

Though an oversimplification, for the scope of this thesis one can consider three main types of magnetism: diamagnetism, paramagnetism, and ordered magnetism. Diamagnets are repelled by a magnetic field, and almost all materials contain some inherent diamagnetism resulting from paired electrons. A negative χ (or a reversible M(H) plot with a negative, linear slope) is indicative of a paramagnetic material. Conversely, a positive χ (or a reversible M(H) plot with a negative, linear slope) is indicative of a paramagnetic material. While there are numerous other forms of paramagnetism (Curie-

Weiss, Pauli, Van Vleck, etc.), this thesis will examine simple paramagnetic materials that obey the Curie law:

$$\chi = \frac{C}{T}$$

where C is a constant known as the Curie constant. Using this, plotting inverse susceptibility ($1/\chi$) vs T will result with a linear plot of slope 1/C passing through the origin (0 K).

The other forms of magnetism include materials that have long-range magnetic ordering, specifically ferromagnetism, ferrimagnetism, and antiferromagnetism. Ferromagnets are the strongest magnetic materials and are noted for their lack of magnetic reversibility known more commonly as magnetic hysteresis (**Figure 18**):

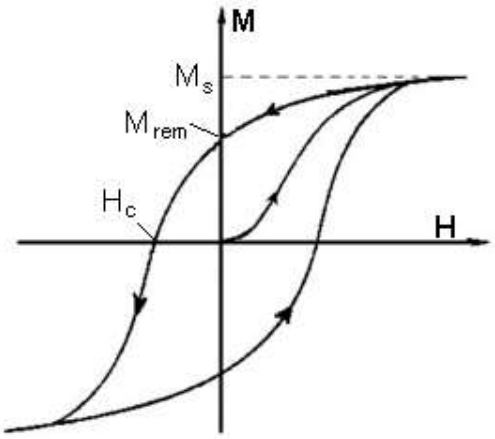

Figure 18. Example magnetic hysteresis loop. M(H) at a fixed field below the Curie temperature, M_S = saturation magnetization, M_{rem} = remnant magnetization, and H_C = coercive force. The curve within the loop is known as the virgin curve.

Hysteresis loops will form below a ferromagnetic sample's Curie point (temperature where a ferromagnet becomes paramagnetic on heating) due to the ferromagnetic

domains attempting to minimize the energy of the system.[145,146] Starting at the origin in **Figure 18**, as H is increased, the corresponding M increases to a maximum known as the saturation magnetization (M_S); the curve leading to the M_S is known as the virgin curve, and is often omitted as little useful information is rendered aside from showing that the measurements started with no remnant magnetization (M_{rem}). M_{rem} refers to the amount of magnetization remaining in the material after removing H, and the amount of H in the reverse direction required to return the materials net M to zero is known as the coercive force/field or H_C. It is also important to note that this magnetic hysteresis will only occur for a ferromagnet below a critical temperature known as the Curie temperature, T_C. Above this temperature, the material will display paramagnetic behavior; below this temperature, all of the magnetic moments are aligned in the same direction, as shown in **Figure 19**.

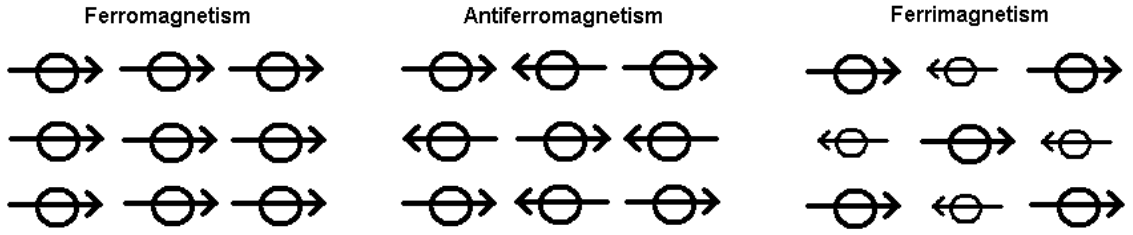

Figure 19. Schematic representation of magnetic moments of ordered magnetic states.

If, however, the magnetic moments align so adjacent moments are in opposite directions (canceling out the net M), the material is known as antiferromagnetic. Similiarly, if the opposite orientation of antiferromagnetism is followed using magnetic moments of differing magnitude, the material is said to be ferrimagnetic.

Superparamagnetism

If a ferromagnetic particle becomes small enough, thermal energy can overcome the sample domains' anisotropy energy, first described by Néel in 1949.[147] At this point, the particles themselves begin to behave like a single domain as the thermal energy overcomes the benefits of maintaining domains:

$$E = KV \sin^2\theta$$

where K is the anisotropy energy density, V is the volume of the particle, and θ is the angle between the M and the sample domain's easy axis (magnetic anisotropy creates easy and hard directions of M, with a strong preference for alignment with the easy axis). Once the value of KV becomes small enough, thermal energy fluctuations can overcome E. This will result in spontaneous changes in the magnetization of a sample, which will resemble a paramagnet. The only key difference is that the displayed paramagnetism is seen for thousands of atoms making up the sample particle, and not an isolated atom, hence the term *super*paramagnetism.

MATERIALS AND METHODS

This section describes the materials and methods used for the synthesis of GNTs and LNTs, as well as the instrumentation and data analysis sequences utilized to gather the magnetic properties and relaxivity measurements of the resulting materials.

GNTs and Lutetium Analogs

The GNTs (Gd^{3+} is paramagnetic) and their lutetium analogs (the Lutetonanotubes, LNTs, note: Lu^{3+} is diamagnetic) were synthesized using the previously published protocol for GNTs.[148] Individualized US-tube nanocapsules (synthesis discussed in detail in **Chapter 1**) were loaded with either Gd^{3+} ions or Lu^{3+} ions using a simple aqueous loading method. Two different precursors were utilized for the study: (a) SWNTs produced using the electric-arc discharge technique (Arc) with a Y-Ni alloy as catalyst (Carbolex Inc.) and (b) SWNTs produced using the high-pressure carbon monoxide method (HiP_{CO}) with Fe as catalyst (Rice University). The materials as purchased (Raw) were further purified from metal catalyst particles through bath sonication in concentrated HCl *(aq)* and liquid bromine treatment under N_2 *(g)* for Arc and HiPCO tubes, respectively.

Briefly, 100 mg of US-tubes were added to 100 mL of aqueous 5.0 mM $GdCl_3$ or 5.0 mM $LuCl_3$ solution prepared with HPLC-grade water (1 mg of US-tube nanocapsules/mL solution, pH = 2.5) and bath sonicated for 60 minutes. The solution was allowed to settle overnight. The lanthanide-ion-loaded US-tubes flocculated at the bottom and were washed with HPLC-grade water (pH = 7.0) over a coarse fritted-glass filter until the filtrate showed no detectible levels (< 1 ppb) of lanthanide ion as determined by inductively-coupled plasma mass spectrometry (ICP-MS) (experimentally determined to be 8 washings of 150 mL of HPLC-grade water).

Samples were removed from the coarse fritted-glass filter via pipette aspiration with

HPLC-grade water, collected on a watch glass, and dried overnight in an 80 ^{o}C oven. The dried samples were then collected; catalyst and encapsulated lanthanide metal percentages were determined using ICP-MS.

Hydroxylated GNTs

Appendix IV sequences unsuccessful attempts to water-solubilize the GNTs (thus preventing the need for a biocompatible surfactant *in vivo*). Despite being unsuccessful, a new material, a GNT with hydroxyl (-OH) groups functionalized to the US-tube nanocapsules' exterior or hydroxylated GNTs, was developed. Details about the synthetic route for obtaining the hydroxylated GNTs can be found within **Appendix IV**.

Metal Analysis

With the exception of the radionuclides of **Chapter 4**, all metal analysis in this thesis was performed on a Perkin-Elmer Optima 4300DV inductively-coupled plasma optical emission spectroscopy (ICP-OES) instrument with ppb sensitivity. For the analysis of powder samples of the US-tube nanocapsules, approximately 250.0 μg of material was oxidized in boiling 30% chloric acid ($HClO_3$) to completion (the $HClO_3$/US-tube nanocapsules mixture would go from black to colorless upon completion). The digestion vessel was washed ten times using 0.5 mL aliquots of 2% HNO_3 prepared with HPLC-grade water, with the resulting solution collected in a 10.00 mL volumetric flask. Upon completion of the washings, the remainder of volumetric flask was filled with 2% HNO_3, and the entirety was filtered using a 0.22 μm PTFE syringe filter to remove any US-tube nanocapsules that were not completely destroyed by the oxidation reaction. For metal

concentrations of surfactant-suspended US-tube nanocapsules samples, the same procedure was followed except 250.0 μL of suspended solution was analyzed instead of powdered sample.

MPMS Sample Preparation and Measurements

Eight samples (Raw SWNT, US-tube nanocapsules, LNTs, and GNTs from both Arc and HiP_{CO} synthesis) were packaged into diamagnetic low-density polyethylene (LDPE) thermoplastic, self-made capsules ca. 1 cm in length. Sample size ranged from 3-8 mg of nanomaterials. Samples were demagnetized prior to measurement.

Magnetic properties of the samples were characterized with a Quantum Design MPMS-XL magnetometer based on a liquid-helium cooled superconducting quantum interference device (SQUID) with a liquid nitrogen jacket. Zero-field-cooled–field-cooled (ZFC-FC) magnetization curves were taken over the temperature range of 5 – 300 K using a magnetic field of 0.1 T. For hysteresis curves, samples were subjected to a range of applied magnetic fields of $-5.0\ \text{T} \leq H \leq 5.0\ \text{T}$ at 2 K. All samples were encapsulated in diamagnetic cellulose for measurements and run in duplicate.

Relaxivity Measurements

All relaxivity measurements were taken with a bench-top SpinTrack Process 1.5 T Relaxometer; relaxivity measurements of randomly selected samples were confirmed on Bruker Minispec mq 60 at 60 MHz. Samples were suspended in a 1.7 % Pluronic solution (a nonionic triblock copolymer with surfactant properties) via probe tip

sonication. All samples were measured at 37 ^{o}C using an inversion recovery pulse sequence, and relaxivity measurement of a control consisting of HPLC-grade water was used for calculations of r_1 and r_2 values.

RESULTS AND DISCUSSIONS

Metal Analysis

The weight percentage data for both catalyst particle (Fe and Ni for HiP_{CO} and Arc synthesized SWNTs, respectively) and loaded lanthanide are summarized in **Table 3**. Additionally, H_C for each sample, as determined from its magnetic hysteresis loop measured at 2K (graphically represented in **Figure 21**), is also represented numerically in **Table 3.**

Table 3. Weight percent (*wt*%) catalyst and lanthanide as determined by ICP-OES. Coercivity (H_C) was measured at 2K.

Sample	HiP_{CO}			Arc		
	wt% Fe	*wt*% La	H_C (Oe)	*wt*% Ni	*wt*% La	Hc (Oe)
Raw SWNTs	17.15	N/A	250	22.76	N/A	130
Purified SWNTs	6.08	N/A	200	15.68	N/A	120
US-tube Nanocapsules	2.32	N/A	140	4.23	N/A	120
LNTs	2.10	4.96	120	2.94	4.38	110
GNTs	1.96	4.87	10	2.70	4.29	10

Magnetism

Figure 20 presents the temperature dependence of both zero-field-cooled (ZFC) and field-cooled (FC) measurements for HiP_{CO} (left) and Arc (right) synthesized SWNTs in a 100 Oe applied magnetic field. Both the raw SWNTs (top) and US-tubes (upper-center) are consistent with superparamagnetism in that the ZFC curves are characterized by a

mean blocking temperature (T_B):

$$T_B = KV / 25k_B$$

above which the material is superparamagnetic and below which magnetic viscosity gives rise to a hysteretic magnetization loop and reduced ZFC magnetization (k_B is the Boltzmann constant).[149] This cusp is a signature of a superparamagnetic state. Using the T_B of 40 K and the magnetic anisotropy constant K for bulk Fe_3O_4, 4 x 10^5 erg/cm^3 (the majority of residual catalyst in raw HiP_{CO} SWNTs exists as magnetite),[150,151] the mean particle volume V = 3.45 x 10^{-19} cm^3, or a mean particle radius r = 4.35 nm. With nine known intermetallic nickel-yttrium alloys as possible precursors, mean catalyst radius is indeterminable for arc samples; regardless, the data indicate an increase of T_B following the cutting procedure (35 K before, **Figure 20e**; 55 K after, **Figure 20f**), suggesting either fluorination or conc. HCl (*aq*.) purification results in not only a decrease in overall catalyst percentage (**Table 3**), but also in mean catalyst radius. These samples have a T_B similar to superparamagnetic small particles of iron oxide (SPIO) that are used currently for clinical MRI T_2 enhancement (ca. 60 K).[152]

Furthermore, the maximum blocking temperature $T_{B,max}$,[153] or the temperature where bifurcation between the ZFC and FC curves occurs, decreases with purification from raw SWNTs to US-tubes (**Figure 20**). As $T_{B,max}$ approaches T_B, the net distribution of superparamagnetic domain sizes become more uniform; this suggests that the purifications remove larger catalyst particles, while smaller particles/domains remain protected within the carbon sheath (recall the internal diameter of the HiP_{CO} and Arc

SWNTs are ca. 1.0 and 1.4 nm, respectively). The reproducible magnetic transition at approximately 75 K for the Arc-synthesized US-tube nanocapsules, GNTs, and LNTs (**Figure 20 (right)**) needs further investigation. The raw data for all M(H) and M(T) plots can be found in **Appendix III**.

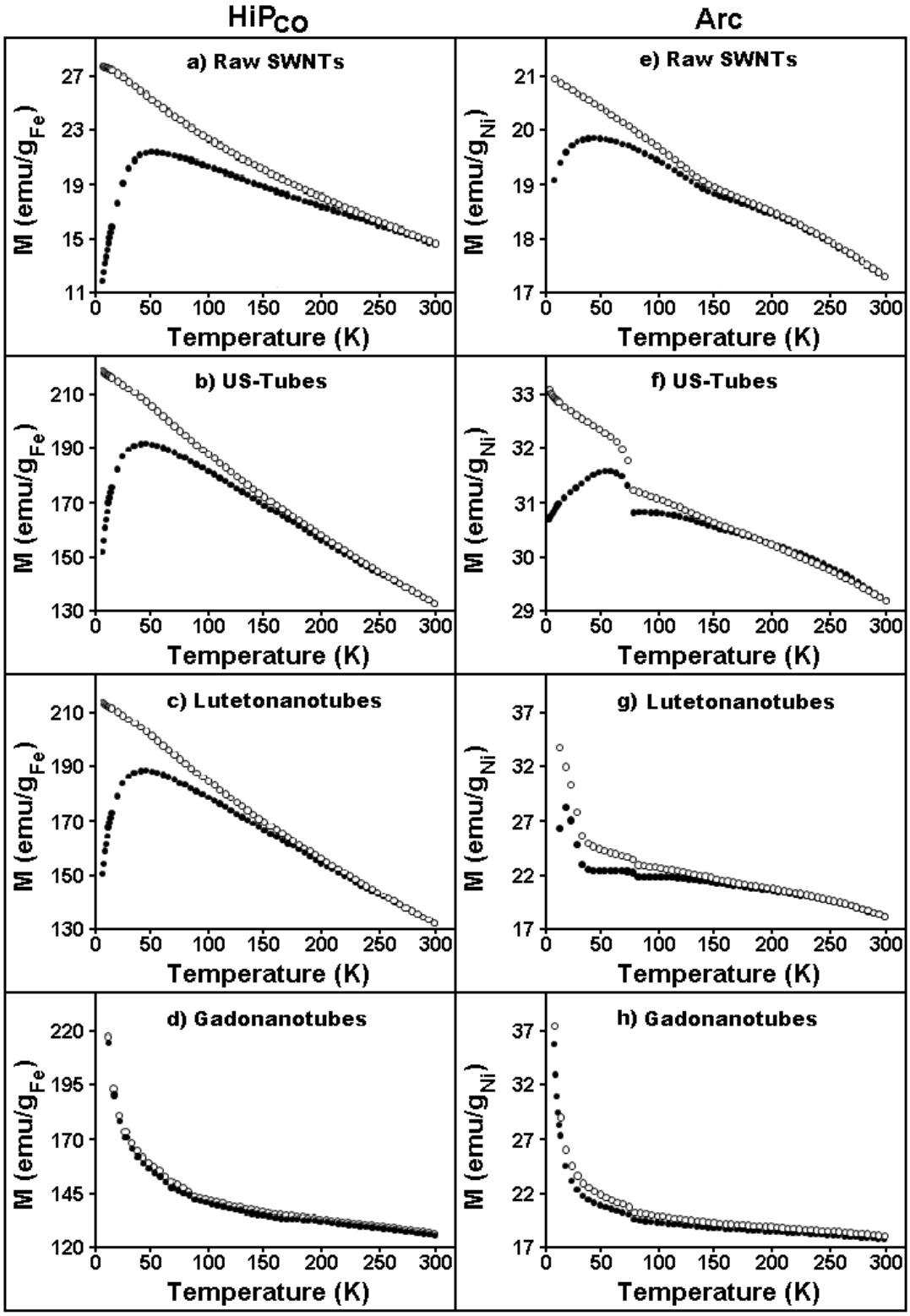

Figure 20. Magnetization versus temperature for raw SWNTs, US-tubes, Lutetonanotubes, and Gadonanotubes from HiPCO (left) and Arc (right) synthesis. Magnetization normalized to catalyst wt%. Field strength = 1000 Oe. ZFC (black) and FC (white).

After loading HiP_{CO} US-tube nanocapsules with diamagnetic Lu^{3+} ions, the resulting LNTs (**Figure 20c**) displayed the same FC/ZFC bifurcation as empty US-tubes (**Figure 20b**) with similar magnetization values. This demonstrates that the superparamagnetic US-tube nanocapsule is essentially unaffected by internal loading with a diamagnetic material; however, after loading US-tube nanocapsules with Gd^{3+} ions, the GNTs' FC and ZFC curves show no divergence (**Figure 20d**), demonstrating that the Gd^{3+}-ion clusters alter the magnetic state of the US-tube material.

To better examine the effects of these Gd^{3+}-ion clusters, it was important to first remove the magnetic effects occurring due to superparamagnetic US-tube nanocapsules. Important to note is paramagnetic susceptibility is inversely proportional to temperature, allowing paramagnetic effects to dominate at very low temperatures where most superparamagnetic materials are blocked and have low susceptibility.[154] Subtracting the M(T) plot for the US-tube nanocapsules (normalized to catalyst mass) from the M(T) plot for the GNTs (also normalized to catalyst mass) rendered an M(T) plot for the GNTs that excluded the effects of the US-tube capsule. Then, by normalizing the sample to moles of Gd^{3+} ions present in the sample, a more accurate M(T) plot for just the effects of the Gd^{3+} ions was produced (**Figure 21 (left)**).

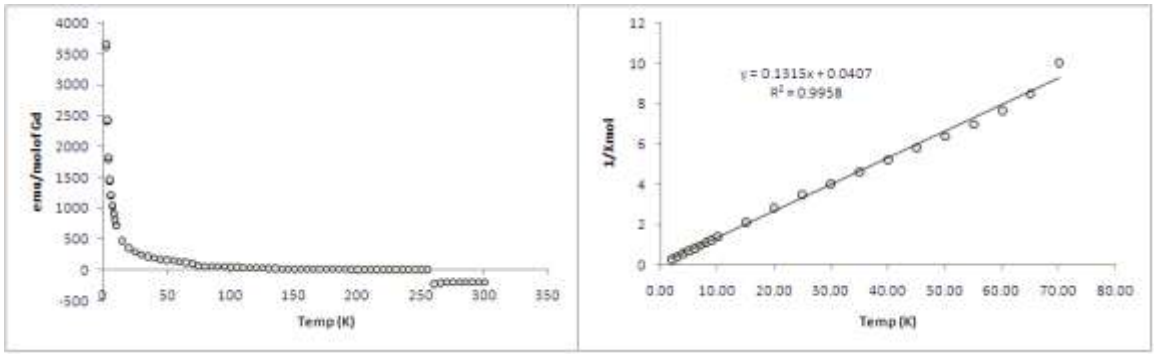

Figure 21. Magnetization versus temperature for Gadonanotubes from HiPCO synthesis. Left: Magnetization of US-tube nanocapsules subtracted from the magnetization of GNTs normalized to molar content Gd^{3+} ion. Right: Inverse molar susceptibility with linear fit over 5 < T < 75. Field strength = 1000 Oe.

It is important to note that at about 75 K, the difference between the M(T) plot of the US-tube nanocapsules and the M(T) plot of the GNTs was nearly negligible, likely suggesting that the magnetic properties of the GNTs are dominated by the US-tube capsule beyond that temperature. By dividing the molar Gd^{3+}-ion M(T) plot (**Figure 21 left**) by H (1000 Oe), the plot became a plot of molar magnetic susceptibility; the inverse of that plot is shown in Figure 21 right for the non-negligible data points from 5 K to 75 K. A linear regression resulted in an excellent fit (R^2 = 0.9958) that almost perfectly intercepts the origin (x-intercept value of -0.309 K). The slope of this regression fit (and hence, $1/C_m$) was 0.1315, which corresponds to a p_{eff} (or effective magnetic moment) of 7.78 μ_B according to:

$$p_{eff} = 2.82\sqrt{C_m}$$

where C_m = is the molar Curie constant with units of emu-K/mol.[144] This is only slightly smaller (ca. 2 %) than the theoretical magnetic moment of free Gd^{3+} ion, S= 7/2, of 7.94 μ_B.[155] Moreover, previous experimental results have shown that the Gd^{3+} ion of

hydroxylated GFs to be 7.7 ± 0.1 μ_B and of Gd-DTPA (Magnevist®) to be 7.9 ± 0.3 μ_B.[156] This paramagnetic character for Gd^{3+} ions is not only characteristic of MRI CAs, but of $Gd@C_{82}$ GFs as well.[157]

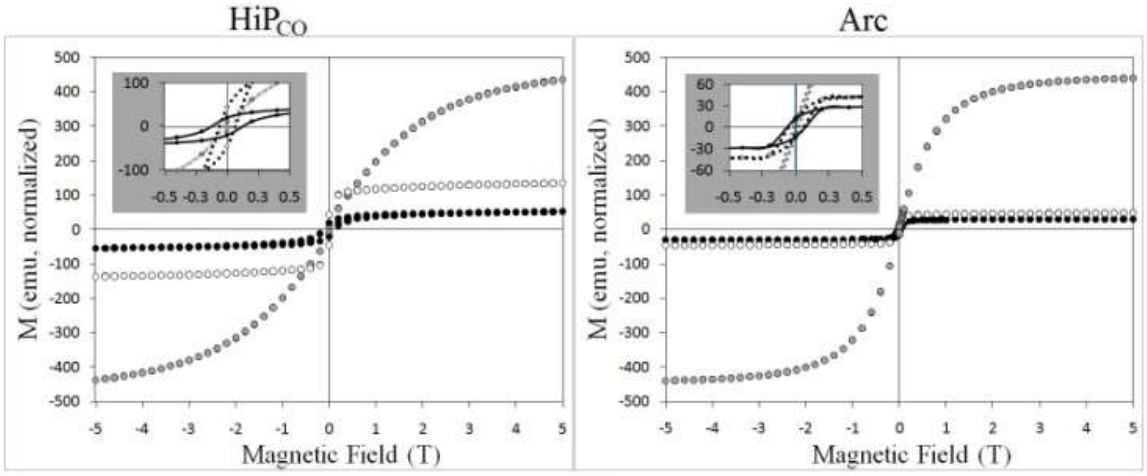

Figure 22. Magnetization versus applied magnetic field (T) for raw SWNTs (white), US-tubes (black), and Gadonanotubes (grey) from both HiPCO (left) and arc (right) synthesis. Measurements taken at 2K after cooling in zero field. 1 T = 1000 Oe.

For further examination of the effect of the Gd^{3+}-ion clusters, normalized magnetization versus applied magnetic field data were collected at 2K (**Figure 22;** note: these figures utilize Tesla instead of Oersted to keep the number of digits on the graph reduced). For the raw SWNTs, the samples rapidly reach magnetic saturation with some coercivity, H_C (**Table 3**). Upon purification and cutting, both steps removing additional metal catalyst impurities, the saturated magnetization logically decreases with decreasing metal fraction; similarly, the H_C of the sample decreases with the removal of catalyst. Finally, upon loading with Gd^{3+} ions, the hysteresis curve for GNTs becomes more hyperbolic and looses the sharp saturation displayed for both raw SWNTs and US-tube nanocapsules. This, coupled with an H_C consistent for no hysteresis within instrument

error, further suggests that the nanoscale Gd^{3+}-ion clusters (less than ten Gd^{3+}-ions with a cluster size of [1 nm x 2-5 nm]) of the GNTs are paramagnetic.

Relaxivity Measurements

Our laboratories have recently shown that the US-tube nanocapsules perform as excellent T_2-weighted CAs.[120] As the GNTs have already been determined to be an excellent T_1-weighted CA,[9] a quick examination of the T_2 relaxation effects of the GNTs was performed. In short, a T_2 relaxation time of ca. 80 ms was obtained for both Arc and HiP_{CO} GNTs suspended in a 1.7 % pluronic solution at 37 ^{o}C. Using a Gd^{3+}-ion concentration as determined by ICP-OES (**Table 3**), the superparamagnetic GNTs possess an r_2 of 230 $mM^{-1}s^{-1}$ per Gd^{3+} ion. From this r_2 value and an r_1 value of ~180 mM^{-1}s-1 per Gd^{3+} ion,[9] the GNTs have an r_2/r_1 ratio of 1.28. Traditionally, when $r_2/r_1 <$ 2.0, the CA is said to be a positive CA, whereas $r_2/r_1 > 2.0$ is indicative of negative CAs;[158] however, a recent CA design with nanoscaled, Gd^{3+}-ion centers and an r_2/r_1 ratio of 1.6 (a traditional positive CA) has proven to be both a positive and negative CA.[159] Likewise, with an r_2/r_1 ratio of 1.28, the GNTs are a traditional, positive CA, but one which also exhibits high-performance negative contrast depending on the MR sequence employed.

Hydroxylation Study

Further probing of the GNTs relaxivity properties occurred on the hydroxylated GNTs (Gadonanotubols) described in **Appendix IV.** The average relaxivity values for the GNTs jumped an impressive 25 % following hydroxylation, suggesting that as much as

one fourth of the relaxation effects of GNTs are being transferred through the carbon side-walls of the nanocapsules and not direct contact of water protons with the paramagnetic gadolinium clusters, as shown in **Figure 23**. These results will help define the GNTs incredible relaxation when considering the large surface area of the nanocapsules compared to the clusters of only a few ions (6-10 Gd^{3+} ions per cluster).

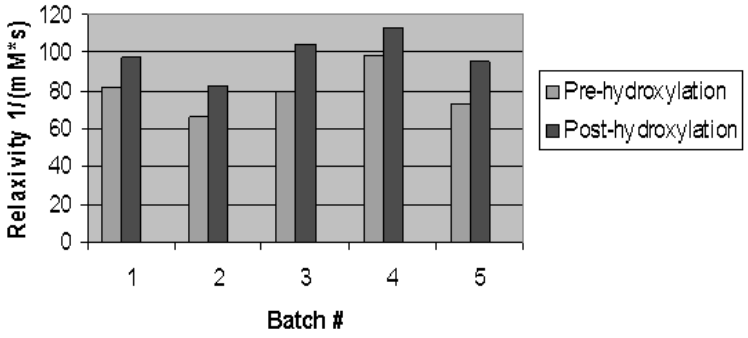

Figure 23. Effects of hydroxylation on GNT relaxivity values.

The GNTs' relaxivity is highly pH sensitive, a feature that could be potentially be employed to allow for diagnostic molecular imaging of cancerous cells, as their external pH values can get as low as 6.3 compared to a healthy physiological pH value of 7.4.[132] The expected pH of a cancerous cell would be around pH 7.0, slightly more acidic than healthy tissue due to the cancerous cell's increased necessity for glycolysis to maintain tumor growth, which results in a higher production of lactic acid. Over this pH range, the GNTs display strong differences in relaxivity measurements (the slope of the change between pH 7.4 and 7.0 is 98 mM^{-1} s^{-1}/unit of pH) which makes the GNTs one of the most dramatic pH-responsive agent in the literature. To ensure this sensitivity remained intact, the pH sensitivity of GNTs was compared to the Gadononatubols, with representative data being shown in **Figure 24**. These measurements were performed on

all samples tested for relaxivity measurements (n = 5), and it was noted that the rate of efficacy increase from pH 7.0 to pH 6.0 for the Gadonanotubols compared to the GNTs was approximately 12%.

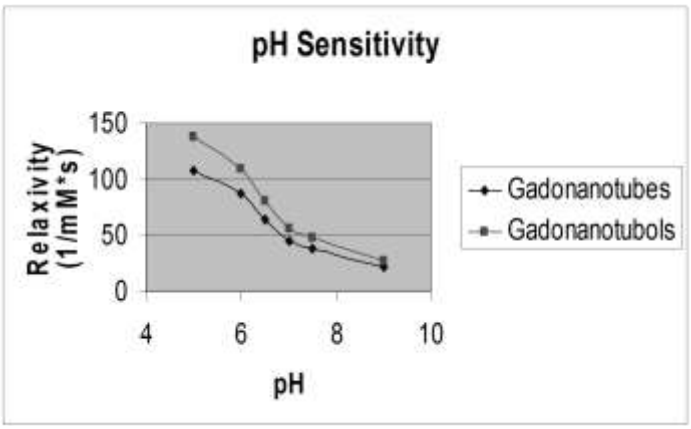

Figure 24. pH sensitivity of GNTs compared to the Gadonanotubols.

CONCLUSIONS

The results of these studies suggest that the GNT is comprised of two magnetic components (**Figure 15**): (1) nanoscale, superparamagnetic catalyst particles inherent of the US-tube capsules that enhance T_2-weighted imaging and (2) nanoscale, paramagnetic Gd^{3+}-ion clusters that enhance T_1-weighted imaging. Monte Carlo simulations have suggested that SWNT materials, like the GNTs, cause a ballistic diffusion of water molecules through their hollow interior,[135] which would effectively allow more water molecules to interact with the magnetic field of the internalized Gd^{3+}-ion clusters, increasing their effective volume. This ballistic diffusion of water through paramagnetic Gd^{3+}-ion clusters probably underlies the high r_1 values, while the remnant superparamagnetic catalyst particles from the synthesis of US-tube nanocapsules

reasonably accounts for the large r_2 values. The hydroxylation studies suggest that the Gadonanotubols: (a) can increase relaxivity of the GNTs by 25%, (b) retain the pH sensitivity of the unfunctionalized GNTs, and (c) hold increased ability to offer pH-basesd cellular differentiation between a pH range of 6.0 and 7.0 pH units. Together, these cooperative properties render a uniquely powerful, yet versatile, bimodal MRI CA. The subsequent chapters of this thesis will explore the stability and range of ions that can form clusters internalized within US-tube nanocapsules.

CHAPTER THREE: RADIOACTIVE LANTHANIDES & ACTINIDES WITHIN US-TUBES

"True stability results when presumed order and presumed disorder are balanced. A truly stable system expects the unexpected, is prepared to be disrupted, waits to be transformed."

~ Tom Robbins, American Novelist

INTRODUCTION

While the previous chapter explored the magnetic properties underlying the Gd^{3+}-ion clusters of the GNTs, this chapter transitions into examining the stability of those clusters, as well as the stability of actinides doped within GNTs, under simulated *in vivo* conditions that the GNTs will encounter in the future. Specifically, **Chapter Three** is divided into two main parts. The first part of this chapter examines the stability of the US-tubes for the retention of Gd^{3+} ions within the GNTs by using the γ-emitting radioinuclide ^{153}Gd (**Figure 25, left**). Previous physiological challenges of the GNTs have shown no leaking of Gd^{3+} ions from the GNTs to the limit of detection for ICP-OES (as described in **Chapter Two**). While promising and at an impressive 1 ppb sensitivity, the ICP-OES can only confirm 99% retention of the Gd^{3+} ions by mass. The present chapter confirms that the other 1% of Gd^{3+}-ion clusters is stable to physiological conditions as well. Additionally, a closer examination of the Gd^{3+}-ion-loading process for the US-tube nanocapsules is also explored. The second part of the chapter examines the ability of US-tube nanocapsules to encapsulate the potent α-particle ($^{4}He^{2+}$) generator $^{225}Ac^{3+}$ ion (**Figure 25, right**).

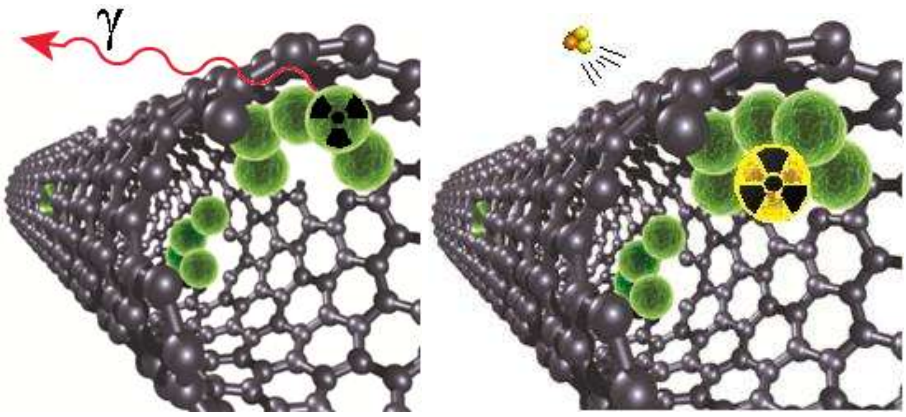

Figure 25: Pictorial representation of a Gadonanotube (left) and actinium-doped Gadonanotube (right). Green spheres represent Gd^{3+} ions, drawn roughly to scale. Green sphere with radioactive sign represents $^{153}Gd^{3+}$ ion, red curved line represents emitted gamma radiation, yellow sphere with radioactive sign represents $^{225}Ac^{3+}$ ion, and yellow/orange cluster represents an emitted alpha particle.

GADOLINIUM ION TOXICITY

This section aims to stress the importance of ensuring Gd^{3+} ions do not leak after internalization within US-tube nanocapsules, since toxicity arising from Gd^{3+} ions can be lethal.

In January 2006, Dr. Thomas Grobner, a nephrologist at the General Hospital of Wiener Neustadt, published an iconic paper that began a global response to Gd^{3+}-ion-based CAs entitled: "Gadolinium – a specific trigger for the development of nephrogenic fibrosing dermopathy and nephrogenic systemic fibrosis?"[160] This publication, classified as an "Interesting Case" by the Journal, documents nine (9) patients suffering from end stage renal disease who underwent a special technique known as Magnetic Resonance Angiography (MRA). MRA utilizes MRI to image blood vessels, most commonly examining arteries for occlusions and/or aneurisms through heavy use of Gd^{3+}-ion-based CAs. Of the nine (9) patients in the report, five (5) patients developed a dermatopathic

disease associated with renal disease known as Nephrogenic Systemic Fibrosis/Nephrogenic Fibrosing Dermopathy (NSF/NFD). NSF/NFD is a newly-discovered disease, first documented in 1997 and first declared a unique disease in 2000,[161,162] which involves painful hardening of the patient's skin with fibrosis at extremities.

In response to the report, the United States Food and Drug Administration (FDA), a branch of the US Department of Health and Human Service tasked, in part, with protecting public health through the regulation and supervision of biopharmaceuticals, issued a Public Health Advisory (PHA) for Gd^{3+}-ion-containing CAs in use for clinical MRIs on June 8th, 2006 (less than 6 months after Grobner's publication).[161] The PHA noted that "the dose of gadolinium-containing [CA] given to patients undergoing an MRA test is often higher (up to three times) than the approved dose for MRI." Furthermore, the PHA specifically noted that none of the then-approved MRI agents (Omniscan, OptiMARK, Magnevist, ProHance, and MultiHance; **Figure 26**) were FDA approved for MRA and warned against use of Gd^{3+}-ion-containing CAs for "patients with advanced kidney failure," citing 25 cases (5 from Grobner's publication) of NSF/NFD linked to Omniscan® (gadodiamide, **Figure 26**).

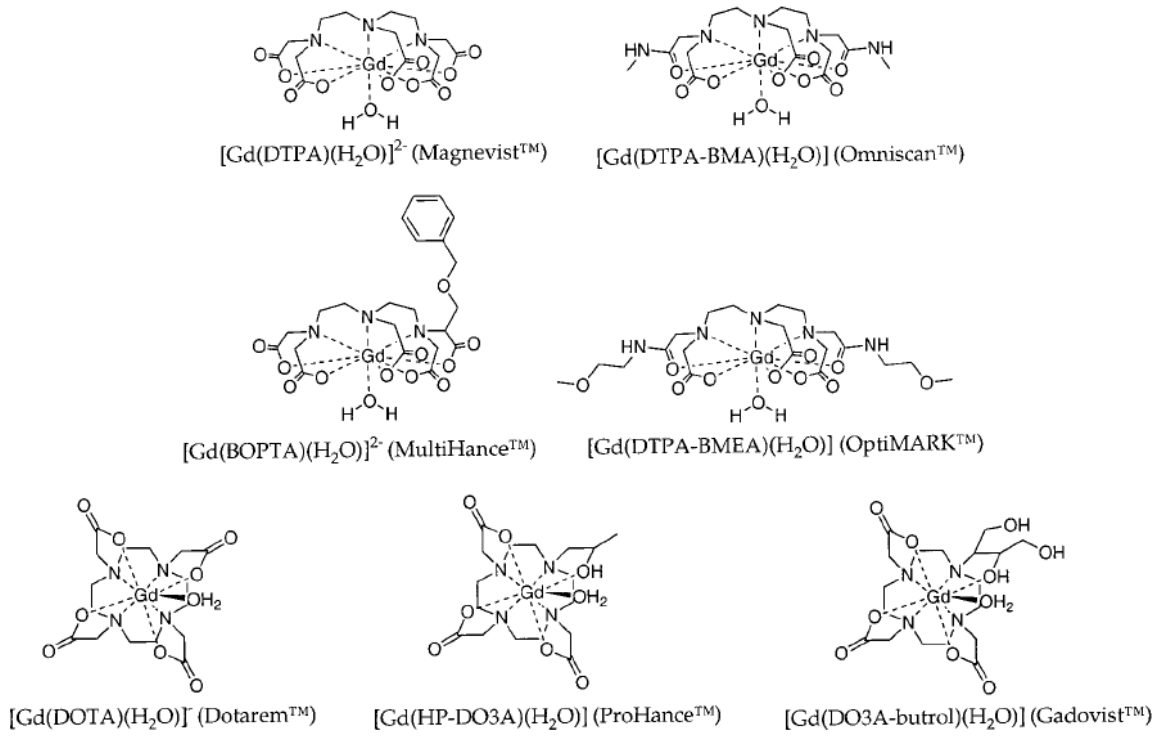

Figure 26: Approved (Europe and/or United States) Gd^{3+}-ion-based contrast agents for use in MRI (from [108]).

Gadodiamide is one of the many clinically-approved nine-coordinate chelation complexes (ligand occupies eight binding sites at the metal center, while the ninth coordination site is occupied by a solvent water molecule).[108] Please note: the focus of comparison to Magnevist™ (gadopentetic acid or Gd-DPTA) throughout this thesis stems purely from Magnevist's dominant market share: with over 20 years of clinical administration, Gd-DTPA has been used in at least 50% of all contrast-enhanced MRI's in the US, administered over 100 million times worldwide since launch, and represented 56% of the US market share in 2009.[163]

By December 21st, 2006, the FDA had raised the number of NSF/NFD cases from 25 to 90 for patients with moderate to end-stage kidney disease following a Gd^{3+}-ion-CA-

enhanced MRA.[164] The FDA also noted that "NSF/NFD has been reported for only three (3) of the five (5) gadolinium-based contrast agents," yet warned against all the potential of NSF/NFD for all five (5).[164] Six months later, the FDA issued a "boxed warning" for all five (5) approved agents.[165]

This boxed warning, "one of the more extreme mechanisms that the FDA may invoke for calling attention to observed serious adverse reactions,"[166] sparked a response from Dr. Emanuel Kanal, a co-author of one of the first MR safety textbooks, in the journal *Radiology*. Within, Dr. Kanal and coauthors list ten (10) itemized reasons for the unjust blanket warning of Gd^{3+}-ion-based CAs. The most critical to this chapter of the thesis states:

> "The dominant theory regarding NSF development and gadolinium deposition in tissues of patients with renal disease is related to the possibility of transmetallation and release of free gadolinium from the chelating agent. The thermodynamic conditional stability constant defines the affinity of the various gadolinium-based agents, at physiologic pH, to bind the gadolinium ion and prevent its release as toxic free gadolinium. Subject to considerations of *in vitro* versus *in vivo* comparison, it is notable that this constant varies substantially among the FDA-approved contrast agents and is lowest for Omniscan and OptiMARK by 100- to 1000-fold, compared with the values for Magnevist, MultiHance, and ProHance.[167] Omniscan and OptiMARK are also the only contrast agents with a substantial amount of excess chelating agent added to the commercially distributed preparation (with Omniscan containing less excess chelating agent than OptiMARK.[167])"[166]

This comparison can be seen with the difference in stability constants shown for Gd^{3+} ion with the linear chelate DTPA (Magnevist™) and the cyclic chelate DOTA (Dotarem™) shown in **Figure 27**.

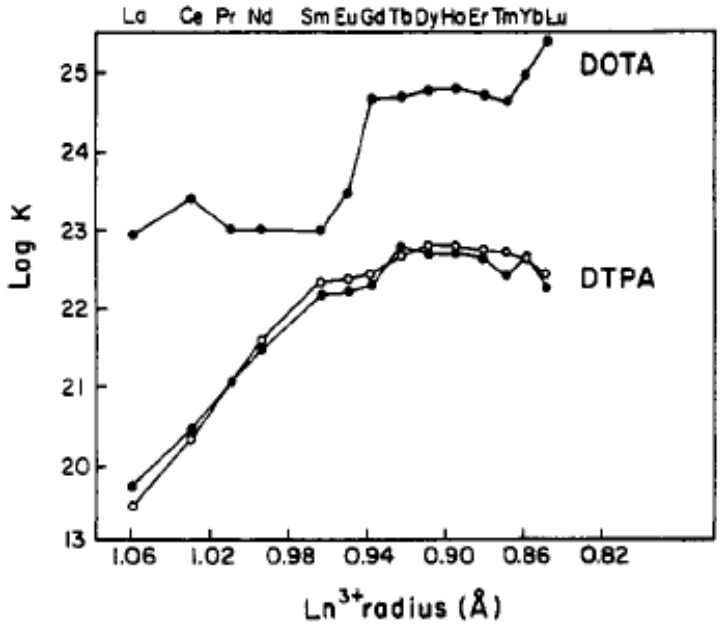

Figure 27: Difference in stability constant for trivalent lanthanide ions for the chemical chelators DOTA and DTPA (note: scale is logarithmic. Adapted from [168]).

This stability constant is important when examining *in vivo* transmetallation of the trivalent gadolinium ions with Zn^{2+}, Cu^{2+}, and Ca^{2+} ions. Toxicity studies show that the smaller stability constants (which correspond to an increase in *in vivo* transmetallation) correlates with an increased median lethal dose (or LD_{50}).[117]

Around the same time as Dr. Kanal's objection to the FDAs blanketed boxed warning, the UK's equivalent to the FDA, the Medicines and Healthcare products Regulatory Agency (MHRA), summarized the Gd^{3+}-ion-based CAs and corresponding NSF/NFD in a Drug Safety Update that reiterated the importance of thermodynamic chemical stability, as shown in **Table 4.**

Table 4: Properties of Gd^{3+}-ion-containing contrast agents and reported cases of NSF (from [169]).

Brand name (generic name)	Chemical structure	Charge	Elimination pathway	Protein binding	Cases of NSF
Omniscan (gadodiamide)	Linear	Non-ionic	Kidney	None	Yes
OptiMARK (gadoversetamide)	Linear	Non-ionic	Kidney	None	Yes
Magnevist (gadopentetate dimeglumine)	Linear	Ionic	Kidney	None	Yes
MultiHance (gadobenate dimeglumine)	Linear	Ionic	97% Kidney 3% Bile	<5%	Yes
Primovist (gadoxetic acid disodium salt)	Linear	Ionic	50% Kidney 50% Bile	<15%	No
Vasovist (gadofosveset trisodium)	Linear	Ionic	91% Kidney 9% Bile	>85%	No
ProHance (gadoteridol)	Cyclic	Non-ionic	Kidney	None	No
Gadovist (gadobutrol)	Cyclic	Non-ionic	Kidney	None	No
Dotarem (gadoterate meglumine)	Cyclic	Ionic	Kidney	None	No

The MHRA summarized the Gd^{3+}-ion-containing contrast agents into three categories relating the risk of NSF (which they define as the likelihood of releasing free Gd^{3+} ion into the body:

(1) **High Risk:** linear chemical structure with excess chelate which carry no molecular charge (eg, Omniscan™ and OptiMARK™)

(2) **In Between:** linear chemical structure with molecular charge (eg, Magnevist™, MultiHance™, Primovist™, and Vasovist™)

(3) **Low Risk:** cyclical structure (eg, ProHance™, Gadovist™, and Dotarem™). [169]

Since the publication of the MHRA's results, the FDA has limited the warnings for Magnevist, Omniscan, and Optimark for patients with kidney disease and has permitted approved the US's first MRA agent, ABLAVAR (generic: gadofosveset), as shown in **Figure 28**:

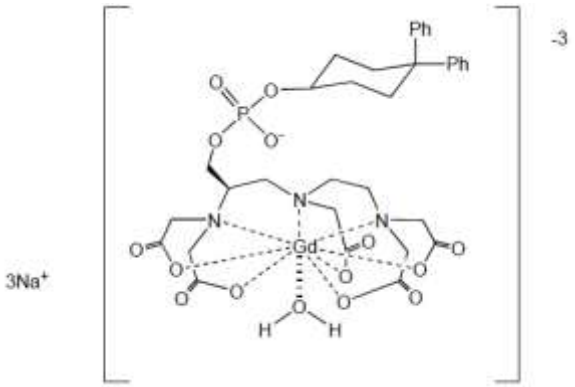

Figure 28: ABLAVAR® (previously: Vasovist™, generic: gadofosveset) - first FDA approved Gd^{3+}-ion-based MRA contrast agent (from official drug label).

The chemical modifications to DTPA's linear backbone (compare **Figure 28** to Gd-DTPA in **Figure 26**) allow gadofosveset to bind to blood proteins (as shown in **Table 4**). Additionally, since the FDA's and MHRA's warnings have been issued, the global number of reports of NSF/NFD has decreased steadily per annum.[163] The approval of ABLAVAR® and the witnessed decrease in cases suggest that the issues of NSF/NFD induced from free Gd^{3+} ion has been properly addressed; however, the importance of sequestering Gd^{3+} ions *in vivo* has clearly been stressed over the past five years.

Knowing this, the GNTs need examination to understand their likelihood of leaking Gd^{3+} ions under *in vivo* conditions. The GNTs have previously been introduced to three (3) *in vitro* challenges designed to best simulate conditions experienced *in vivo*: phosphate-

buffered saline solution (PBS), bovine serum, and heat.[93] Using membrane dialysis for each of the simulated challenge experiments for 48 hours resulted in no measurable loss of Gd^{3+} ion as determined by ICP-OES. With a Gd^{3+}-ion detection limit of ca. 1-2 parts-per-billion (ppb), these early results demonstrate that the GNTs retained 99% of their Gd^{3+}-ion concentration upon exposure to the pH, serum, and temperature challenges. While ppb accuracy is amazing (as a century is 3.1556926×10^9 seconds, 1 ppb would be ca. 3 seconds in a century!), a gamma counter (or γ-ray counter) shows no concentration-dependence for sensitivity since the instrument measures actual events. Repeating these earlier retention studies with a γ counter and γ-emitting gadolinium radionuclides (specifically, ^{153}Gd) has the potential to extend the current understanding *in vitro* retention of Gd^{3+} ions in GNTs from 99% to beyond 99.99%.

PART ONE: ^{153}Gd EXPERIMENTS

Materials and Methods

This section explains the synthesis of ^{153}GNTs, describes the microcentrifugation devices used to wash and challenge the GNTs, explains the simulated physiological challenges used to analyze $^{153}Gd^{3+}$-ion retention, and introduces the instrumentation used to quantify $^{153}Gd^{3+}$-ion decay.

Materials

Debundled US-tube nanocapsules from electric-arc discharge SWNTs with Ni/Y catalyst (AP Grade, CarboLex, Inc., Lexington, Kentucky) were prepared as discussed in

Chapter 1. Carrier-free $^{153}GdCl_3$ (half-life: 241.6 days) was purchased from PerkinElmer New England Nuclear (Boston, MA, Activity: 1.020286 mCi in 36 µL on 27NOV09 [28.33 mCi/µL] and 60.88 mCi/mg specific activity). Carrier-free radionuclides (or radionuclides that are free of more stable isotopes of the same element) are usually preferred for radiolabeling inorganic drugs, as the percentage of radiolabeling will naturally increase when you remove competing isotopes that are chemically-equivalent.[170] As will be established for both $^{153}Gd^{3+}$-ions and $^{225}Ac^{3+}$-ions later in this Chapter, the unique clustering of lanthanide metal ion within the US-tube nanocapsules will require a concentration of radionuclide that carrier-free samples cannot safely provide.

Millipore Centrifugal Filters

Both this chapter and the subsequent chapter, **Chapter 4,** employ the use of centrifugal filters to separate free radionuclide from the US-tube nanocapsules. Specifically, Amicon® Ultra Centrifugal Filter Units (Millipore, Billerica, MA) with a nominal molecular weight limit (NMWL) of 100 kDa (the bovine serum albumin protein (BSA) has a molecular weight of 66.7 kDa, while the Immunoglobin G antibody (IgG) has a molecular weight of 156 kDa, for reference). These filters feature two key components (as shown in **Figure 29**): (1) a 1.5 mL microcentrifuge tube (commonly known as "eppendorfs" due to the major manufacturer: Eppendorf) and (2) a removable filter insert with a cellulose (a common hydrophilic, polysaccharide polymer) filter membrane.

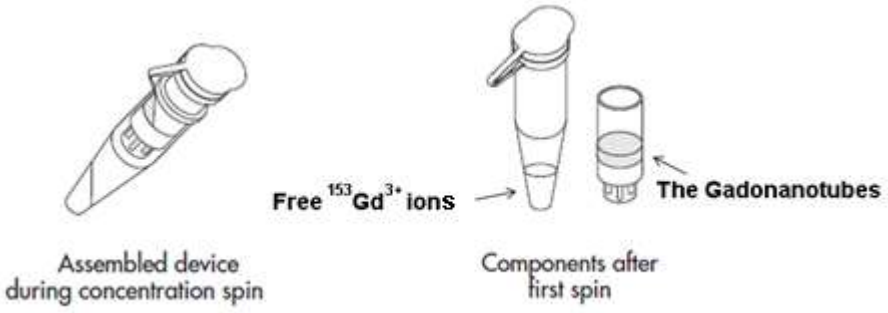

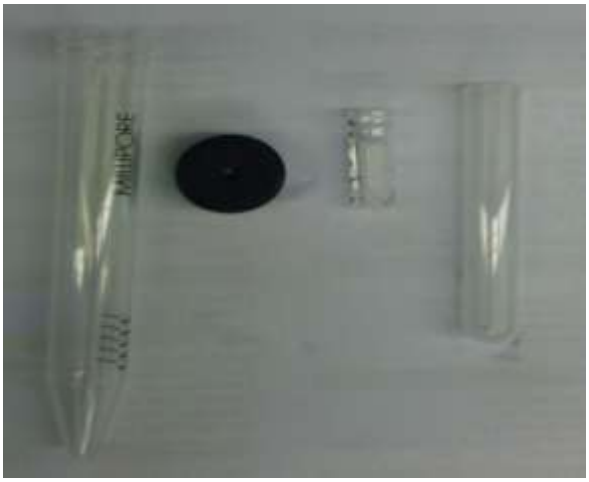

Figure 29: **Top:** Drawings of centrifugal spin devices showing separation of free $^{153}Gd^{3+}$-ions from ^{153}GNTs. This Eppendorf-based model is used for the $^{153}Gd^{3+}$-ion studies in this section, the $^{225}Ac^{3+}$-ion studies in the second half of this chapter, and for the ^{64}Cu challenge experiments of **Chapter 5**. **Bottom:** Photograph of actual centrifugal filter used for the $^{153}Gd^{3+}$-ion studies.

^{153}Gd Loading Study

First, a suspension of 10.0 mg of US-tube nanocapsules was created in 10.0 mL acidic water (~10 mM HCl) to give an approximate concentration of 1 mg/mL. From this, 250 µL of the US-tube suspension was added to a scintillation vial with 125 µL of 10 mM $GdCl_3$ solution and 125 µL of $^{153}GdCl_3$. This mixture was then vortexed to effectively mix the samples. These studies compared a loading technique employing both carrier-free and carrier-added $^{153}GdCl_3$. The final mixtures consisted of: 0.25 mg US-tubes nanocapsules, 0.33 mg $GdCl_3$, and 111 µCi of radioactivity. Following a one hour bath

sonication, the mixture was incubated for 1 to 12 days.

The following day, the prepared solution was vortexed again and transferred in full to a micropore filter inside a centrifuge tube. Make a tube containing 0.5 mL water that can counter balance with the sample tube for centrifuging in a Hettich Model EBA 20 Centrifuge. Following centrifugation at 6,000 RPM for five (5) minutes, the collected filtrate was counted via γ-counter. The filter was then returned to the centrifuge tube, washed with another 0.5 mL of DI water, centrifuged, and the filtrate again was checked for activity. This process continued until there was no activity in the filtrate. Usually, this process required 6 to 7 washings. The final, washed US-tube samples were also counted via γ counter, and a final loading % (wt/wt) was calculated from the total counts and the amount (from carrier and carrier-added) of $GdCl_3$ used.

Note: a parallel control experiment examined the non-specific binding of $^{153}GdCl_3/GdCl_3$ to the walls of the centrifugal micro filter device.

Gamma Counting

Initial gamma counting was performed using a 1282 CompuGamma Gamma Counter (LKB), shown in **Figure 30, top,** a universal γ counter capable of counting γ-emitting isotopes with energies ranging from 10 to 2000 KeV. An example spectrum is displayed in **Figure 30, bottom** with the arrow designating the energy range scanned to determine $^{153}Gd^{3+}$-ion concentration. Subsequent measurements were taken using a Wallac (Perkin-Elmer) 2470 Wizard^2 Gamma Counter.

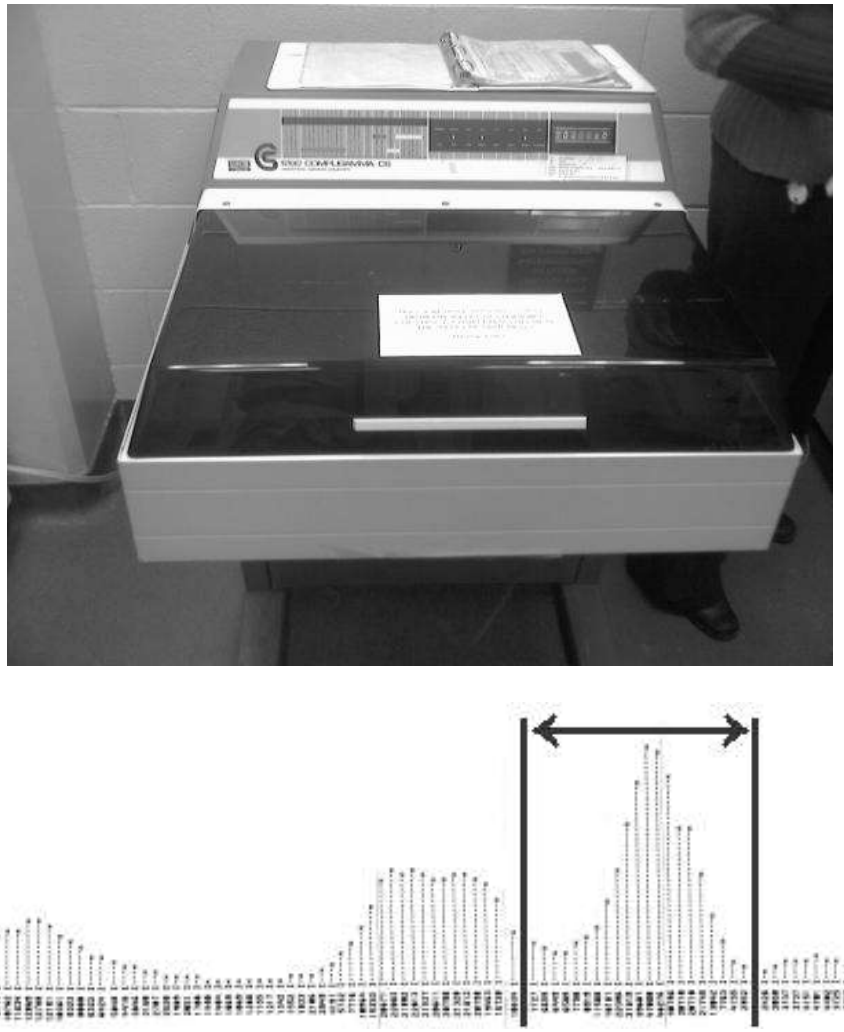

Figure 30: **Top:** 1282 Compugamma CS Universal Gamma Counter. **Bottom:** Representative spectra for ^{153}Gd on gamma counter.

Human Plasma Stability Studies

Centrifugal microfiltration devices were employed to separate human plasma (Sigma) from GNTs. 500 μL of human plasma sample was added to each centrifugal microfiltration device containing carrier-added $^{153}GdCl_3$-loaded US-tube nanocapsules, carrier-free $^{153}GdCl_3$-loaded US-tubes, and the control solution of carrier-added $^{153}GdCl_3$ (no US-tube nanocapsules). All filters were centrifuged for 15 minutes following a 2 h incubation period. The filtrate and the microfiltration devices were γ counted, and the

percentage of $^{153}Gd^{3+}$-ion released was determined comparing counts in the filter and filtrate. The filtrate was replaced with fresh plasma and in the same microfiltration device, incubated for an additional 48 h, and then centrifuged again for 15 minutes. Again, the percentage of $^{153}Gd^{3+}$ ion released was determined comparing counts in the filter and filtrate.

Results and Discussion

Loading Studies

Despite attempts with both carrier-added and carrier-free $^{153}GdCl_3$ for our loading studies, all attempts with carrier-free $^{153}GdCl_3$ proved unsuccessful in synthesizing GNTs (99.9% of ^{153}Gd was removed by the fourth washing). This is likely owed to the fact that with no carrier, 111 μCi correlates to approximately 1.8 μg of Gd^{3+} ion for 250 μg of US-tube nanocapsules. Using a rough molecular weight of 72000 g/US-tube nanocapsules (estimating 120 C atoms per nm at an average length of 50 nm per US-tube nanocapsule), there was a rough molar ratio of 3.3 (3.3 Gd^{3+} ions per US-tube nanocapsule). As all previous TEM imaging suggest Gd^{3+}-ion cluster sizes of 6-10 Gd atoms per US-tubes (discussed in further detail in **Chapter 2**), the most-likely reason that the carrier-free loading techniques failed is simply due to a lack of concentration to successfully form stable Gd^{3+}-ion clusters within the US-tube nanocapsules. Due to the relatively low concentration of Gd^{3+} ions present within the GNTs, previous attempts at better understand the true chemical nature of these clusters have not proven fruitful.

Gd^{3+}-ion complexes have been previously synthesized at low concentrations in aqueous

solutions through the formations of hydroxyl bridges;[171] binuclear gadolinium complexes are formed via hydroxyl bridges in most compounds over 0.5 nm in diameter. An example of a more complex gadolinium cluster can be seen in the hydroxyl- and oxo-bridged cation shown in **Figure 31** (Note: the cluster shown in **Figure 31** is of a Nd^{3+}-ion cluster that is isomorphous with the Gd^{3+}-ion cluster).[172]

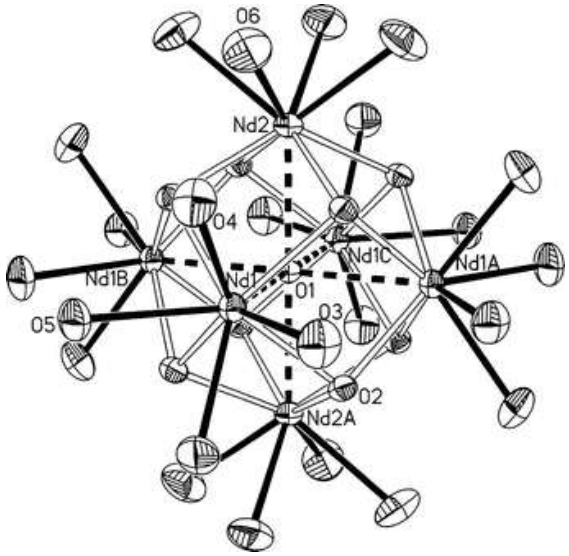

Figure 31: Oak Ridge Thermal Ellipsoid Plot Program (ORTEP) molecular modeling of the $[Nd_6(\mu_6\text{-}O)(\mu_3\text{-}OH)_8]^{8+}$ cation cluster. This cluster is isomorphous with the $[Gd_6(\mu_6\text{-}O)(\mu_3\text{-}OH)_8]^{8+}$ cation cluster (adapted from [172]).

This cluster is an oxo-centered octahedron that is synthesized in similar conditions to the GNTs. In short, $Gd(ClO_4)_3$ is added to an acidic solution of L-serine, and the pH is adjusted to above 6.0 by the addition of NaOH (*aq*). Recall from **Chapter 2** that the GNTs are synthesized by placing US-tube nanocapsules in acidic $GdCl_3$ (*aq.*), and the pH is adjusted to above 5.0 following washings with DI water. As the magnetic studies of **Chapter 2** suggest that the Gd^{3+} ions within GNTs have isolated magnetic spins, it is unlikely that this is the exact cluster one would expect within the GNTs, primarily as the

central μ_6-oxo ligand would be expected to facilitate magnetic exchange coupling interactions between the Gd^{3+} ions (note: magnetic susceptibility measurements for the cluster and isomorphs of **Figure 31** do not currently exist).[173] However, having the proper number of expected Gd^{3+} ions (the cluster of **Figure 31** has 6 lanthanide ions and the Gd^{3+}-ion clusters within the GNTs contain 6-10 ions) and having formed in similar, aqueous environments, the Gd^{3+}-ion-based analog of the cluster in **Figure 31** is currently among the best models for how the Gd^{3+} ions exist within the GNTs. This large cluster further supports the hypothesis that individual Gd^{3+} ions enter the US-tube nanocapsules and form clusters that are too large to escape, hence their high stability even under physiological challenge. For a short description on the general properties of gadolinium, see **Appendix VI**.

Moreover, concentrating carrier-free $^{153}GdCl_3$ to mimic cold loading protocols would be both cost prohibited and, with a 242 day half-life, generate far too much radioactive waste. This failure to retain ions under a critical concentration will be seen to repeat with carrier-free $^{225}Ac^{3+}$-ions later in this chapter. The results of the loading over various incubation times are summarized in **Table 5**.

Table 5: Loading percentages (w/w) of $^{153}Gd^{3+}$-ions varying addition of carrier ions and incubation time.

$^{153}GdCl_3$ Used	Incubation Period	% Retained by US-tube Nanocapsules
Carrier Free	24 hr	0.24
Carrier Added	72 hr	10.0
Carrier Added	288 hr (12 d)	17.6

While the result of 17.6 % retention is significantly higher than previously recorded 2.8 % (w/w) retention of the available Gd^{3+} ions in solution, this value also corresponds to roughly the same number of Gd^{3+} ions per US-tube nanocapsules: using the 72000 g/US-tube nanocapsule of length 50 nm assumption described above, the published 2.84% retention of the high concentration $GdCl_3$ loading corresponds to 13.0 Gd^{+} ions per nanocapsule, which is roughly the same as the 12.5 Gd^{3+} ions per nanocapsule using the same assumptions for the lower concentration $^{153}GdCl_3$ loading.

Plasma Stability

The results from the plasma stability studies are summarized in **Table 6.** In short, these studies show that there are two distinct populations of Gd^{3+} ions: (a) one population is removable following a 2 hour incubation in human serum and (b) another population is unremoved despite a 48 hour serum challenge.

Table 6: Plasma stability study results.

Sample	% Counts in filtrate (after 2 hr)	% Counts in filtrate (after 48 hr)
Control	35.8	50.6
^{153}GNTs	41.6	35.6

The significance of this data is demonstrated via the 48 hr time-point, with the ^{153}GNTs retaining a significantly higher percentage (15% more) of initial activity than free $^{153}Gd^{3+}$ ions in serum. This suggests that some stabilization beyond the standard two hours is required when loading with significantly low concentrations of ions.

Conclusions

All of the results of these radiolabeling/loading studies suggest a key conclusion about the GNTs: there are a critical minimum number of Gd^{3+} ions required per US-tube nanocapsules to produce stable clustering. Synthesizing GNTs with more than the critical number per US-tube nanocapsules, however, does render any significant differences in the final GNT product. This fact is incredibly useful in attempts to minimize the amounts of precursor $GdCl_3$ used for synthesis.

Another important conclusion is that the stability of the GNTs *in vitro* under conditions that would be experienced *in vivo* (previously established with 99 % certainty) show NO leakage of toxic Gd^{3+} ions following 48 hour plasma challenge. This conclusion solidifies earlier claims that the GNTs should prove stable under *in vivo* conditions which should encourage future development of the GNTs as viable *in vivo* MRI CAs.

PART TWO: ^{225}Ac EXPERIMENTS

As the first part of this chapter exploited a radionuclide ($^{153}Gd^{3+}$ ion) to monitor potential leakage of the Gd^{3+} ions from GNTs under physiological conditions, the second part of this chapter aims to exploit a significantly more potent radionuclide, the α-particle generator $^{225}Ac^{3+}$-ion, for potential use in radiotherapy within US-tube nanocapsules. Many of the conclusions and proposed explanations for the Gd^{3+}-ion-loading process for the US-tube nanocapsules used in the previous part of this chapter will carry over into the $^{225}Ac^{3+}$-ion section.

Alpha Radiotherapy

Following cancer diagnosis, one common treatment approach used by oncologists is radiotherapeutics. As opposed to surgery, which is highly invasive and specific for large tumors, radiotherapeutics, similar to traditional chemotherapeutics, offer a noninvasive form of cancer treatment. Unfortunately, also like traditional chemotherapeutics, radiotherapeutics are toxic to all cells (both healthy and cancerous/diseased). The ultimate goal of the radiotherapeutics is to impair cellular mitosis via targeting cells that divide rapidly. Unfortunately, certain healthy cells in the body also divide rapidly, which results in the painful collateral damage of healthy cells that is associated with chemotherapy;[174,175] these include the cells found in bone marrow (which produce red blood cells, so this collateral damage results in a decrease in red blood cell production, known as myelosuppression) and the cells that line the intestinal tract (which results in painful inflammation known as mucostitis). Perhaps the most visually apparent sign of collateral damage is the hair loss (alopecia) associated with chemotherapy due to chemotherapeutics attacking the hair follicles.

Unlike chemotherapeutics, however, cancerous cells do not become immune to the radiotherapeutics. So with this drawback to chemotherapeutics alleviated, the other primary goal for radioimmunotherapy of cancer (RAIT) is to eliminate unwanted collateral damage.[176,177] One method is to create a targeted drug via attachment of moieties (antibodies, peptide sequences, etc.) that will have an affinity for cancerous cells. The US-tube nanocapsules' graphitic carbon sheath allows for covalent functionalization with disease-targeting agents.[7,141,178-181] This feature renders SWNT-

based materials ideal as delivery platforms for targeted α-particle therapy (TαT), a specific branch of RAIT (10, 11). This part of **Chapter 3** specifically examines the ability of US-tube nanocapsules to encapsulate the potent, *in vivo* α-particle ($^{4}He^{2+}$) generator ^{225}Ac whose decay sequence is shown in **Figure 32**.

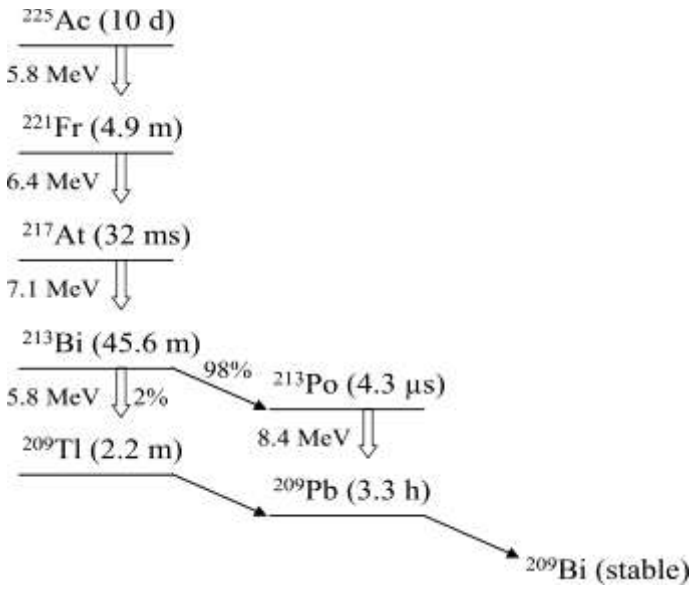

Figure 32: Simplified decay scheme for ^{225}Ac. Each arrow represents an α-particle emission with the average energy to each arrow (adapted from [182]).

α-particle emitters, such as ^{213}Bi, ^{211}At, and ^{225}Ac, possess a significantly higher linear energy transfer (LET) (5,000 – 8,000 keV) and shorter range (50–80 μm, or a few cell diameters,) than the β-particle (e^{-}) emitters, such as the FDA-approved ^{90}Y and ^{131}I, which are currently used in RAIT [11,176,183]. For these reasons, α-particle emitters are preferred for the specific killing of small volume cancers such as single cells or micrometastatic lesions. Moreover, Monte Carlo simulations suggest that a solitary α-particle can have an equivalent cytotoxic effect as over a thousand β-particles.[184] ^{225}Ac's

potency is further enhanced by the yield of 3 daughter α-particle emitting radionuclides that are also lethal to targeted cells (**Figure 32**).

Traditional radiometal-labeling requires the use of chelates, such as DOTA or DTPA, to sequester the free radionuclides to the targeting ligand; these ligands have two primary drawbacks: (1) traditional chelating agents are only capable of transporting a single radiometal and (2) loss of $^{225}Ac^{3+}$ ion from these agents results in poor body clearance and accumulation of $^{225}Ac^{3+}$ ion in the liver.[185] The stability constant for a EDTA-Ac complex is only $10^{14.2}$ (well below the minimum threshold of 10^{20} for safe *in vivo* use), and EDTA, DTPA, and DOTA show similar instability *in vivo.*[186]

The first drawback causes limitations in accumulating potent $^{225}Ac^{3+}$ ions to targeting agents, such as monoclonal antibodies (mAbs), for the delivery of therapeutics to specific sites *in vivo* may decrease the toxicity via minimizing nonspecific tissue damage (the aforementioned collateral damage).[177] For example, EDTA antibody constructs and DTPA antibody constructs have been synthesized with 4 chelates per antibody before substantial effects occurred in radionuclide stability and biodistribution.[186] The empty, available interior of the US-tube nanocapsules allows for multiple radiometals per targeted drug molecule. As only one Gd^{3+}-ion cluster within an US-tube has up to 10 Gd^{3+} ions on average and each GNT has multiple Gd^{3+}-ion clusters on average, US-tube nanocapsules internalized with chemically-similar Ac^{3+}-ion clusters hold potential to concentrate significantly more radioactivity per targeting moiety. As there is an inherent preference for intracellular uptake and retention of radiometals over radiohalides,[187] and

the US-tube nanocapsules are also relatively bio-inert, intracellular agents,[74,142] the successful targeting of a US-tube nanocapsule/$^{225}Ac^{3+}$-ion construct could lead to a rapid uptake of radiometal within the targeted diseased cells. Furthermore, Rituximab and Lintuzumab antibodies have successfully been attached to the carbon-sidewall exterior of SWNTs for *in vivo* targeting.[6] The key difference the US-tube nanocapsules provide compared to previous targeting of SWNT-based materials with radiolabels is the fact that the radionuclide of choice is internalized within the carbon sheath (and in significant number) as opposed to being bound to externally-functionalized chelating agents.

The second drawback to traditional chelating agents is one of toxicity. Specifically, high toxicity stems from free $^{225}Ac^{3+}$ ions which deposits in the liver and bone tissue.[185] Traditional chelating agents have proven unstable under *in vivo* conditions, resulting in toxic free $^{225}Ac^{3+}$ ion. For example, the acyclic chelating agent DTPA bound to $^{225}Ac^{3+}$ ion and an antibody specific for lung cancer (^{225}Ac-CHX-DTPA-mAb 201B) results in 100% mouse mortality 8 days post-injection at only a dose of 185 kBq (5 μCi).[188] While no chemical agent will likely survive the high energy of the first α-decay in the $^{225}Ac^{3+}$-ion decay sequence (**Figure 32**), the potential for the US-tube nanocapsules to retain $^{225}Ac^{3+}$ ions similar to the Gd^{3+} ions within the GNTs discussed in the previous part of this chapter would prevent the loss of $^{225}Ac^{3+}$ ion experienced by traditional chelating agents *in vivo.*

Herein is reported a novel synthetic pathway for the internalization and stabilization of $^{225}Ac^{3+}$ ions within US-tube nanocapsules (accomplished through the addition of Gd^{3+}

ions).

Materials and Methods

Materials

A dried $^{225}AcNO_3$ residue obtained from the Department of Energy (Oak Ridge National Laboratory, Oak Ridge, TN) was dissolved in 0.1 ml of 0.2 M HCl (Optima grade, Fisher Scientific, Pittsburgh, PA). ^{225}Ac activity was measured using a drop well dose calibrator (CRC-17 Radioisotope Calibrator, E.R. Squibb and Sons, Inc., Princeton, NJ) set at 775, with displayed activity value multiplied by 5.

Individualized US-tube nanocapsules were prepared following previously-established synthetic methods (**Chapter 1**) from full-length SWNTs produced in an electric arc discharge with Ni/Y catalyst (AP Grade, CarboLex, Inc., Lexington, Kentucky).[5]

^{225}Ac@US-tubes

US-tube nanocapsules were dispersed via bath sonication to a concentration of 5 g/L in metal-free water obtained from a Purelab Plus system (United States Filter Corp., Lowell, MA). Three separate aqueous loading techniques were examined: (1) addition of $^{225}Ac^{3+}$ ions alone, (2) addition of a mixture of Gd^{3+} ions and $^{225}Ac^{3+}$ ions, and (3) sequential addition of Gd^{3+} ions followed by $^{225}Ac^{3+}$ ions. For $^{225}Ac^{3+}$ ions alone, 3.0 μL of $^{225}AcCl_3$ (7.0 MBq) were diluted in 200.0 μL of metal-free water and mixed with 50 μL of a US-tube suspension. For the mixture, 3.0 μL of $^{225}AcCl_3$ (7.0 MBq) were diluted in 150.0 μL of metal-free water, mixed with 50 μL of 19 mM $GdCl_3$ (Aldrich Chemical Milwaukee, WI, USA) and 50.0 μL of the US-tube suspension. Finally, for the

sequential addition, 150.0 μL of metal-free water was mixed with 50.0 μL of 19 mM $GdCl_3$ (previously established method for creation of the GNTs); 12 hours later, 7.0 MBq of $^{225}AcCl_3$ was added to the $GdCl_3$/US-tube solution. Activity was determined using a Packard Cobra γ counter (Packard Instrument Company, Inc., Meriden, CT) with a 340-to 540-KeV window.

All loading techniques underwent bath sonication for two hours and were allowed to equilibrate overnight. The following day, all samples were washed with 250.0 μL of metal-free water and filtered using a Handee™ Micro-Spin Column (Thermo Scientific Pierce) with a paper membrane (pore size ~10 μm) until no activity was detected in the filtrate via drop well dose calibrator. Following filtration, all samples were removed from the filter with 200.0 μL distilled water by pipette aspiration and measured for activity. All loading techniques were performed in triplicate.

Human Serum Challenge Experiments

To simulate in vivo conditions, challenge experiments were conducted monitoring the effect of heat, time, and human serum on the ^{225}Ac@US-tube nanocapsules suspensions. For each serum challenge, 20.0 μL of the resulting ^{225}Ac@US-tube nanocapsules (12.5 μg) suspension from the three loading techniques above was added to 180.0 μL of normal human AB serum (Sigma Chemical Co., St. Louis, MO). The mixture was stirred and incubated at 37 ºC for two hours. After incubation, the mixture was filtered using a centrifugal filter devices (100xg, 5 min.), and the serum filtrate was counted in scintillation fluid using a β counter (samples were allowed to reach equilibrium

overnight). Standards of the ^{225}Ac@GNTs (loading technique (2) from above) were counted as reference. For re-challenging the samples, 200.0 μL of serum was again added to the filter device, and the mixture was re-suspended and re-incubated at 37 ºC for 2 hours. The filtration process was repeated. As a control, $^{225}AcCl_3$ alone in serum was spun in the filter device. Samples also were challenged for longer time durations (4 hr and 12 hr) and at both room temperature (RT) and 37 ºC to compare the effects of temperature and time.

Results and Discussion

Serial washings via centrifugation filtration resulted in over 95% of the added activity remaining with the US-tube nanocapsules. For both loading techniques involving Gd^{3+} ions with $^{225}Ac^{3+}$ ions, approximately 50% of the activity remained associated with the US-tubes. All three loading experiments showed no radioactivity in the centrifugal filtrate following the third wash, indicating that only 750.0 μL of metal-free water is required to separate the $^{225}Ac^{3+}$ ions not bound to the US-tube nanocapsules in suspension.

The results of the serum challenge experiments are summarized in **Figure 33**. In short, there was little difference in $^{225}Ac^{3+}$ ion retention observed between sequential and simultaneous loading of $^{225}Ac^{3+}$ and Gd^{3+} ions within the US-tube nanocapsules. Moreover, the additional challenges of time (both 4 hr and 12 hr) and elevated temperature (37 ºC) on the ^{225}Ac@GNTs synthesized via simultaneous loading technique did not promote additional losses of $^{225}Ac^{3+}$ ions.

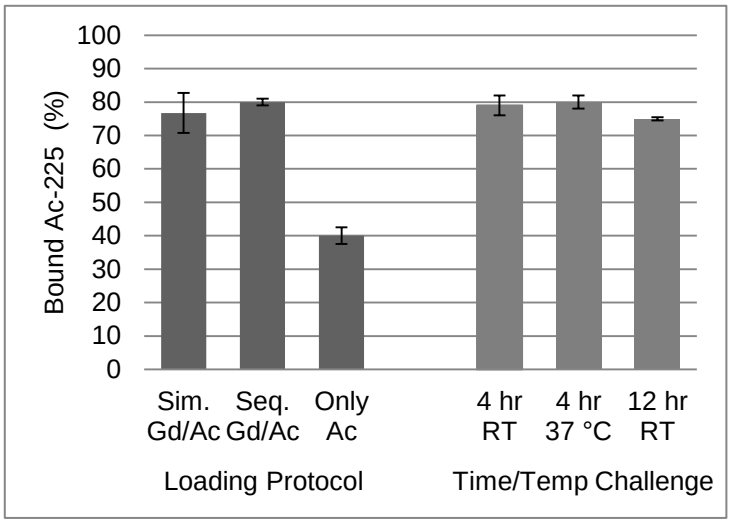

Figure 33: Results of human serum challenge experiments. Time/Temp challenge experiments performed on ^{225}Ac@GNTs synthesized via simultaneous loading. Sim. = simultaneous loading, Seq. = sequential loading, and RT = room temperature.

Finally, subsequent challenges of the ^{225}Ac@GNTs revealed no measurable quantity of $^{225}Ac^{3+}$ ions in the filtrate and ~100% retention of the $^{225}Ac^{3+}$ ions with the ^{225}Ac@GNTs in the filter. However, subsequent challenges of the ^{225}Ac@US-tubes continued to remove $^{225}Ac^{3+}$ ions, until only 5% of $^{225}Ac^{3+}$-ion activity remained bound to the US-tube nanocapsules.

The above results were consistent with the hypothesis that the $^{225}Ac^{3+}$ ions would behave similarly to the Gd^{3+} ions within US-tube nanocapsules due to the similar solution chemistry of both trivalent actinide ions and trivalent lanthanide ions.[189] One exception was the continual leaking of $^{225}Ac^{3+}$ ions from the US-tube nanocapsules upon repetitive serum challenges, while $^{153}Gd^{3+}$ ions did not leak under similar conditions (see Part I of this chapter).[132] Therefore, it is unclear whether the internalization of the $^{225}Ac^{3+}$ ions

directly mimics the Gd^{3+} ion internalization of the GNTs. Previous high-resolution transmission electron microscopy (HRTEM) images revealed that Gd^{3+} ions existed in small (1 nm x 2-5 nm) clusters that corresponded to roughly 6-10 Gd^{3+} ions per cluster;[9] additionally, the GNTs averaged 2-5% Gd by mass as determined ICP-OES. Assuming a mean length of 50 nm and a minimum of 112 carbon atoms per nanometer (a (7,7) chirality with diameter of ca. 0.95 nm, the mean diameter of HiPco),[190] each US-tube nanocapsule contains roughly 9-21 Gd^{3+} ions. The synthesis method herein utilizes the maximum concentration of $^{225}Ac^{3+}$ ion commercially available and the minimum concentration of US-tubes that can be reliably manipulated for filtration experiments, yet only provides one $^{225}Ac^{3+}$ ion for roughly every 250 US-tube nanocapsules. At this low concentration, there is not enough $^{225}Ac^{3+}$ ions present to form $^{225}Ac^{3+}$-ion clusters that would directly mimic the Gd^{3+}-ion clusters inside the GNTs. However, the $^{225}Ac^{3+}$ ions do behave similarly to the Gd^{3+} ions when admixed into the US-tube nanocapsules with Gd^{3+} carrier metal, allowing for use of the cold Gd^{3+} ion for the majority of the cluster atoms within the US-tube nanocapsules. Interestingly, the methodology of loading (sequential vs. simultaneous) appears to have little to no effect on the final product. This proves beneficial to future synthesis routes with regards to the time of production of $^{225}Ac^{3+}$-ion clusters within the US-tube nanocapsules, and the solution chemistry of the $^{225}Ac^{3+}$ ions within the GNTs further supports the hypothesis that a cluster of ions is critical for their embedment and retention within the US-tube nanocapsules and their resistance to serum challenge.

Conclusions

In summary, the ^{225}Ac@GNTs provide a novel alternative to chelation for radiometal ions useful for TαT. The resistance of the ^{225}Ac@GNTs to physiological challenges strongly suggests that this agent would not suffer the release of highly toxic, free $^{225}Ac^{3+}$ ions *in vivo* currently associated with traditional chelating agents.[185,188] Furthermore, as the demand for $^{225}Ac^{3+}$ ion rises resulting in an decrease of supply, the US-tube nanocapsules hold potential to contain a concentration of the isotope that will net over 100 α-particle emissions from a single, targeted US-tube nanocapsules. Until higher concentrations become commercially available, the doping of the $^{225}Ac^{3+}$ ions within the Gd^{3+}-ion clusters of the GNTs provides a new technology that could be especially useful for those cases (for $^{225}Ac^{3+}$ RAIT) where *in vivo* retention of radiometals within chelating agents remains problematic. The next chapter of the thesis further explores the doping of radionuclides within the GNTs' stable Gd^{3+}-ion clusters.

CHAPTER FOUR: POSITRON EMISSON TOMOGRAPHY RADIONUCLIDES WITHIN US-TUBES

"The world is an old woman, and mistakes any gilt farthing for a gold coin; whereby being often cheated, she will thenceforth trust nothing but the common copper"

~ Thomas Carlyle, Scottish Essayist

INTRODUCTION

Similar to the previous chapter's exploitation of the stable Gd^{3+}-ion clusters in the GNTs to stabilize the encapsulation of the $^{225}Ac^{3+}$ ion, this chapter aims to extend that exploitation to include the $^{64}Cu^{2+}$ ion. The primary purpose of **Chapter Four** is to explore the use of US-tube nanocapsules as multimodal imaging agents for use in combined MRI/PET (positron emission tomography) imaging. The first part of the chapter discusses preliminary experiments utilizing the US-tube nanocapsules to encapsulate the positron-emitting radionuclide, ^{125}I of molecular iodine ($^{125}I_2$). High costs caused this project to be abandoned, which lead to the second part of the chapter: experiments creating a novel material consisting of the positron-emitting $^{64}Cu^{2+}$-ion radionuclide doped within the Gd^{3+}-ion clusters of the GNTs (**Figure 34**). Ultimately, the chapter establishes a stable multimodal (PET, T_1-weighted MRI, and T_2-weighted MRI) agent, the ^{64}CuGNTs (^{64}Cuprogadonanotubes or ^{64}Cu@GNTs, **Figure 34, right**).

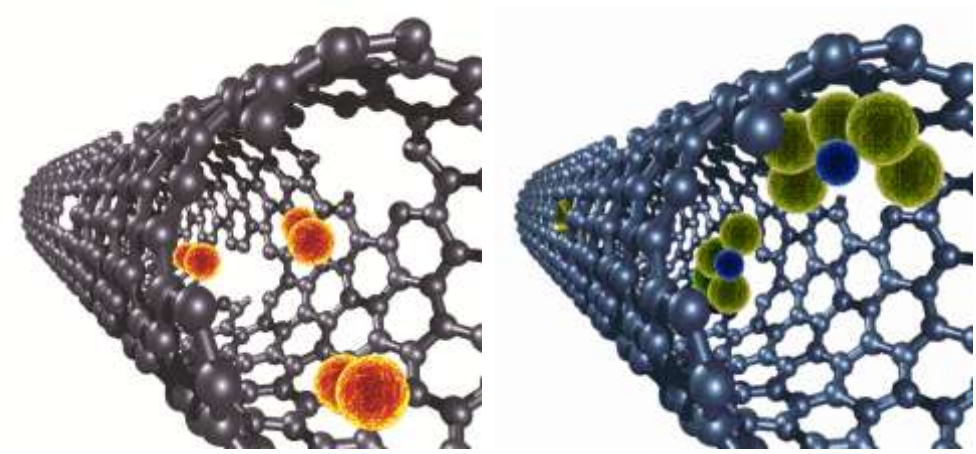

Figure 34: Pictorial representation of a US-tube loaded with molecular iodine (left) and a ^{64}Cuprogadonanotube (^{64}CuGNT) (right). **Left:** Each pair of orange spheres represents a molecule of iodine (I_2), drawn roughly to scale. **Right:** Green spheres represent Gd^{3+} ions and blue spheres represent Cu^{2+} ions, drawn roughly to scale.

DIAGNOSTIC IMAGING

The primary purposes of this section are to introduce another powerful diagnostic imaging technique (PET), describe the powerful information that arises when this technique is coupled with MRI (described extensively in **Chapter 2**), provide a summary of the state-of-the-art for combined PET/MRI agents and to summarize previous experiments which internalized molecular iodine (I_2) within US-tube nanocapsules.

Positron Emission Tomography

While MRI's resolution renders great anatomical and physiological information, its relative lack of sensitivity makes molecular imaging nearly impossible. Luckily, Nuclear Medicine (NM) offers high sensitivity combined with the accurate quantification required for efficient molecular imaging. More specifically, positron emission tomography (PET) has a sensitivity ranging from 100 to 1000 times higher than single photon emission computed tomography (SPECT), the second most sensitive NM technique.[191] PET

depends on the triangulation of annihilation photons following positron (β^+) decay from specific radionuclides. The most commonly-used PET radionuclides involve radioactive nonmetals, such as ^{15}O ($t_{1/2}$ = 2 min), ^{11}C ($t_{1/2}$ = 20 min), and the widely-used ^{18}F ($t_{1/2}$ = 2 h);[192] however, radiochemists are exploring various radiohalogens and radiometals as well,[193] such as ^{124}I ($t_{1/2}$ = 4.2 d), ^{86}Y ($t_{1/2}$ = 14.7 h), and ^{64}Cu ($t_{1/2}$ = 12.7 h), to capitalize on their extended half-lives for extended studies.

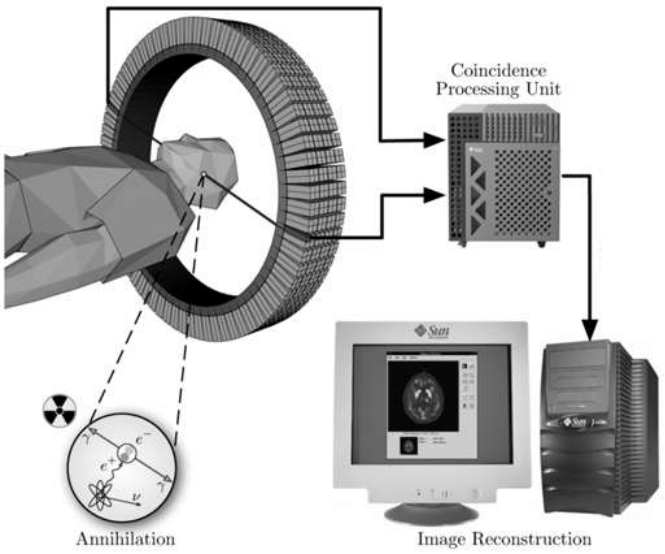

Figure 35: Positron Emission Tomography (PET) instrumentation. Beginning at "Annihilation" (where emitted β^+ annihilates neighboring e^-), continuing to a circular arrangement of scintillators which detects resultant γ-rays, concluding with coincidence processing required to extrapolate position of annihilation for image reconstruction.

As a β-emitting radioisotope decays, the escaping positron travels a short distance, known as 'positron range,' before annihilating with an electron to create 1.022 MeV of energy according to $E=mc^2$ (m being the combined mass of the annihilated positron and electron, see "Annihilation" in **Figure 35**).[194] This energy is divided evenly into two high-energy γ rays that emerge from the body away from each other at an 180° angle (± 0.25°).[195]

Outside of the body, these photons are then detected by an array of scintillators surrounding the patient. If the coincidence processing unit determines a pair of scintillator detectors simultaneously record γ rays, then the annihilation event is expected to have occurred somewhere between the detectors. After a specific number of annihilation events are recorded (typically over 100,000), the distribution of triangulated annihilations are reconstructed and displayed in a tomographic representation.

Multimodal Imaging

In many ways, positron emitting radionuclides are purely a CA at a physician's disposal that sacrifices resolution for specificity. While PET is considered one of the most sensitive diagnostic techniques, its lack of resolution can cause misleading anatomical information. For example, with spatial resolutions ranging 5-7 mm in clinical PET applications, a malignant tumor on the lung can easily be misdiagnosed as either stomach cancer or esophageal cancer. The image produced following a PET scan is simply color scaled voxels with the one color of the scale representing no activity, another representing the highest recorded activity in a single voxel, and all other colors representing a scale in between (most commonly white, black, and shades of grey). Unfortunately, there is no anatomical reference to apply to the image, but only reference to the circle of scintillators of the PET instrumentation (**Figure 35**). Imagine the hiker with a global position system (GPS) receiver, yet no map; he may know very intelligent information with regards to his location, yet still be completely lost in the woods without reference or bearings.

To alleviate this problem, the majority of current clinical PET instruments are used in "tandem" with a CT imager.[196] Using a maneuverable bed, an initial full-body (most scans ranging from head to hip) CT scan is taken for anatomical reference, followed by a PET scan for sensitive tracing. There are many advantages for using CT, instead of MRI, in conjunction with PET: the CT imager is only a fraction of the cost of an MRI imager, it takes under a minute for an anatomical reference scan, and the instrumentation is much less sensitive to its external surroundings.[197] Conversely, the are many disadvantages to a CT procedure: the patient receives harmful ionizing radiation, the CT provides low resolution scans when monitoring neural activity changes in brain scans compared to high resolution fMRI, and it lacks the contrast resolution required for enhanced tissue resolution.[198] Additionally, the radiation dangers associated with CT prevents the ability for repetitive scans that MRI allows.

For these reasons, there has been a race among researchers to create the first clinical MRI/PET multimodal imager with the first prototypes just now making their way into clinics.[199-201] Currently, images taken with an MRI scanner followed by separate images taken with a PET scanner have been overlaid to show great promise with regards to clarity, resolution, and identification of a radionuclide tracer. **Figure 36**, clearly shows the anatomic resolution of rat's body scan coupled with the amazing contrast that the targeted ^{124}I provides the tumor.[202]

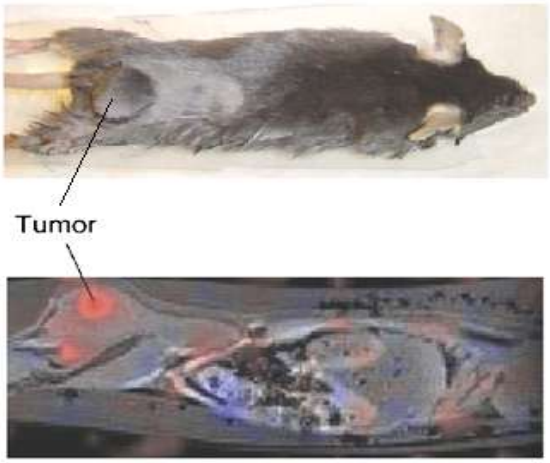

Figure 36: Colocalization of PET and MRI images. **Top:** External dorsal view showing position of tumor on lower back of mouse. **Bottom:** Sagittal MR image (linear grayscale) through the tumor of the mouse shown in top image overlaid with the corresponding PET data (blue-red color scale, adapted from [203]).

The disadvantage to this method is that the subject must be physically moved between images. This movement leads to inaccuracies when the images are overlaid, ultimately creating problems with localization. The first preclinical fused PET/MRI images were created in 2006 by Cherry's research group at the University of California, Davis,[204] and the potential strength of combining these two imaging modalities became readily apparent as shown in **Figure 37**:

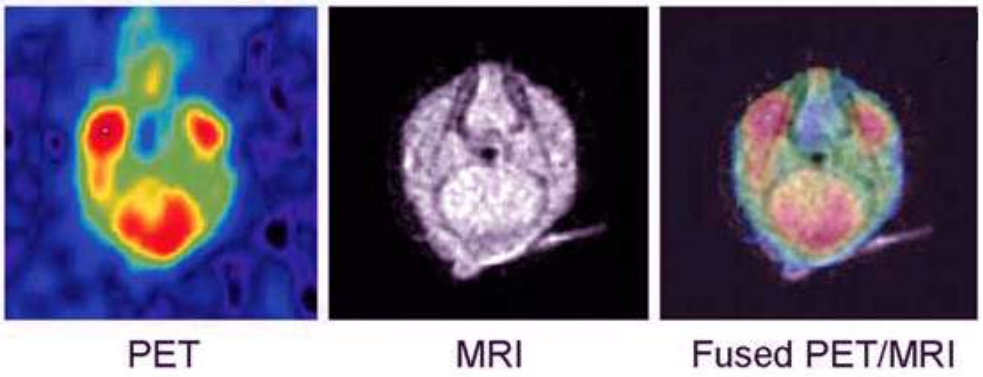

Figure 37: Simultaneous *in vivo* imaging with MRI and ^{18}F-fluorodeoxyglucose (FDG) PET of a rat, showing overlaid cross-sectional images through the head. FDG uptake in both muscle and brain is prominent (adapted from [204]).

These images show a cross-sectional brain scan of rat given ^{18}F-fluorodexoyglucose (FDG), a drug made to resemble glucose to monitor glucose uptake. The MRI scan gives both anatomical reference and resolution, while the PET image renders glucose uptake with incredible specificity. The overlay of the two shows the power of combined MRI/PET imaging.

Unfortunately, there are many obstacles in creating a clinical MRI/PET scanner. First, the magnet used in MRI is very sensitive to its surroundings. Simply having the PET instrumentation in close proximity can result in inhomogeneity of the magnetic field. Furthermore, the RF radiation emitted from a PET scanner can interfere with MRI measurements, especially if the RF is at any of the MRI scanner's resonant frequencies. Not only can the PET interfere with the MRI scan, but the opposite is also true, since the detectors in the circumference of the gantry of the PET scanner are comprised of photomultiplier tubes (PMTs) that are strongly susceptible to magnetic fields.[195] Despite all the inherent obstacles, one interesting benefit, discovered through Monte Carlo simulations, is that in the presence of a strong magnetic field (Tesla in strength), β^+ ranges will actually reduce the effective positron range of radionuclides,[205] suggesting that coupling the two instruments will enhance PET's resolution before computed overlay.

Most recently, on June 10, 2011 the FDA issued a press release clearing the Siemens Biograph mMR system, the first approved PET/MRI combined system. Previously, physicians could only use a PET and CT scanner to image the body. Repeating much of

the section above, the press release stated:

> "Advantages of the Siemens Biograph mMR system over current systems include simultaneous imaging, reduced radiation dose, and increased soft tissue contrast.
>
> 'The Siemens PET/MRI system allows two tests to run simultaneously without having to move the patient to a different scanning system,' Alberto Gutierrez, Ph.D., director of the Office of In Vitro Diagnostic Device Evaluation and Safety in the FDA's Center for Devices and Radiological Health. 'Minimizing changes in a patient's position between tests allows physicians to compare images more easily and helps them get the most accurate information possible.'"
>
> ~June 10, 2011 FDA Press Release

The first human MR-PET system installed in the U.S. was the 3T Seimens TIM Trio 60 cm (RF coil ID) 32 channel MRI at the Charlestown facility associated with the Athinoula A. Martinos Center (a collaborative center between Harvard University, Massachusets General Hospital, and Massachusetts Institute of Technology) in Boston, Massachusetts, shown in **Figure 38**.

Figure 38: First clinical MR-PET system installed in the U.S. (3T Seimens TIM Trio 60 cm (RF coil ID) 32 channel MRI).

Multimodal Imaging Agents

With MRI being the anatomical imager of choice by neurologists and the wealth of information stemming ^{18}FDG glucose uptake studies, fused images have been developed to combine this information into one powerful image, such as **Figure 37**.[202] Some physicians have even used MRI contrast agents for the MRI scans that they have overlaid PET scans atop.[206] Despite knowing the power of combining these imaging modalities, currently, no MRI/PET multimodal imaging agent has been developed.

The literature alludes to the design of single platform, dual PET/MRI imaging agents, yet however none have yet been reported. One reference is quite literally only an allusion to the eventual possibility of a nanoscale MRI/PET imaging agent: "It should be stressed that in PET imaging nanoparticles never have been used as a [CA] and this way can substantially increase the sensitivity and performance of this method both for animal and human studies, not mention their potential for multimodality."[207] The other two proposals in the literature involve taking previously reported nanoparticles functionalized with multiple DOTA chelating groups highlighting that DOTA binds strongly to either Gd^{3+} ion or $^{64}Cu^{2+}$ ion.[195]

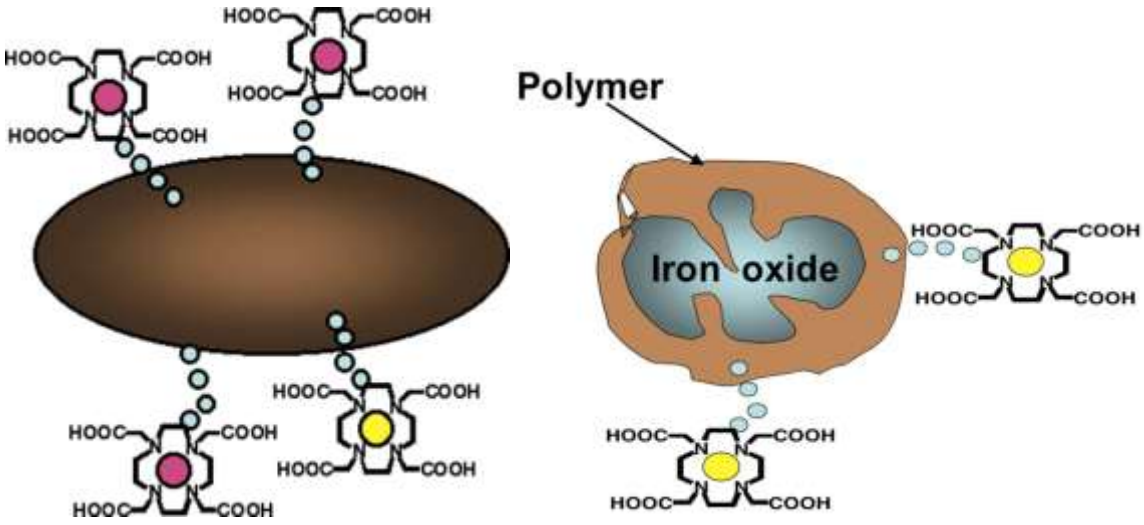

Figure 39: Proposed designs of dual PET/MRI imaging agents. **Left:** The brown oval represents bovine serum albumin (BSA) functionalized with DOTA chelating both $^{64}Cu^{2+}$ ion (represented by yellow circles) and Gd^{3+} ion (represented by pink circles) allowing for both PET and T_1-weighted MR imaging. **Right:** A dextran-sulfate-coated SPIO has been functionalized with DOTA chelating $^{64}Cu^{2+}$ ion (represented by yellow circles) allowing for both PET and T_2-weighted MR imaging (adapted from [208].

These are both reasonable approaches for creating multimodal MRI/PET agents. The first (**Figure 39, left**) follows attachment of isothiocyanate functionalized DOTA to a common blood serum protein, bovine serum Albumin (BSA). The other proposed method involves dextran sulfate coated SPIO conjugated (also via an isothiocyante reaction with a primary amine) to DOTA, capable of chelating $^{64}Cu^{2+}$ ions, as shown in **Figure 39, right**. The first proposal would have Gd^{3+} ion and $^{64}Cu^{2+}$ ion, causing it to be useful as both a MRI CA for T_1-weighted images along with PET images, and the other, with superparamagnetic SPIO instead of paramagnetic Gd^{3+} ions, should work for MRI CA for T_2-weighted images instead. Though not mentioned in the paper, for both T_1 and T_2 enhancement coupled with PET imaging, the group need only chelate Gd^{3+} ion along with $^{64}Cu^{2+}$ ion in the attached DOTA ligands. The problem with these two DOTA-functionalized precursors is simply that the precursors are already heavily functionalized,

making additional functionalization with targeting moieties, such as antibodies or targeting peptide sequences, especially difficult.

Through internalization of both PET radioisotopes and MRI CAs (useful for both T_1- and T_2-weighted enhancement) inside the US-tube nanocapsules, the exterior side wall of the nanocapsules remains unobstructed for functionalization with solubility-enhancing moieties to decrease the injected dose, targeting agents for enhanced diagnosis, and therapeutic agents, such as radiotherapeutics and chemotherapeutics. For this reason, the US-tube nanocapsules would seem to possess ideal potential for the development of forefront theranostic agents (therapeutic plus diagnostic, as described in **Chapter 1**).

Molecular and Mixed Halogens @ US-Tube Nanocapsules

The aim of the Part One of this chapter is to internalize $^{124}I_2$ (molecular iodine composed of positron-emitting [25.6%] radionuclides of iodine with a $t_{1/2}$ of 4.18 d) within the US-tube nanocapsules. To lay the groundwork for this experiment, three key experiments have been previously reported in the literature which internalized molecular iodine (I_2) and a mixed radiohalogen (^{225}AtCl) inside the US-tube nanocapsules:

The first, an internalization of I_2, simply involved sublimation of I_2 over the US-tube nanocapsules.[92] Using XPS and ICP-AES, the resultant I_2@US-tube nanocapsules are ca. 25% I_2 by mass after removing the externally-adsorbed I_2. The externally-adsorbed I_2 was removed by either (a) reduction of the I_2@US-tube nanocapsules with Na^0/THF or by (b) the heating of the I_2@US-tube nanocapsules to 300 °C. This technique, despite its

effectiveness, is not a possibility as the safety protocols at the Frensley Center for Imaging Research at Baylor College of Medicine (where the studies were performed) preclude the sublimation of radionuclides. However, the experiment did suggest that if $^{124}I_2$ could be successfully internalized within the US-tube nanocapsules, that it will likely be retained by the US-tube nanocapsule. Heating of the I_2@US-tube nanocapsules (following removal of the externally-adsorbed I_2) to 500 °C resulted in no measurable loss of I_2 by XPS or ICP-AES. Later studies revealed that the US-tube nanocapsules could be externally-functionalized with malonodiserinolamide (Ser) groups via Bingel chemistry rendering the water-soluble nanocapsules (ca. 0.25 mg/mL).[10] These water-solubilized I_2@US-tube nanocapsules are more than twice as opaque to X-rays as the empty US-tube nanocapsules.

The second important experiment examined US-tube nanocapsules with $^{125}I^-$ ions and oxidized $^{125}I_2$.[209] Both species ($^{125}I^-$ ions and oxidized $^{125}I_2$) were retained more strongly by US-tube nanocapsules than other carbonaceous materials tested: full-length SWNTs, fluorinated SWNTs, charcoal, graphite, and fluorinated graphite. This is believed to be owed, in part, to the US-tube nanocapsules' large surface area: 1180 m^2/g. The $t_{1/2}$ for $^{125}I^-$ ion retention to the US-tube nanocapsules calculated using the wash-off rate of iodine by pure water was ca. 4 months (2,720 h); meanwhile, the $t_{1/2}$ for $^{125}I_2$ retention following oxidation via 1 mM H_2O_2 was almost 2 years (14,300 h). This method of aqueous loading of radiohalides is more applicable for $^{124}I_2$, as it does not involve gas phase radionuclide during sublimation.

The third experiment followed the aqueous loading and subsequent oxidization above, however it was performed on the α-emitting $^{211}At^-$ ion with subsequent oxidation to $^{211}AtCl$ using the chemical oxidant Chloramine-T (ChT). ChT was utilized, as opposed to the H_2O_2 in the previous study, since ChT has been documented to form I_2 and not ICl, when oxidizing NaI.[210] This study also explored the internalization of stable, monoisotopic iodine (^{127}I) in the form of aqueous NaI oxidized to I_2 with ChT within both US-tube nanocapsules and full-length SWNTs. XPS and ICP-AES showed no internalization of I_2 within the full-length SWNTs. As the full-length SWNTs possess closed ends and lack the sidewall defects of the US-tube nanocapsules, this result is not unexpected. More importantly, however, is that the US-tube nanocapsules do retain the oxidized molecular iodine (I_2) at ca. 1.5-3 % by mass following washing with pure water. Moreover, as internally-loaded iodine and externally-physisorbed iodine have different Auger spectra (a high-energy shoulder at 520 keV would be expected if the iodine was externally-physisorbed), this aqueous loading of iodine is internal only (**Figure 39**). This aqueous loading of ionic radiohalogen, followed by oxidation with ChT, will also be followed in this part of the chapter below. Again, it should be noted that the first part of this chapter, while rendering promising results, was later abandoned due to high costs; the cost for the 1 mCi (10 μL) of $Na^{124}I$ utilized for the original study was over $5,000 (compared to 25.0 mCi of $^{64}CuCl_2$ in Part Two costing under $700).

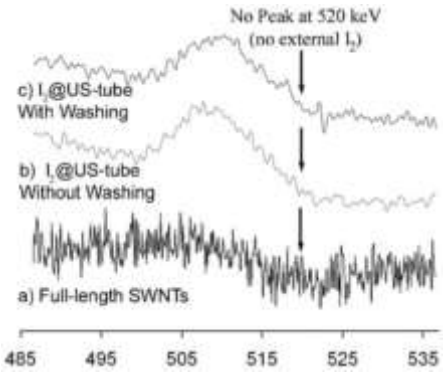

Figure 40: X-ray-induced Auger emission spectrum of nanotube materials (adapted from [92]).

PART ONE: PRELIMINARY ^{124}I EXPERIMENTS

Materials and Methods

US-tube Nanocapsules Solution

1.0 mL of HPLC-grade water was added to 1.0 mg of individualized US-tube nanocapsules (synthesized per **Chapter 1** from Arc-ablation synthesis, Carbolex AP-grade). To this, 1.0 mL of a 2% biocompatible Pluronic® F108 Block Copolymer (a nonionic surfactant composed of polyoxypropylene and polyoxyethylene, BASF Corporation) prepared with HPLC-grade was added and the solution was bath sonicated for 10 minutes. Subsequent centrifugation resulted in no flocculation, suggesting a complete suspension (ca. 0.5 mg US-tube nanocapsules/mL 1% Pluronic solution).

$^{124}I_2$@US-tube Nanocapsules

1.0 mg of US-tube nanocapsules were added to 1.0 mL of HPLC-grade water and bath sonicated for 5 min. While actively being sonicated, 200 μL (ca. 200 μg of US-tube nanocapsules) were added to 1.0 μCi of $Na^{124}I$ (ca. 33.3 pmol or 3.33 mM, radionuclide

purity > 99%, specific activity: 30 Ci/mmol, IBA Molecular North America, ca. 12 μL). This solution was bath sonicated for 10 min, followed by a 20 min rest to ensure equilibration. Then, 100 μL of a 0.30 M ChT solution was added to the initial solution and manually shaken in a sealed centrifuge vial. 300 μL of 2% biocompatible Pluronic® F108 Block Copolymer, followed by bath sonication for 10 min.

Limitations of ^{124}I

The relatively long half-life of ^{124}I (4.2 days) is beneficial since it allows for easy shipment (clinics need not have costly, on-site radioisotope production), and it permits further processing of the material (such as functionalization of the US-tube nanocapsules' sidewalls post-loading). Unfortunately, from another standpoint, this long half-life has serious negative consequences due to radionuclide handling regulations. Specifically, Baylor College of Medicine requires a period of 10 half-lives of decay prior to removing radiowaste from a laboratory for disposal. With a 4.2 d half-life, this equates to ca. 1.5 months of lab space being occupied with waste. This limitation also prevents membrane dialysis, since storage of radioactive waste water following dialysis is impractical.

Mouse Models

An athmyic nude mouse model was selected for stability since the inhibited immune system (missing thymus which results in no T-cell production) does not reject a tumor graft. All mice (both $^{124}I_2$@US-tube nanocapsules and $Na^{124}I$ control mice, n = 3 for both control and experiment) were tumor bearing with SKBR3, a common human breast

carcinoma cell line. For each set of three mice, two bore the tumor on the left leg and one on the right leg to ensure no difference with tumor location. Control mice were injected with ca. 466 μCi $Na^{124}I$ in 200 μL saline solution. Experimental mice were injected with ca. 333 μCi $^{124}I_2$@US-tube nanocapsules in 200 μL 1% Pluronic. All injections were intravenious, lateral tail vein with a 28 ga. needle.

MicroPET/CT Imaging

In vivo PET/CT imaging studies were performed using a Siemens INVEON small-animal imager with a dedicated PET scanner within a multimodality CT (Siemens Healthcare, Knoxville, TN). The CT imaging parameters included an X-ray voltage of 80 kV with an anode current of 500 μA and an exposure time of 260 milliseconds for each of the 120 rotation steps over a total rotation of 220° at low system magnification. A MicroCT image was taken of all mice pre-injection and 2 hr post-injection. After CT imaging, PET emission scans were performed at 1 hr, 4 hrs, and 24 hrs post-injection. Each PET scan had a 20 minute collection time. PET images were reconstructed using a two-dimensional filtered back-projection and CT images were reconstructed using a Feldkamp cone-beam algorithm with a ramp filter cutoff at the Nyquist frequency. Image fusion and analysis were performed using ASIPro, Inveon Research Workplace (Siemens Preclinical Solutions) and AMIRA (version 3.1; Konrad-Zuse-Zentrum fur Informationstechnik, Berlin, Germany).

Results

MicroCT

The MicroCT images showed no measurable CT enhancement from pre- to post-injection with the $^{124}I_2$@US-tube nanocapsules (**Figure 41**):

Figure 41: MicroCT image of athmyic nude mouse pre- and post-injection with prepared $^{124}I_2$@US-tube nanocapsule solution.

MicroPET

The result from the MicroPET imaging for the tumor-bearing mouse model injected with $^{124}I_2$@US-tube nanocapsule solution is visually displayed in **Figure 42**. At the 1 hr time-point, five distinct regions of activity appeared on the mouse: the mouth, the thyroid, the stomach, the bladder, and the tumor (**Figure 42, left**). The color scale represents the injected dose per gram of tissue (% ID/g) ranging from 0 % to 5 % of the total injected dose; color saturation is seen at thyroid, which has % ID/g of between 20% and 25%. At the 4 hr time-point, only four of these areas remained as the bladder no longer showed

activity (**Figure 42, center** and **Figure 43**). Note: the mice in **Figure 42** and **Figure 43** have tumors on opposite legs so as to ensure the tumor is not confused with the bladder. By the 24 hr time-point, most all activity was concentrated only in the thyroid (**Figure 42, right**).

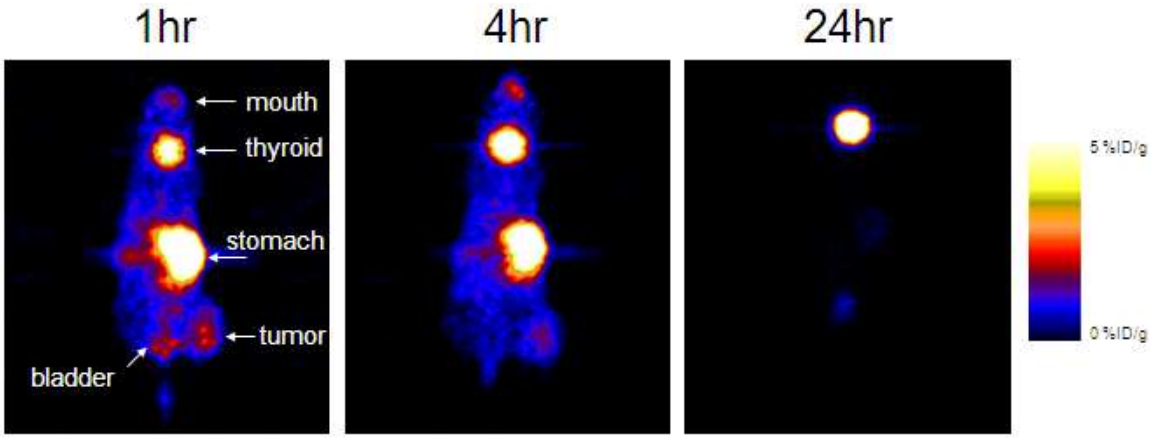

Figure 42: MicroPET image of athmyic nude mouse post-injection with prepared $^{124}I_2$@US-tube nanocapsule solution. Note: Tumor is on left leg.

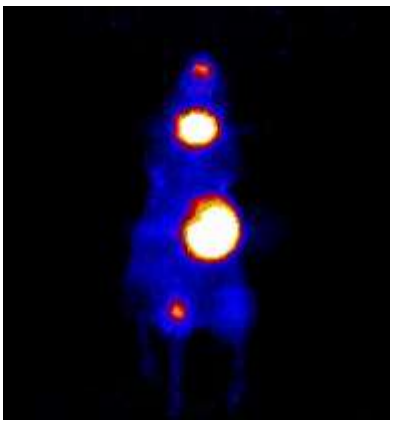

Figure 43: Four hour time-point MicroPET image of athmyic nude mouse post-injection with prepared $^{124}I_2$@US-tube nanocapsule solution. Note: Tumor is on right leg.

These results were visually identical to the control mice injected with $Na^{124}I$ in saline; with the only significant difference noted between the control and experimental mice being the % ID/g (normalized) at a 4 hr time-point data, as shown in **Figure 44**:

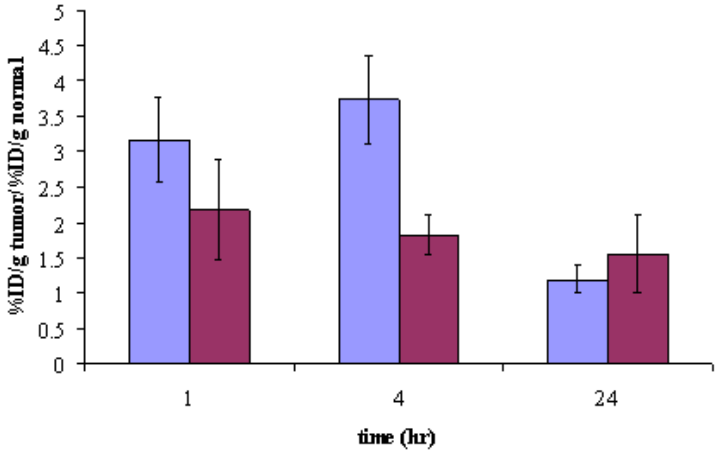

Figure 44: Tumor to background ratio. Light blue (left) represents mice injected with $^{124}I_2$@US-tube nanocapsule solution while purple (right) represents control mice injected with Na^{124}I solution. Raw data can be found in Appendix

Discussion

Unfortunately, this first round (and only round) of ^{124}I experiments was simply a preliminary study which had too many variables for firm conclusions to be reached:

(1) There was no washing of the US-tube nanocapsules post-oxidation with ChT to remove any weakly bound $^{124}I_2$. While previous studies suggested that the vast majority (if not all) of the I_2 was internalized (**Figure 40**), they also suggested that washing can remove a small amount I_2. It is possible that filtration and or membrane dialysis would have removed molecular iodine not strongly bound to the US-tube nanocapsules following oxidation.

(2) There was no washing of the US-tube nanocapsules post-oxidation with ChT to remove the ChT. It is unlikely that the small amount of oxidant would have

played a significant role in imaging; regardless, it should have been removed.

(3) The control didn't posses any Pluronic® to see if the surfactant played any role. Had the control contained an equal concentration of the surfactant, analysis of the interesting retention in the tumor at the 4 hour time-point could be more conclusively attributed to just the US-tube nanocapsules.

As such, this thesis will not attempt to draw many conclusions from this study. Again, cost was the number one reason for transitioning away from further $^{124}I_2$@US-tube nanocapsules experiments.

The interesting data stems from the 4 hour time-point. For all mouse models (n=3), the normalized % I.D. for the $^{124}I_2$@US-tube nanocapsules was nearly twice that of free $Na^{124}I$ in saline. As near-infrared (NIR) fluorescence spectra have suggested that blood proteins displace nanotube surfactant molecules within seconds,[211] it is likely that the only difference at the 4 hour time-point stems purely from the US-tube nanocapsules. Drs. Dai and Gambhir previously reported that nonspecific targeting of full-length SWNTs functionalized with the chemical polymer polyethylene glycol (PEG) is minimal, especially when compared to a the same material with the addition of a cancer targeting protein (specifically, using the arginine-glycine-asparatic acid (RGD) peptide capable of quantifying integrin $\alpha_v\beta_3$ expression in cancer patients).[212] This study used Raman spectroscopy to confirm similar results determined by covalently attaching the metal chelator ligand DOTA (1,4,7,10-tetraazacyclododecane-1,4,7,10- tetraacetic acid) to pegylated full-length SWNTs and chelating the PET-active $^{64}Cu^{2+}$ radionuclide.[213]

However, it is important to recall that the pristine nanotubes have a different biodistribution from functionalized nanotubes.[214] More specifically, functionalized, full-length SWNTs do not accumulate in RES organs,[215,216] while pristine full-length, ^{13}C-enriched SWNTs do.[214] Similarly, the US-tube nanocapsules have a different biodistribution from full-length SWNTs, escaping the reticuloendothelial system (RES) and being excreted through the kidneys and bile ducts.[74]

Conclusions

As stated above, few conclusions can be drawn from this preliminary study. As the bulk of the activity for both the control and the US-tube nanocapsules was displayed in the thyroid (there is no documented accumulation of nanotube materials in the thyroid), the most likely conclusion is that the majority of the $^{124}I_2$ was not retained within the US-tube nanocapsules. It remains unclear if this is due to a failure to properly oxidize the $Na^{124}I$ to $^{124}I_2$, or if the $^{124}I_2$ was leached from the US-tube nanocapsules when challenged *in vivo*. However, the data from the 4 hour time-point suggests further examination of untargeted US-tube nanocapsules may prove useful for time-points between 1 and 24 hours, since the US-tube nanocapsules is the most likely candidate for the increase in tumor retention of % I.D. The most likely reason for the increase in ^{124}I isotope in the solid tumor is the Enhanced Permeability and Retention (EPR) effect, a property of macromolecules and smaller particles to accumulate in tumor tissue due to poor fluid transport within tumors stemming from their rapid production of blood vessels.[217]

Ultimately, ^{124}I was simply too costly (and therefore impractical) for further examination;

examination of the US-tube nanocapsules ability to accumulate in solid tumors over time could prove advantageous for the development of US-tube nanocapsule-based imaging agents for nuclear medicine.

PART TWO: THE ^{64}Cu EXPERIMENTS

While the high cost of ^{124}I was the primary motivation for searching for a new PET radionuclide to encapsulate within the US-tube nanocapsules to develop a dual PET/MRI imaging agent, other advantages also arose from the selection of the ^{64}Cu radionuclide. The primary advantages of the ^{64}Cu radionuclide over the ^{124}I radionuclide are summarized in **Table 7** below.

Table 7: Comparison between the ^{124}I and ^{64}Cu PET radionuclides.

	^{124}I	^{64}Cu
Half-life:	4.2 days	12.7 hours
Modes of Decay:	26% β^+ emission 74% electron capture	26% β^+ emission 43% electron capture 39% beta decay
β^+ Range*:	2.4 mm	0.57 mm
Cost:	Approx. $6000 / mCi	Approx. $40 / mCi

*Positron Range determined in aqueous media

First, the ^{64}Cu radionuclide has the advantage of a significantly shorter half-life at 0.5

days as opposed to 4 days for ^{124}I. This half-life still allows for overnight shipment of the isotope, yet circumvents the issue of radioactive waste storage. Standard protocol at UTHSC (where these experiments were conducted) requires radionuclides to undergo 10 half-lives before disposal, which results in only a 5 day storage period for ^{64}Cu as opposed to a 41 day storage for ^{124}I. Second, while both radionuclides have the same % of β^+ emission (the decay mode visible through PET imaging), ^{64}Cu also undergoes β^- decay, as well. This mode of decay for ^{64}Cu has been employed as a radiotherapy agent for the treatment of cancer making this radionuclide an inherently theranostic agent.[218,219] Finally, ^{64}Cu has a significantly shorter positron range in aqueous media. The positron range is the average distance an emitted β^+ will travel before encountering an electron to annihilate. Important to note is that PET instrumentation does not triangulate the location of where the radionuclide decays but rather the location of where the β^+ annihilation occurs. Therefore, the longer the positron range, the more error in the resulting PET image. Also, as discussed extensively above, ^{64}Cu is a fraction of the cost of ^{124}I.

Methods and Materials

This section will describe the synthesis of Cu@US-tube nanocapsules, cold CuGNTs, and hot (radioactive) ^{64}CuGNTs. Additionally, this section describes the protocols used for simulating physiological challenges, as well as the imaging protocols used for both the MicroCT/PET and MR imaging.

Preparation of Cold Cu@US-tube Nanocapsules

Prior to tests with $^{64}CuCl_2$, cold copper(II) chloride (99.999% trace metals basis, Sigma)

was used to examine loading and retention of Cu^{2+} ions within the US-tube nanocapsules prepared as discussed in **Chapter 1**. Cu@US-tube nanocapsules were prepared following the same protocols found in **Chapter 2** for the GNTs. In short, a 5 mM solution of $CuCl_2$ was prepared using DI water. 15.0 mg of US-tube nanocapsules were added to 10.0 mL of $CuCl_2$ solution (in triplicate) and bath sonicated for 1 hr. Following sonication, the US-tube nanocapsules samples were filtered and washed seven times with DI water. The filtrate was analyzed via ICP-OES, the collected samples were dried overnight in an 80 °C, and the dried samples were digested as described in **Chapter 2** for ICP-OES analysis. All samples prepared in triplicate.

Preparation of Cold Cuprogadonanotubes (CuGNTs)

Cold cuprogadonanotubes were prepared identically to the Cu@US-tube nanocapsules described above except for the addition of $GdCl_3$ to the $CuCl_2$ solution. CuGNTs were prepared in solutions with varying ratios of Cu^{2+} ion to Gd^{3+} ion to study the effects of the ratio of ions in solution. Both 5 mM solutions of $CuCl_2$ and $GdCl_3$ were prepared using DI water, one with a 1:1 ratio of $CuCl_2$ to $GdCl_3$ and the other with a 1:4 ratio of $CuCl_2$ to $GdCl_3$. 15.0 mg of US-tube nanocapsules were added to 10.0 mL of each solution (in triplicate) and bath sonicated for 1 hr. All samples were filtered, washed, oven-dried, and analyzed via ICP-OES as described above for the Cu@US-tube nanocapsules.

Cold Cu@US-tube Nanocapsule and Cuprogadonanotube Challenges

The dried samples were introduced to *in vitro* challenges that would best simulate

conditions experienced *in vivo:* heat (37 °C), serum proteins (specifically bovine serum albumin or BSA), and phosphate buffered saline (PBS). Following 12 hr, 24 hr, and 7 d challenge experiments, the samples were filtered with a coarse-grade fritted glass filter and the filtrate was analyzed for both Cu^{2+} ion and Gd^{3+} ion via ICP-OES. All samples were challenged in triplicate. DI water, BSA, and PBS were also analyzed for Cu^{2+} ion and Gd^{3+} ion as controls for background levels.

Preparation of ^{64}Cuprogadonanotubes (^{64}CuGNTs)

Having established that Cu^{2+} ions leak from the US-tube nanocapsules without the presence of Gd^{3+} ions in the above cold experiments, all further loading was performed with only $GdCl_3$ and $^{64}CuCl_2$ mixtures. With the available concentration of $^{64}CuCl_2$ being on the picomolar scale in workable volumes, all further combinations were 5 mM $GdCl_3$ added to as much $^{64}CuCl_2$ as available (this traditionally was collaborator-dependent and varied from week to week). $^{64}CuCl_2$ was only available for shipment every 2 weeks, and project requirements took varying amounts each week. All samples were loaded with $^{64}CuCl_2$-spiked $GdCl_3$, with 2-15 mg of US-tube nanocapsules following the same loading protocol as for the CuGNTs. Filtration was performed in microcentrifugation filters as described in **Chapter 5**, using a 2 minute spin-down at 6,000 RPM. All washings involving hot ^{64}CuGNTs used 18 MΩ water for every set of experiments.

Many protocols were examined, but the final, most successful protocol involved addition of strong base at the end of the bath sonication. In short: 4.1 mCi of $^{64}CuCl_2$ was added to 6.2 mg of US-tube nanocapsules in 0.500 mL 1N HCl (aq) and bath sonicated for 30

mins. Then, 0.500 mL 1 mM $GdCl_3$ (aq) (pH ~ 5.2) was added and again the sample was bath sonicated for 30 minutes. After 60 minutes of equilibration, 0.600 mL 1N NaOH (aq) was added to ensure basic conditions. The samples were then transferred to microcentrifugation filters for initial spin downs, and the filtrate was examined for activity. Following the initial spin downs, all subsequent washings were with 18 MΩ water.

^{64}Cuprogadonanotube Challenges

Challenge experiments mimicked those of **Chapter 4**. The only variance was that 50% mouse serum was used instead of human plasma. All filtrations were performed in 1.5 mL microcentrifugation devices with a 100 kDa pore size. All samples were challenged for 24 hours in 1 x PBS (pH ~7.9) 40 °C or 50% mouse serum (pH ~7.5) for 24 hr challenge at 40 °C. All samples were challenged in triplicate and 1 % Pluronic and 1 % Tween-80 surfactants were compared.

MicroCT/PET Phantom Images

MicroCT and MicroPET imaging were performed on the same Siemens Inveon small-animal imager used above in **Part 1**. Each MicroPET scan was a 20 min collection. MR images were performed in both 1.5 T and 3.0 T systems. The phantoms were prepared at three concentrations (200 μCi/mL, 100 μCi/mL, and 50 μCi/mL) with Tween-80 surfactant and compared to blanks of DI water and Tween-80 surfactant.

3 T and 1.5 T MR Phantom Images

Phantom MR imaging was performed both a 1.5 T and 3.0 T commercial scanner (Achieva, Philips Medical Systems, Best, The Netherlands) with a 32-channel radiofrequency system. A 32- or 16-element phased-array surface coil was used for MR signal reception. An inversion recovery sequence was used for image acquisition with TR = 9000 ms and TE = 20 ms for 3 T images and TR = 6500 ms and TE = 10 ms for 1.5 T images.

Results and Discussion

Cold Cu^{2+}-ion Loading and Challenges

All loading techniques with cold copper(II) chloride only resulted in undetectable levels of Cu^{2+} ions in the filtrate of DI washings by the 7^{th} washing; moreover, these materials were 2.05 % (w/w) copper as determined via ICP-OES analysis. Unfortunately, significant (>45%) copper leakage occurred at 12 hr for PBS and BSA challenges at 40 °C, implying that Cu^{2+} ions are not stable within the US-tube nanocapsules under simulated *in vivo* challenge. At this point, all further attempts to internalize only Cu^{2+} ions within US-tube nanocapsules were abandoned.

All the samples prepared with cold $CuCl_2$ and $GdCl_3$ had no measurable Gd^{3+} ions or Cu^{2+} ions in the filtrate of DI washings by the 7^{th} washing. A 1:1 (Cu:Gd) loading ratio resulted in 0.70 % (w/w) copper in the final product, and a 1:4 ratio resulted in 0.38 % (w/w) copper. No measurable Gd^{3+} ions or Cu^{2+} ions leaked from the US-tube nanocapsules following *in vivo* simulated challenge for 7 days.

$^{64}Cu^{2+}$-ion Loading and Challenges

For the six 0.250 mL aliquots, the average activity was 470.5 μCi (or 1.88 μCi/μL). Following the initial spin-down, there was an average of 99.18% retention (or 0.92% of the $^{64}CuCl_2$ was removed). The subsequent washings resulted in 0.65 %, 0.49 %, and 0.23% of the activity removed. It should be noted that the 0.23 % sample had only 1 μCi of activity, which is the detection limit of the well counter used. Traditionally, 95% retention is considered viable for *in vivo* experiments, so the washings proved unnecessary.

There were no detectable levels of $^{64}Cu^{2+}$ ions in the filtrate of any of the samples after a 24 hour challenge at 40 °C in PBS, suggesting no problems with salt concentrations that could be encountered *in vivo.* Unfortunately, there was an average of 36.6% leakage at a 24 hour time point after being challenged in 50% mouse serum. All samples were then washed with 50 % mouse serum until no $^{64}Cu^{2+}$ ion was detected in the filtrate (an average of five washes), and these samples were then challenged again for 24 hours. At the following spin down, only 1-2 μCi (instrumental detection limit) occurred for the all of the samples. This agrees with the results in **Part 2** of **Chapter 4** that revealed there were two populations of $^{153}Gd^{3+}$ ions in ^{153}GNTs, one that could be removed and one that was stable to serum challenge. The initial MRI and PET images for the ^{64}CuGNTs are displayed in **Figure 45.**

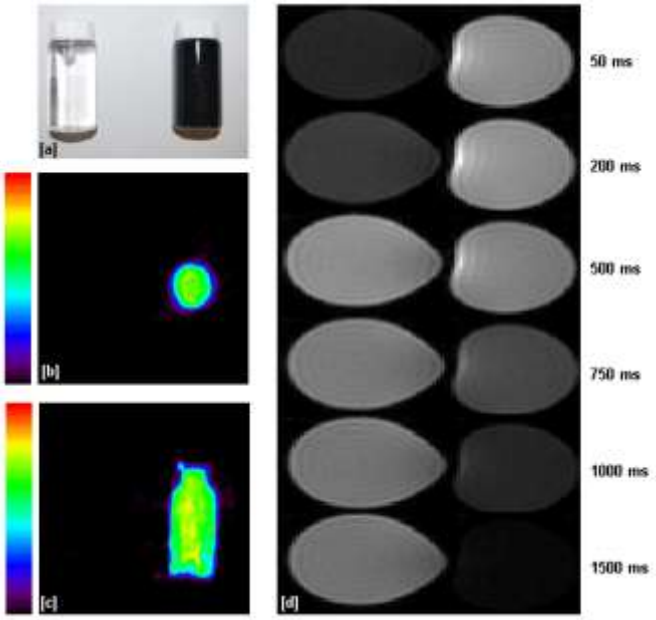

Figure 45: [a] Phantoms of DI water (left) and ^{64}CuGNTs (right). **[b]** Transverse MicroPET image of DI water (left) and ^{64}CuGNTs (right). **[c]** Coronal MicroPET image of DI water (left) and ^{64}CuGNTs (right). **[d]** MR images of DI water (left) and ^{64}CuGNTs (right) at various inversion times.

It should be noted that these samples may or may not be contaminated by free ^{64}Cu; initial iTLC measurements show 18.4 % leached copper (free $^{64}Cu^{2+}$), yet subsequent studies determined that the DOTA present in the iTLC protocol could remove even the Gd^{3+} ions from stable GNTs. For this reason, the images were repeated for the final, serum-washed ^{64}CuGNTs as shown in **Figures 46 and 47**.

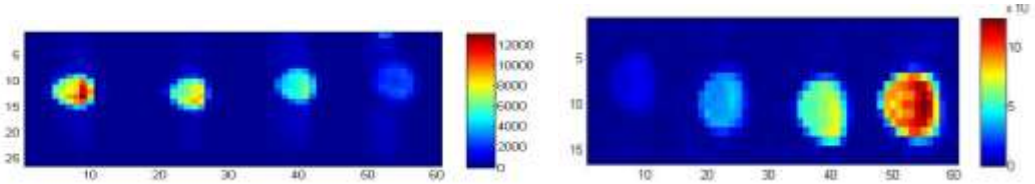

Figure 46: 3 T and 1.5 MR images of the ^{64}CuGNTs. **Left:** MR image of ^{64}CuGNTs at 200 μCi/mL, 100 μCi/mL, 50 μCi/mL, and 1% Tween-20 surfactant at 3 T. **Right:** MR image of 1% Tween-20 surfactant, ^{64}CuGNTs at 50 μCi/mL, 100 μCi/mL, and 200 μCi/mL at 1.5 T (note: order reversed).

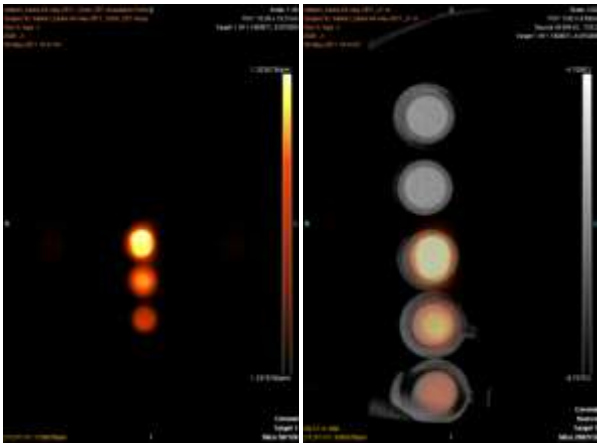

Figure 47: MicroPET and MicroCT images of ^{64}CuGNTs. **Left:** MicroPET of ^{64}CuGNTs at 200 μCi/mL, 100 μCi/mL, and 50 μCi/mL. **Right:** Same MicroPET with overlay of MicroCT. Uppermost phantom is 18 MΩ and the one below is 1% Tween-20 polysorbate surfactant.

The raw data and T_1 and T_2 for the MR images of **Figure 46** can be found in **Appendix VI**. The most important conclusion is that the ^{64}CuGNTs retain the high T_1-weighted relaxivity (52.7 $mM^{-1}s^{-1}$) expected for the GNT material (without copper). With so few Cu^{2+} ions present in the ^{64}CuGNTs, the lack of a significant change in T_1 relaxivity (the same as the GNT precursor batch at 53.4 $mM^{-1}s^{-1}$) was not unexpected.

Tween-20 was chosen as the surfactant because it better dispersed the US-tube nanocapsules, as shown in **Figure 48**. Though somewhat difficult to discern in the figure, the left (1% Pluronic F108) clearly shows the ring about the scintillation vial sidewall where the nanocapsules that flocculated out of solution remain, while better dispersion is evident on the right (1 % Tween-20).

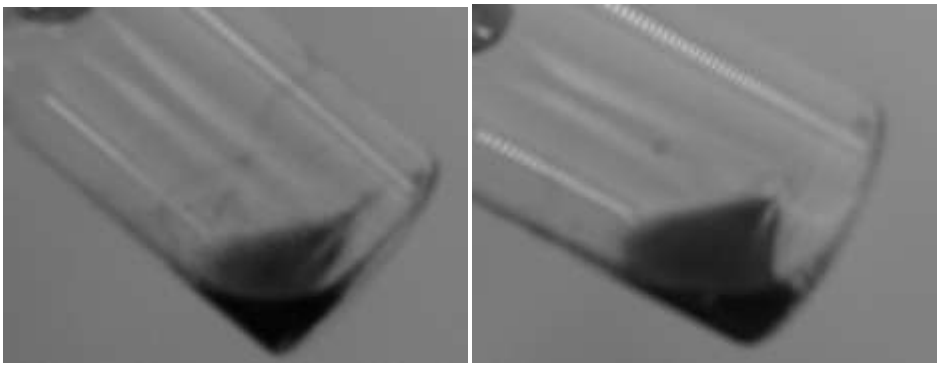

Figure 48: Comparison of surfactants. Left: 1 mg of ^{64}Cuprogadonanotubes suspended in 1% Pluronic F108. Right: 1 mg of ^{64}Cuprogadonanotubes suspended in 1 % Tween-20.

Conclusions

^{64}Cuprogadonanotubes washed with serum are a capable dual MRI-PET contrast agent that shows potential for being among the first targetable dual agents for the MRI-PET hardware systems that are only now coming online. Moreover, the requirement for the Gd^{3+} ions presence for a stable species (similar to the results found for $^{153}Gd^{3+}$ ions and $^{225}Ac^{3+}$ ions in **Chapter 4**) show the importance of the unique pH-dependent lanthanide ion chemistry for Gd^{3+} ions to form clusters within the US-tube nanocapsules that cannot be stripped away by simulated *in vivo* challenges.

CHAPTER SIX: CONCLUSIONS AND FUTURE WORK

"Better living through chemistry"

~Thomas Carlyle, Scottish Essayist

CONCLUSION

Few, if any, agents can boast the customizability of the US-tube nanocapsules. As the future ushers in medicine with unique objectives specific for each patient, the US-tube nanocapsules should remain on the forefront of targetable, therapeutic agent design. When filled with Gd^{3+}-ion clusters, the resulting GNTs are a powerful, dual modal MRI agent comprised of two magnetic components: (1) nanoscale, superparamagnetic catalyst particles that enhance T_2-weighted imaging and (2) nanoscale, paramagnetic Gd^{3+}-ion clusters that enhance T_1-weighted imaging. Additionally, the paramagnetic Gd^{3+}-ion clusters are stable to physiological challenges, including heat, human serum, and PBS as verified by the γ-emitting $^{153}Gd^{3+}$ ion used in the synthesis of ^{153}GNTs. Furthermore, the ability to select medically-active ions suitable to a patient's needs allows the US-tube nanocapsules to be among the first nanoscale theranostic agents for personalized medicine. The unique pH-dependent, lanthanide-ion chemistry that occurs within the US-tube nanocapsules has proven successful for the stable encapsulation of both $^{225}Ac^{3+}$ ions for α-radiotherapy and $^{64}Cu^{2+}$ ions for production of the first bimodal MRI/PET agent based on a SWNT material. For all of these reasons, the US-tube nanocapsules hold great promise for the future of personalized medicine.

FUTURE WORK

Future experiments will be designed to probe the true structure of the Gd^{3+}-ion clusters within the GNTs using high resolution x-ray study. Additionally, future experiments will explore the limitations of doping other medically-interesting ions within the Gd^{3+}-ion clusters (if any limitations exist). Finally, future studies will explore the successful targeting of the US-tube nanocapsules to diseased and/or cancerous cells.

APPENDIX I: ABBREVIATIONS AND SYMBOLS

@	within (x@y = x within y)
°C	degrees Celsius
Å	angstrom
AC	alternating current
AFM	atomic force microscopy
B_0	external magnetic field
BCM	Baylor College of Medicine
BSA	bovine serum albumin
CA	contrast agent
CGS	Gaussian centimeter, gram, second units
ChT	Chloramine-T
C_m	molar Curie constant
CoMoCat®	cobalt-molybdenum catalyzed SWNTs
conc.	concentrated
CT	computed tomography
CVD	chemical vapor deposition
d	day
DI	deionized
DOTA	1,4,7,10-tetraazacyclododecane-1,4,7,10-tetraacetic acid
DTPA	diethylene triamine pentaacetic acid
$E=mc^2$	mass-energy equivalence
EDS	energy dispersive X-ray spectroscopy
EDTA	ethylenediaminetetraacetic acid

eV	electronvolt
FC	field-cooled
FDA	Food and Drug Administration
FDG	fluorodeoxyglucose (^{18}F)
FFWW	fat-free body weight
fMRI	functional magnetic resonance imaging
G	gauss
ga.	gauge
GNTs	gadonanotubes or Gd@US-tube nanocapsules
GPS	global position system
H	magnetic field
hr	hour
H_c	coercive force
HiPCO	high-pressure carbon monoxide CVD process
HPLC	high-pressure liquid chromatography
HRTEM	high-resolution transmission electron microscopy
HSVM	high-speed vibration mill
ICP-OES	inductively-coupled plasma – optical emission spectroscopy
IPR	isolated pentagon rule
IR	infrared
IUPAC	International Union of Pure and Applied Chemistry
K	Kelvin
K	anisotropy energy density
k_B	Boltzmann constant
L	liter

LC	liquid chromatography
LDPE	low density polyethylene
LET	linear energy transfer
LNTs	lutetonanotubes or Lu@US-tube nanocapsules
M	magnetization
mAb	monoclonal antibody
MHRA	Medicines and Healthcare products Regulatory Agency
min	minute
m	meter
MPMS	Magnetic Property Measurement System
MRA	magnetic resonance angiography
M_{rem}	remnant magnetization
MRI	magnetic resonance imaging
M_s	saturation magnetization
MSC	mesenchymal stem cells
MWNT	multi-walled carbon nanotube
Nd:YAG	neodymium-doped yttrium aluminum garnet
NIR	near infrared spectroscopy
NM	nuclear medicine
NMR	nuclear magnetic resonance
NMV	net magnetization vector
NMWL	nominal molecular weight limit
NSF/NFD	nephrogenic systemic fibrosis/nephrogenic fibrosing dermopathy
Oe	Oersted
PET	positron emission tomography

PHA	Public Health Advisory
PMT	photomultiplier tube
ppb	parts per billion (microgram per liter)
ppm	parts per million (milligram per liter)
ppt	parts per thousand (gram per liter)
PTFE	polytetrafluoroethylene
RAIT	radioimmunotherapy
RBM	radial breathing mode
rem	Röntgen equivalents
RF	radio frequency
RT	room temperature
SEA	Shared Equipment Authority
SEM	scanning electron microscopy
Ser	malonodiserinolamide
SI	Système international d'unités (International System of Units)
SPECT	single photon emission computed tomography
SPIO	small particles of iron oxide
SQUID	superconducting quantum interference device
STM	scanning tunneling microscope
SWeNT	SouthWest NanoTechnologies Inc.
SWNT	single-walled carbon nanotube
T	Tesla
T_1	spin-lattice relaxation
T_2	spin-spin relaxation
$t_{1/2}$	half-life

TαT	targeted alpha therapy
T_B	blocking temperature
T_c	Curie temperature
TEM	transmission electron microscopy
TGA	thermal gravimetric analysis
THF	tetrahydrofuran
TαT	targeted α-particle therapy
V	volume
XPS	X-ray photoelectron spectroscopy
ZFC	zero-field-zooled
α	alpha particle ($^4He^{2+}$)
β-	beta particle (an electron)
β+	positron
γ	gamma emission
γ	gyromagnetic ratio
θ	angle
χ	magnetic susceptibility
ω	Larmor frequency or resonant frequency

APPENDIX II: GUIDELINES FOR QUOTATION OF EXCERPTS

This appendix is a direct copy of the 2008 *GUIDELINES FOR QUOTATION AND OTHER ACADEMIC USES OF EXCERPTS FROM JOURNAL ARTICLES (Version 2)* stating official guidelines for use of excerpts from scholarly journals according to The International Association of Scientific, Technical & Medical Publishers ("STM") and the Professional Scholarly & Publishing division of the Association of American Publishers ("PSP"):

"The International Association of Scientific, Technical & Medical Publishers ("STM") and the Professional Scholarly & Publishing division of the Association of American Publishers ("PSP") believe it is in the interest of the scholarly and professional community as well as scholarly and professional publishers, to set out some common principles with respect to the use of limited amounts of journal article content in other published academic works and for educational use, and to reduce legal uncertainty with respect to such uses. STM and PSP have with other trade associations recently published a White Paper in May 2007 on the general subject of academic re-use entitled Author and Publisher Rights For Academic Use: An Appropriate Balance.

Publishers accept that scholarly articles often require the direct reproduction of illustrative material (such as figures, tables, structures) for the purposes of discussion or comparison with other data, and that the electronic version of an article needs to contain the same illustrative material in order to maintain the authenticity of the record in both print and digital form. Publishers accept that the use of short quotations is normal in scholarship, generally intended to place the new work in scholarly context or to comment on the quoted work or its impact, and that there is minimal potential in such practices of negatively impacting the demand for the original work. Publishers also understand that in the development of course-

packs (including for distance education), whether in print or electronic form, universities often wish to use similar quotations or limited excerpts.

With respect to the use of small portions of journal articles by academics and scholars, or the institutions in which they conduct their research or educational work, that scholars (or their institutions with respect to course-packs) may (without obtaining explicit permission from publishers):

- *Use a maximum of two figures (including tables) from a journal article or five figures per journal volume (unless a separate copyright holder is identified in such figure, in which event permission should be sought from that holder);*
- *Use single text extracts of less than 100 words or series of text extracts totaling less than 300 words for quotation; and*
- *Use such excerpts in all media and in future editions.*

The following conditions apply:

- *The purpose of the use is scholarly comment or non-commercial research or educational use;*
- *Certain complex illustrations such as anatomical drawings; cartoons; maps; poetry; works of art; or photographs, will still require normal permissions requests of publishers (or other copyright holder) as the journal article author(s) is unlikely to own the copyright in these;*
- *Full credit should be given to the author(s) and publisher(s) of the material(s) used, consistent with normal scholarly practice; and*
- *The quotation or excerpt must never be modified.*

Note that some scholarly societies that own journals published on their behalf by another publisher may have more restrictive policies on permissions than those of the publisher, and the publisher, journal administrator or the journal's web site may need to be consulted with respect to such policies (check the copyright notice to see if there is a copyright owner other than the

publisher). These Guidelines are intended to help reduce legal uncertainty and improve and simplify administrative procedures with respect to the use of short excerpts of scholarly and professional information from journal articles. The participating publishers believe that by establishing clear guidance, research and scholarship as a whole is improved and scientific communication and education are made more effective and efficient.

Publisher signatories:

- *American Chemical Society*
- *BMJ Publishing Group Ltd*
- *Elsevier*
- *Institute of Physics*
- *International Union of Crystallography*
- *John Wiley & Sons (including Blackwell)*
- *Oxford University Press journals*
- *Portland Press Limited*
- *Royal Society of Chemistry*
- *SAGE Publications*
- *Springer Science+ Business Media*
- *Taylor & Francis"*

APPENDIX III: RAW MPMS DATA

Table 8: M(H) Data for Raw Arc SWNTs.

Field (T)	Field (Oe)	Long Moment (emu)	emu/g	emu/g of catalyst
0	0	0.027615	2.060792537	7
0	2000	0.103199	7.701447761	26
0	4000	0.112190	8.372373134	28
1	6000	0.114923	8.57630597	29
1	8000	0.116303	8.679335821	29
1	10000	0.117157	8.743074627	29
1	12000	0.117740	8.786597015	30
1	14000	0.118168	8.818522388	30
2	16000	0.118497	8.843074627	30
2	18000	0.118761	8.862776119	30
2	20000	0.119066	8.885514925	30
2	22000	0.119153	8.892037313	30
2	24000	0.119307	8.903492537	30
3	26000	0.119439	8.91338806	30
3	28000	0.119619	8.926776119	30
3	30000	0.119718	8.934186567	30
3	32000	0.119795	8.939940299	30
3	34000	0.119871	8.945559701	30
4	36000	0.119937	8.950507463	30
4	38000	0.119925	8.949634328	30
4	40000	0.119964	8.952567164	30
4	42000	0.120015	8.956328358	30
4	44000	0.120083	8.961440299	30
5	46000	0.120084	8.9615	30
5	48000	0.120093	8.962134328	30
5	50000	0.120194	8.969716418	30
5	48000	0.120167	8.967664179	30
5	46000	0.120184	8.968940299	30
4	44000	0.120156	8.966873134	30
4	42000	0.120038	8.958037313	30
4	40000	0.119990	8.954455224	30
4	38000	0.119940	8.950708955	30
4	36000	0.119960	8.952208955	30
3	34000	0.119818	8.941604478	30
3	32000	0.119755	8.936925373	30
3	30000	0.119683	8.931552239	30
3	28000	0.119661	8.929925373	30

3	26000	0.119558	8.922246269	30
2	24000	0.119323	8.904701493	30
2	22000	0.119185	8.894380597	30
2	20000	0.119106	8.888507463	30
2	18000	0.118644	8.854029851	30
2	16000	0.118547	8.846820896	30
1	14000	0.118229	8.823037313	30
1	12000	0.117797	8.790835821	30
1	10000	0.117238	8.74908209	29
1	8000	0.116369	8.684253731	29
1	6000	0.115020	8.583559701	29
0	4000	0.112310	8.381313433	28
0	2000	0.104726	7.815358209	26
0	0	0.050367	3.758716418	13
0	-2000	-0.101895	-7.604067164	-26
0	-4000	-0.112158	-8.369992537	-28
-1	-6000	-0.114919	-8.576007463	-29
-1	-8000	-0.116376	-8.684776119	-29
-1	-10000	-0.117233	-8.748761194	-29
-1	-12000	-0.117808	-8.791656716	-30
-1	-14000	-0.118235	-8.823470149	-30
-2	-16000	-0.118562	-8.847895522	-30
-2	-18000	-0.118826	-8.867626866	-30
-2	-20000	-0.119039	-8.883470149	-30
-2	-22000	-0.119216	-8.896738806	-30
-2	-24000	-0.119370	-8.908223881	-30
-3	-26000	-0.119499	-8.917858209	-30
-3	-28000	-0.119609	-8.926037313	-30
-3	-30000	-0.119719	-8.934276119	-30
-3	-32000	-0.119798	-8.940141791	-30
-3	-34000	-0.119866	-8.945253731	-30
-4	-36000	-0.119933	-8.950253731	-30
-4	-38000	-0.119991	-8.954529851	-30
-4	-40000	-0.120035	-8.957828358	-30
-4	-42000	-0.120081	-8.961253731	-30
-4	-44000	-0.120062	-8.959850746	-30
-5	-46000	-0.120064	-8.959985075	-30
-5	-48000	-0.120100	-8.962649254	-30
-5	-50000	-0.120121	-8.964276119	-30
-5	-48000	-0.120208	-8.970708955	-30
-5	-46000	-0.120093	-8.962164179	-30

-4	-44000	-0.120167	-8.967701493	-30
-4	-42000	-0.120030	-8.957432836	-30
-4	-40000	-0.119990	-8.9545	-30
-4	-38000	-0.119949	-8.95141791	-30
-4	-36000	-0.119873	-8.945708955	-30
-3	-34000	-0.119809	-8.941	-30
-3	-32000	-0.119745	-8.936208955	-30
-3	-30000	-0.119570	-8.923156716	-30
-3	-28000	-0.119579	-8.923791045	-30
-3	-26000	-0.119468	-8.915492537	-30
-2	-24000	-0.119352	-8.906835821	-30
-2	-22000	-0.119202	-8.895701493	-30
-2	-20000	-0.119028	-8.882679104	-30
-2	-18000	-0.118901	-8.873238806	-30
-2	-16000	-0.118665	-8.85558209	-30
-1	-14000	-0.118333	-8.830813433	-30
-1	-12000	-0.117818	-8.792350746	-30
-1	-10000	-0.117236	-8.748955224	-29
-1	-8000	-0.116395	-8.686186567	-29
-1	-6000	-0.115027	-8.584097015	-29
0	-4000	-0.112366	-8.385522388	-28
0	-2000	-0.104811	-7.821738806	-26
0	0	-0.050509	-3.769322388	-13
0	2000	0.101943	7.607686567	26
0	4000	0.112185	8.371977612	28
1	6000	0.114957	8.578843284	29
1	8000	0.116333	8.681567164	29
1	10000	0.117180	8.744776119	29
1	12000	0.117770	8.78880597	30
1	14000	0.118184	8.819686567	30
2	16000	0.118512	8.844164179	30
2	18000	0.118860	8.87011194	30
2	20000	0.119075	8.886179104	30
2	22000	0.119173	8.893529851	30
2	24000	0.119326	8.90491791	30
3	26000	0.119451	8.914261194	30
3	28000	0.119566	8.922820896	30
0	0	0.000151	0.011250716	0
0	200	0.017880	1.334332836	4
0	400	0.040280	3.005965672	10
0	600	0.056294	4.20101791	14

0	800	0.072551	5.414270149	18
0	1000	0.084247	6.287104478	21
0	1200	0.089007	6.642319403	22
0	1400	0.093032	6.942686567	23
0	1600	0.097777	7.296777612	25
0	1800	0.101300	7.559671642	25
0	2000	0.103840	7.749283582	26
0	2200	0.105243	7.85391791	26
0	2400	0.106446	7.943716418	27
0	2600	0.107460	8.019373134	27
0	2800	0.108348	8.085701493	27
0	3000	0.109268	8.154320896	27
0	4000	0.112207	8.373619403	28
1	5000	0.113819	8.49391791	29
1	6000	0.114937	8.577402985	29
1	7000	0.115709	8.635014925	29
1	8000	0.116301	8.679171642	29
1	9000	0.116770	8.714171642	29
1	10000	0.117153	8.742723881	29
1	7500	0.116034	8.659276119	29
1	5000	0.113879	8.498410448	29
0	2500	0.107617	8.031119403	27
0	2000	0.104699	7.81338806	26
0	1800	0.103169	7.699156716	26
0	1600	0.101357	7.563962687	25
0	1400	0.099134	7.398079851	25
0	1200	0.096405	7.194418657	24
0	1000	0.093037	6.943031343	23
0	800	0.088831	6.629208209	22
0	600	0.083529	6.233526866	21
0	400	0.076457	5.705710448	19
0	200	0.066615	4.971302239	17
0	0	0.050755	3.787665672	13
0	-200	0.022166	1.65414403	6
0	-2500	-0.106425	-7.942149254	-27
-1	-5000	-0.113822	-8.494156716	-29
-1	-7500	-0.116016	-8.657940299	-29
-1	-10000	-0.117143	-8.742014925	-29
-1	-7500	-0.116031	-8.659044776	-29
-1	-5000	-0.113892	-8.49941791	-29
0	-2500	-0.107678	-8.035664179	-27

0	-2000	-0.104781	-7.819485075	-26
0	-1750	-0.102851	-7.675477612	-26
0	-1500	-0.100396	-7.492246269	-25
0	-1250	-0.097229	-7.255926119	-24
0	-1000	-0.093200	-6.9552	-23
0	-750	-0.087833	-6.554697015	-22
0	-500	-0.080514	-6.008475373	-20
0	-250	-0.069756	-5.205669403	-17
0	0	-0.051113	-3.814380597	-13
0	250	-0.014031	-1.047079104	-4
0	500	0.026143	1.950981343	7
0	750	0.055388	4.133420896	14
0	1000	0.073985	5.521284328	19
0	1250	0.085606	6.388540299	21
0	1500	0.093135	6.950382836	23
0	1750	0.098216	7.329585075	25
0	2000	0.101830	7.599276119	26
0	2250	0.104486	7.797455224	26
0	2500	0.106469	7.945410448	27
0	2750	0.107992	8.059104478	27
0	3000	0.109194	8.148783582	27
0	-200	0.021875	1.632489552	5
0	-400	-0.011523	-0.859936567	-3
0	-600	-0.039866	-2.975041045	-10
0	-800	-0.060328	-4.502123881	-15
0	-1000	-0.074446	-5.555673134	-19
0	-1200	-0.084267	-6.288580597	-21
0	-1400	-0.091103	-6.798732836	-23
0	-1600	-0.096020	-7.16565597	-24
0	-1800	-0.099634	-7.435385075	-25
0	-2000	-0.102383	-7.640514925	-26

Table 9: M(H) Data for US-tube Nanocapsules.

Field (T)	Field (Oe)	Long Moment (emu)	emu/g	emu/g of catalyst
0	0	0.007206267	0.439406524	24.651981
0	100	0.009309825	0.567672256	31.848060
0	200	0.0119883	0.730993902	41.010878

0	300	0.01458613	0.889398171	49.897817
0	400	0.01654984	1.009136585	56.615490
0	500	0.01821808	1.110858537	62.322386
0	600	0.01966613	1.199154268	67.276033
0	700	0.02092132	1.275690244	71.569923
0	800	0.02202822	1.343184146	75.356527
0	900	0.02299573	1.402178659	78.666290
0	1000	0.023848	1.454146341	81.581828
0	2000	0.02978714	1.816289024	101.899083
0	4000	0.0323492	1.972512195	110.663656
1	6000	0.03337728	2.0352	114.180624
1	8000	0.03409056	2.078692683	116.620690
1	10000	0.03466011	2.113421341	118.569068
1	12000	0.03516192	2.144019512	120.285714
1	14000	0.03560226	2.170869512	121.792077
2	16000	0.03601002	2.195732927	123.186987
2	18000	0.03638837	2.218803049	124.481288
2	20000	0.03674952	2.24082439	125.716749
2	22000	0.03707451	2.260640854	126.828510
2	24000	0.03737551	2.278994512	127.858203
3	26000	0.03765223	2.295867683	128.804837
3	28000	0.03790776	2.31144878	129.678982
3	30000	0.03813078	2.325047561	130.441913
3	32000	0.0383482	2.338304878	131.185687
3	34000	0.03855152	2.350702439	131.881226
4	36000	0.0387284	2.361487805	132.486316
4	38000	0.03889152	2.371434146	133.044335
4	40000	0.03903016	2.379887805	133.518610
4	42000	0.03919085	2.389685976	134.068316
4	44000	0.03930434	2.396606098	134.456554
5	46000	0.0394347	2.404554878	134.902504
5	48000	0.03952765	2.410222561	135.220478
5	50000	0.03965056	2.417717073	135.640941
5	48000	0.03955506	2.411893902	135.314245
5	46000	0.03944436	2.405143902	134.935550
4	44000	0.03933035	2.398192073	134.545532
4	42000	0.03919285	2.389807927	134.075157
4	40000	0.03905559	2.381438415	133.605603
4	38000	0.03889159	2.371438415	133.044574
4	36000	0.03872806	2.361467073	132.485153
3	34000	0.03856011	2.35122622	131.910612

3	32000	0.03835836	2.33892439	131.220443
3	30000	0.03815059	2.326255488	130.509681
3	28000	0.03791591	2.311945732	129.706862
3	26000	0.03766305	2.296527439	128.841851
2	24000	0.03738273	2.279434756	127.882902
2	22000	0.03708943	2.26155061	126.879550
2	20000	0.03675662	2.241257317	125.741037
2	18000	0.03640343	2.219721341	124.532807
2	16000	0.03602979	2.196938415	123.254618
1	14000	0.0356213	2.172030488	121.857211
1	12000	0.03517716	2.14494878	120.337849
1	10000	0.03468534	2.114959756	118.655378
1	8000	0.03411804	2.080368293	116.714696
1	6000	0.0334182	2.037695122	114.320608
0	4000	0.03242111	1.976896951	110.909654
0	2000	0.03025973	1.845105488	103.515770
0	0	0.01297439	0.791121341	44.384202
0	-2000	-0.02968115	-1.80982622	-101.536501
0	-4000	-0.03233251	-1.971494512	-110.606561
-1	-6000	-0.0333843	-2.035628049	-114.204639
-1	-8000	-0.0340906	-2.078695122	-116.620826
-1	-10000	-0.0346607	-2.113457317	-118.571086
-1	-12000	-0.03515934	-2.143862195	-120.276888
-1	-14000	-0.03560541	-2.171061585	-121.802853
-2	-16000	-0.03601295	-2.195911585	-123.197010
-2	-18000	-0.0363918	-2.219012195	-124.493021
-2	-20000	-0.03674375	-2.240472561	-125.697010
-2	-22000	-0.03707252	-2.260519512	-126.821702
-2	-24000	-0.03737737	-2.279107927	-127.864566
-3	-26000	-0.03765699	-2.296157927	-128.821121
-3	-28000	-0.03790281	-2.311146951	-129.662048
-3	-30000	-0.03813417	-2.325254268	-130.453510
-3	-32000	-0.03834959	-2.338389634	-131.190442
-3	-34000	-0.03854722	-2.350440244	-131.866516
-4	-36000	-0.03873435	-2.36185061	-132.506671
-4	-38000	-0.03889001	-2.371342073	-133.039169
-4	-40000	-0.03904624	-2.380868293	-133.573618
-4	-42000	-0.03918617	-2.38940061	-134.052306
-4	-44000	-0.03931521	-2.397268902	-134.493740
-5	-46000	-0.03945867	-2.406016463	-134.984503
-5	-48000	-0.03954424	-2.411234146	-135.277230

-5	-50000	-0.03964573	-2.417422561	-135.624418
-5	-50000	-0.03962424	-2.416112195	-135.550903
-5	-48000	-0.03955354	-2.41180122	-135.309045
-5	-46000	-0.03944484	-2.405173171	-134.937192
-4	-44000	-0.03931826	-2.397454878	-134.504174
-4	-42000	-0.03919797	-2.390120122	-134.092672
-4	-40000	-0.03908606	-2.383296341	-133.709839
-4	-38000	-0.03890988	-2.372553659	-133.107143
-4	-36000	-0.03873839	-2.362096951	-132.520491
-3	-34000	-0.03855655	-2.351009146	-131.898433
-3	-32000	-0.03835992	-2.339019512	-131.225780
-3	-30000	-0.03817092	-2.327495122	-130.579228
-3	-28000	-0.03791258	-2.311742683	-129.695471
-3	-26000	-0.03766233	-2.296483537	-128.839388
-2	-24000	-0.03738474	-2.279557317	-127.889778
-2	-22000	-0.03707885	-2.260905488	-126.843357
-2	-20000	-0.03676147	-2.241553049	-125.757629
-2	-18000	-0.03640417	-2.219766463	-124.535338
-2	-16000	-0.03602747	-2.196796951	-123.246682
-1	-14000	-0.03562053	-2.171983537	-121.854577
-1	-12000	-0.03517669	-2.144920122	-120.336241
-1	-10000	-0.03468146	-2.114723171	-118.642105
-1	-8000	-0.03411801	-2.080366463	-116.714594
-1	-6000	-0.03341917	-2.037754268	-114.323926
0	-4000	-0.03241594	-1.976581707	-110.891968
0	-2000	-0.03026116	-1.845192683	-103.520662
0	0	-0.01300334	-0.792886585	-44.483238
0	2000	0.02967516	1.809460976	101.516010
0	4000	0.03233261	1.97150061	110.606903
1	6000	0.03337687	2.035175	114.179221
1	8000	0.03408342	2.078257317	116.596264
1	10000	0.03466186	2.113528049	118.575055
1	12000	0.03515979	2.143889634	120.278428
1	14000	0.03560569	2.171078659	121.803811
2	16000	0.03601271	2.195896951	123.196189
2	18000	0.03638897	2.218839634	124.483340
2	20000	0.03674504	2.24055122	125.701423
2	22000	0.03707625	2.260746951	126.834462
2	24000	0.03737444	2.278929268	127.854543
3	26000	0.03765122	2.295806098	128.801382
3	28000	0.03790955	2.311557927	129.685105

3	30000	0.03813174	2.325106098	130.445197
3	32000	0.03833687	2.337614024	131.146928
3	34000	0.03854309	2.350188415	131.852388
4	36000	0.03872627	2.361357927	132.479030
4	38000	0.0388899	2.371335366	133.038793
4	40000	0.03903876	2.380412195	133.548030
4	42000	0.0391824	2.389170732	134.039409
4	44000	0.03930926	2.396906098	134.473385
5	46000	0.03940902	2.402989024	134.814655
5	48000	0.0395023	2.408676829	135.133758

Table 10: M(H) Data for GNTs.

Field (Oe)	Temp (K)	Long Moment (emu)	emu/g	emu/g of catalyst
0	5	0.005172031	0.315367744	25.437886
100	5	0.006704644	0.408819756	32.975821
200	5	0.00861478	0.525291463	42.370549
300	5	0.01048227	0.639162805	51.555528
400	5	0.01190106	0.72567439	58.533642
500	5	0.01310437	0.799046951	64.451948
600	5	0.01416125	0.863490854	69.650059
700	5	0.01505289	0.917859146	74.035461
800	5	0.0158538	0.966695122	77.974621
900	5	0.01654783	1.009014024	81.388107
1000	5	0.01717349	1.047164024	84.465326
2000	5	0.0214734	1.309353659	105.613811
4000	5	0.02328765	1.419978659	114.536937
6000	5	0.02399894	1.46335	118.035314
8000	5	0.02449423	1.49355061	120.471326
10000	5	0.02488873	1.517605488	122.411617
12000	5	0.02522589	1.538164024	124.069890
14000	5	0.02552768	1.556565854	125.554200
16000	5	0.02579338	1.572767073	126.861007
18000	5	0.02604643	1.588196951	128.105597
20000	5	0.02628165	1.602539634	129.262493
22000	5	0.02649947	1.615821341	130.333809
24000	5	0.02670329	1.62824939	131.336268
26000	5	0.02687302	1.63859878	132.171060

28000	5	0.02703905	1.648722561	132.987655
30000	5	0.02718716	1.657753659	133.716113
32000	5	0.02730373	1.664861585	134.289445
34000	5	0.02744873	1.673703049	135.002607
36000	5	0.02756098	1.680547561	135.554692
38000	5	0.02766357	1.686803049	136.059266
40000	5	0.02775994	1.692679268	136.533248
42000	5	0.02780606	1.695491463	136.760083
44000	5	0.02792305	1.702625	137.335481
46000	5	0.02798032	1.706117073	137.617155
48000	5	0.02811337	1.714229878	138.271542
50000	5	0.02813486	1.715540244	138.377238
48000	5	0.02805435	1.710631098	137.981261
46000	5	0.0279885	1.706615854	137.657387
44000	5	0.02792157	1.702534756	137.328202
42000	5	0.02786144	1.698868293	137.032461
40000	5	0.02778209	1.694029878	136.642190
38000	5	0.02766111	1.686653049	136.047167
36000	5	0.02756769	1.680956707	135.587694
34000	5	0.02746516	1.674704878	135.083415
32000	5	0.02733201	1.666585976	134.428536
30000	5	0.02719778	1.65840122	133.768345
28000	5	0.02706758	1.650462195	133.127976
26000	5	0.02687885	1.638954268	132.199734
24000	5	0.02670642	1.628440244	131.351662
22000	5	0.02651032	1.616482927	130.387173
20000	5	0.0262789	1.602371951	129.248967
18000	5	0.02605966	1.589003659	128.170667
16000	5	0.02581602	1.574147561	126.972359
14000	5	0.02553857	1.557229878	125.607761
12000	5	0.02524054	1.539057317	124.141944
10000	5	0.02490484	1.518587805	122.490852
8000	5	0.02451908	1.495065854	120.593547
6000	5	0.02404032	1.465873171	118.238835
4000	5	0.02333865	1.423088415	114.787773
2000	5	0.02181036	1.3299	107.271100
0	5	0.009276926	0.56566622	45.627218
-2000	5	-0.02139143	-1.304355488	-105.210653
-4000	5	-0.0232859	-1.419871951	-114.528330
-6000	5	-0.02401088	-1.464078049	-118.094039
-8000	5	-0.02450444	-1.494173171	-120.521542

-10000	5	-0.02487997	-1.517071341	-122.368532
-12000	5	-0.02522362	-1.53802561	-124.058725
-14000	5	-0.02552399	-1.556340854	-125.536052
-16000	5	-0.02579701	-1.572988415	-126.878861
-18000	5	-0.02604836	-1.588314634	-128.115090
-20000	5	-0.02628359	-1.602657927	-129.272034
-22000	5	-0.02649885	-1.615783537	-130.330759
-24000	5	-0.02669388	-1.62767561	-131.289986
-26000	5	-0.0268734	-1.638621951	-132.172929
-28000	5	-0.02703936	-1.648741463	-132.989180
-30000	5	-0.02719149	-1.658017683	-133.737409
-32000	5	-0.02731079	-1.665292073	-134.324169
-34000	5	-0.02744798	-1.673657317	-134.998918
-36000	5	-0.02754024	-1.679282927	-135.452685
-38000	5	-0.02766301	-1.686768902	-136.056512
-40000	5	-0.02776318	-1.692876829	-136.549184
-42000	5	-0.02784291	-1.697738415	-136.941324
-44000	5	-0.02791467	-1.702114024	-137.294265
-46000	5	-0.02798152	-1.706190244	-137.623057
-48000	5	-0.02804758	-1.710218293	-137.947964
-50000	5	-0.02810264	-1.71357561	-138.218768
-50000	5	-0.02809338	-1.713010976	-138.173224
-48000	5	-0.02804987	-1.710357927	-137.959227
-46000	5	-0.02799214	-1.706837805	-137.675290
-44000	5	-0.0279191	-1.702384146	-137.316054
-42000	5	-0.02784795	-1.698045732	-136.966113
-40000	5	-0.02774129	-1.691542073	-136.441521
-38000	5	-0.02766639	-1.686975	-136.073136
-36000	5	-0.02756868	-1.681017073	-135.592563
-34000	5	-0.02745612	-1.674153659	-135.038953
-32000	5	-0.02733267	-1.66662622	-134.431782
-30000	5	-0.02719603	-1.658294512	-133.759738
-28000	5	-0.02705455	-1.649667683	-133.063889
-26000	5	-0.02688635	-1.639411585	-132.236622
-24000	5	-0.02670639	-1.628438415	-131.351515
-22000	5	-0.02651096	-1.616521951	-130.390321
-20000	5	-0.02629509	-1.603359146	-129.328595
-18000	5	-0.0260617	-1.589128049	-128.180700
-16000	5	-0.02581024	-1.573795122	-126.943931
-14000	5	-0.02553941	-1.557281098	-125.611893
-12000	5	-0.0252411	-1.539091463	-124.144698

-10000	5	-0.02490974	-1.518886585	-122.514952
-8000	5	-0.02452358	-1.495340244	-120.615680
-6000	5	-0.02403903	-1.465794512	-118.232491
-4000	5	-0.02335182	-1.423891463	-114.852548
-2000	5	-0.02182169	-1.330590854	-107.326825
0	5	-0.009314422	-0.567952561	-45.811637
2000	5	0.02139782	1.304745122	105.242081
4000	5	0.0233115	1.421432927	114.654240
6000	5	0.02401863	1.46455061	118.132156
8000	5	0.02450396	1.494143902	120.519182
10000	5	0.02488248	1.51722439	122.380877
12000	5	0.02523069	1.538456707	124.093498
14000	5	0.02553066	1.556747561	125.568857
16000	5	0.02580276	1.573339024	126.907141
18000	5	0.02605583	1.588770122	128.151830
20000	5	0.02628929	1.603005488	129.300069
22000	5	0.02650613	1.616227439	130.366565
24000	5	0.02670128	1.628126829	131.326382
26000	5	0.02688735	1.639472561	132.241540
28000	5	0.02704095	1.648838415	132.997000
30000	5	0.02719071	1.657970122	133.733573
32000	5	0.02731798	1.665730488	134.359532
34000	5	0.02745407	1.674028659	135.028871
36000	5	0.02757904	1.68164878	135.643518
38000	5	0.02766428	1.686846341	136.062758
40000	5	0.02773483	1.691148171	136.409748
42000	5	0.02784691	1.697982317	136.960997
44000	5	0.02779741	1.694964024	136.717539
46000	5	0.02795679	1.704682317	137.501426
48000	5	0.02805154	1.710459756	137.967440

Table 11: M(H) Data for LNTs.

Field (Oe)	Temp (K)	Long Moment (emu)	emu/g	emu/g of catalyst
0	5	0.005172031	0.315367744	25.437886
100	5	0.006704644	0.408819756	32.975821
200	5	0.00861478	0.525291463	42.370549
300	5	0.01048227	0.639162805	51.555528
400	5	0.01190106	0.72567439	58.533642

500	5	0.01310437	0.799046951	64.451948
600	5	0.01416125	0.863490854	69.650059
700	5	0.01505289	0.917859146	74.035461
800	5	0.0158538	0.966695122	77.974621
900	5	0.01654783	1.009014024	81.388107
1000	5	0.01717349	1.047164024	84.465326
2000	5	0.0214734	1.309353659	105.613811
4000	5	0.02328765	1.419978659	114.536937
6000	5	0.02399894	1.46335	118.035314
8000	5	0.02449423	1.49355061	120.471326
10000	5	0.02488873	1.517605488	122.411617
12000	5	0.02522589	1.538164024	124.069890
14000	5	0.02552768	1.556565854	125.554200
16000	5	0.02579338	1.572767073	126.861007
18000	5	0.02604643	1.588196951	128.105597
20000	5	0.02628165	1.602539634	129.262493
22000	5	0.02649947	1.615821341	130.333809
24000	5	0.02670329	1.62824939	131.336268
26000	5	0.02687302	1.63859878	132.171060
28000	5	0.02703905	1.648722561	132.987655
30000	5	0.02718716	1.657753659	133.716113
32000	5	0.02730373	1.664861585	134.289445
34000	5	0.02744873	1.673703049	135.002607
36000	5	0.02756098	1.680547561	135.554692
38000	5	0.02766357	1.686803049	136.059266
40000	5	0.02775994	1.692679268	136.533248
42000	5	0.02780606	1.695491463	136.760083
44000	5	0.02792305	1.702625	137.335481
46000	5	0.02798032	1.706117073	137.617155
48000	5	0.02811337	1.714229878	138.271542
50000	5	0.02813486	1.715540244	138.377238
48000	5	0.02805435	1.710631098	137.981261
46000	5	0.0279885	1.706615854	137.657387
44000	5	0.02792157	1.702534756	137.328202
42000	5	0.02786144	1.698868293	137.032461
40000	5	0.02778209	1.694029878	136.642190
38000	5	0.02766111	1.686653049	136.047167
36000	5	0.02756769	1.680956707	135.587694
34000	5	0.02746516	1.674704878	135.083415
32000	5	0.02733201	1.666585976	134.428536
30000	5	0.02719778	1.65840122	133.768345

28000	5	0.02706758	1.650462195	133.127976
26000	5	0.02687885	1.638954268	132.199734
24000	5	0.02670642	1.628440244	131.351662
22000	5	0.02651032	1.616482927	130.387173
20000	5	0.0262789	1.602371951	129.248967
18000	5	0.02605966	1.589003659	128.170667
16000	5	0.02581602	1.574147561	126.972359
14000	5	0.02553857	1.557229878	125.607761
12000	5	0.02524054	1.539057317	124.141944
10000	5	0.02490484	1.518587805	122.490852
8000	5	0.02451908	1.495065854	120.593547
6000	5	0.02404032	1.465873171	118.238835
4000	5	0.02333865	1.423088415	114.787773
2000	5	0.02181036	1.3299	107.271100
0	5	0.009276926	0.56566622	45.627218
-2000	5	-0.02139143	-1.304355488	-105.210653
-4000	5	-0.0232859	-1.419871951	-114.528330
-6000	5	-0.02401088	-1.464078049	-118.094039
-8000	5	-0.02450444	-1.494173171	-120.521542
-10000	5	-0.02487997	-1.517071341	-122.368532
-12000	5	-0.02522362	-1.53802561	-124.058725
-14000	5	-0.02552399	-1.556340854	-125.536052
-16000	5	-0.02579701	-1.572988415	-126.878861
-18000	5	-0.02604836	-1.588314634	-128.115090
-20000	5	-0.02628359	-1.602657927	-129.272034
-22000	5	-0.02649885	-1.615783537	-130.330759
-24000	5	-0.02669388	-1.62767561	-131.289986
-26000	5	-0.0268734	-1.638621951	-132.172929
-28000	5	-0.02703936	-1.648741463	-132.989180
-30000	5	-0.02719149	-1.658017683	-133.737409
-32000	5	-0.02731079	-1.665292073	-134.324169
-34000	5	-0.02744798	-1.673657317	-134.998918
-36000	5	-0.02754024	-1.679282927	-135.452685
-38000	5	-0.02766301	-1.686768902	-136.056512
-40000	5	-0.02776318	-1.692876829	-136.549184
-42000	5	-0.02784291	-1.697738415	-136.941324
-44000	5	-0.02791467	-1.702114024	-137.294265
-46000	5	-0.02798152	-1.706190244	-137.623057
-48000	5	-0.02804758	-1.710218293	-137.947964
-50000	5	-0.02810264	-1.71357561	-138.218768
-50000	5	-0.02809338	-1.713010976	-138.173224

-48000	5	-0.02804987	-1.710357927	-137.959227
-46000	5	-0.02799214	-1.706837805	-137.675290
-44000	5	-0.0279191	-1.702384146	-137.316054
-42000	5	-0.02784795	-1.698045732	-136.966113
-40000	5	-0.02774129	-1.691542073	-136.441521
-38000	5	-0.02766639	-1.686975	-136.073136
-36000	5	-0.02756868	-1.681017073	-135.592563
-34000	5	-0.02745612	-1.674153659	-135.038953
-32000	5	-0.02733267	-1.66662622	-134.431782
-30000	5	-0.02719603	-1.658294512	-133.759738
-28000	5	-0.02705455	-1.649667683	-133.063889
-26000	5	-0.02688635	-1.639411585	-132.236622
-24000	5	-0.02670639	-1.628438415	-131.351515
-22000	5	-0.02651096	-1.616521951	-130.390321
-20000	5	-0.02629509	-1.603359146	-129.328595
-18000	5	-0.0260617	-1.589128049	-128.180700
-16000	5	-0.02581024	-1.573795122	-126.943931
-14000	5	-0.02553941	-1.557281098	-125.611893
-12000	5	-0.0252411	-1.539091463	-124.144698
-10000	5	-0.02490974	-1.518886585	-122.514952
-8000	5	-0.02452358	-1.495340244	-120.615680
-6000	5	-0.02403903	-1.465794512	-118.232491
-4000	5	-0.02335182	-1.423891463	-114.852548
-2000	5	-0.02182169	-1.330590854	-107.326825
0	5	-0.009314422	-0.567952561	-45.811637
2000	5	0.02139782	1.304745122	105.242081
4000	5	0.0233115	1.421432927	114.654240
6000	5	0.02401863	1.46455061	118.132156
8000	5	0.02450396	1.494143902	120.519182
10000	5	0.02488248	1.51722439	122.380877
12000	5	0.02523069	1.538456707	124.093498
14000	5	0.02553066	1.556747561	125.568857
16000	5	0.02580276	1.573339024	126.907141
18000	5	0.02605583	1.588770122	128.151830
20000	5	0.02628929	1.603005488	129.300069
22000	5	0.02650613	1.616227439	130.366565
24000	5	0.02670128	1.628126829	131.326382
26000	5	0.02688735	1.639472561	132.241540
28000	5	0.02704095	1.648838415	132.997000
30000	5	0.02719071	1.657970122	133.733573
32000	5	0.02731798	1.665730488	134.359532

34000	5	0.02745407	1.674028659	135.028871
36000	5	0.02757904	1.68164878	135.643518
38000	5	0.02766428	1.686846341	136.062758
40000	5	0.02773483	1.691148171	136.409748
42000	5	0.02784691	1.697982317	136.960997
44000	5	0.02779741	1.694964024	136.717539
46000	5	0.02795679	1.704682317	137.501426
48000	5	0.02805154	1.710459756	137.967440

Table 12: M(T) Data for raw SWNTs.

Field (Oe)	Temperature (K)	Long Moment (emu)	emu/g	emu/g of catalyst
1000	2	0.077045	5.749621642	19.319965
1000	3	0.078205	5.83619403	19.610867
1000	4	0.079043	5.898707463	19.820926
1000	5	0.079783	5.953990299	20.006688
1000	6	0.080505	6.007842537	20.187643
1000	7	0.081200	6.059696269	20.361883
1000	8	0.081647	6.093047015	20.473948
1000	9	0.082119	6.128264179	20.592286
1000	10	0.082538	6.159542537	20.697388
1000	2	0.080789	6.029030597	20.258839
1000	3	0.081322	6.068827612	20.392566
1000	4	0.081815	6.105616418	20.516184
1000	5	0.082145	6.130259701	20.598991
1000	6	0.082478	6.155087313	20.682417
1000	7	0.082804	6.179437313	20.764238
1000	8	0.082989	6.193201493	20.810489
1000	9	0.083198	6.208786567	20.862858
1000	10	0.083403	6.22408209	20.914254
1000	15	0.084397	6.29830597	21.163663
1000	20	0.085144	6.354016418	21.350862
1000	25	0.085694	6.395041045	21.488713
1000	30	0.086037	6.420700746	21.574935
1000	35	0.086331	6.44264403	21.648669
1000	40	0.086554	6.459254478	21.704484
1000	45	0.086706	6.470570149	21.742507
1000	50	0.086797	6.477389552	21.765422
1000	55	0.086844	6.480904478	21.777233
1000	60	0.086858	6.481945522	21.780731

1000	65	0.086839	6.480495522	21.775859
1000	70	0.086788	6.476723881	21.763185
1000	75	0.086714	6.471189552	21.744589
1000	80	0.086614	6.463720149	21.719490
1000	85	0.086490	6.45448209	21.688448
1000	90	0.086341	6.443332836	21.650984
1000	95	0.086178	6.431181343	21.610152
1000	100	0.085998	6.41776194	21.565060
1000	2	0.091302	6.813595522	22.895146
1000	3	0.091250	6.809689552	22.882021
1000	4	0.091177	6.804270896	22.863813
1000	5	0.091131	6.800841791	22.852291
1000	6	0.091080	6.796998507	22.839377
1000	7	0.091031	6.793342537	22.827092
1000	8	0.090981	6.78961791	22.814576
1000	9	0.090929	6.785735075	22.801529
1000	10	0.090880	6.78209403	22.789294
1000	15	0.090641	6.764248507	22.729330
1000	20	0.090402	6.746430597	22.669458
1000	25	0.090162	6.728502985	22.609217
1000	30	0.089918	6.710291045	22.548021
1000	35	0.089666	6.691523881	22.484959
1000	40	0.089412	6.672546269	22.421190
1000	45	0.089158	6.653553731	22.357371
1000	50	0.088896	6.634058955	22.291865
1000	55	0.088633	6.614373881	22.225719
1000	60	0.088366	6.594476119	22.158858
1000	65	0.088095	6.574239552	22.090859
1000	70	0.087822	6.553856716	22.022368
1000	75	0.087544	6.533162687	21.952832
1000	80	0.087259	6.511849254	21.881214
1000	85	0.086969	6.490248507	21.808631
1000	90	0.086675	6.468272388	21.734786
1000	95	0.086377	6.446009701	21.659979
1000	100	0.086090	6.424660448	21.588241
1000	105	0.085861	6.407548507	21.530741
1000	110	0.085654	6.392117164	21.478888
1000	115	0.085435	6.375764179	21.423939
1000	120	0.085221	6.359775373	21.370213
1000	125	0.085013	6.344229851	21.317977
1000	130	0.084818	6.329729851	21.269254

1000	135	0.084642	6.316587313	21.225092
1000	140	0.084490	6.305220149	21.186896
1000	145	0.084360	6.295537313	21.154359
1000	150	0.084238	6.286453731	21.123836
1000	155	0.084121	6.277673134	21.094332
1000	160	0.083992	6.268037313	21.061953
1000	165	0.083877	6.259510448	21.033301
1000	170	0.083762	6.250861194	21.004238
1000	175	0.083636	6.241466418	20.972669
1000	180	0.083499	6.231287313	20.938465
1000	185	0.083374	6.221914179	20.906970
1000	190	0.083236	6.211656716	20.872502
1000	195	0.083079	6.199899254	20.832995
1000	200	0.082934	6.189130597	20.796810
1000	205	0.082748	6.17519403	20.749980
1000	210	0.082560	6.161196269	20.702944
1000	215	0.082394	6.148832836	20.661401
1000	220	0.082191	6.133671642	20.610456
1000	225	0.082016	6.120576119	20.566452
1000	230	0.081834	6.106978358	20.520761
1000	235	0.081644	6.092833582	20.473231
1000	240	0.081430	6.07686194	20.419563
1000	245	0.081210	6.060416418	20.364302
1000	250	0.080976	6.042969403	20.305677
1000	255	0.080721	6.023936567	20.241722
1000	260	0.080444	6.003271642	20.172284
1000	265	0.080140	5.980607463	20.096127
1000	270	0.079844	5.958518657	20.021904
1000	275	0.079519	5.934247015	19.940346
1000	280	0.079192	5.909873134	19.858445
1000	285	0.078869	5.885718657	19.777280
1000	290	0.078564	5.862984328	19.700888
1000	295	0.078249	5.839470149	19.621876
1000	300	0.077919	5.814887313	19.539272

Table 13: M(T) Data for US-tube nanocapsules.

Field (Oe)	Temperature (K)	Long Moment (emu)	emu/g
10	5	0.090	0.739
10	10	0.090	0.739
10	15	0.090	0.741
10	20	0.090	0.742
10	25	0.090	0.744
10	30	0.090	0.745
10	35	0.090	0.744
10	40	0.089	0.737
10	45	0.088	0.725
10	50	0.086	0.711
10	55	0.085	0.697
10	60	0.083	0.682
10	65	0.081	0.667
10	70	0.079	0.652
10	75	0.077	0.638
10	80	0.076	0.624
10	85	0.074	0.610
10	90	0.072	0.596
10	95	0.071	0.583
10	100	0.069	0.570
10	105	0.068	0.558
10	110	0.066	0.546
10	115	0.065	0.536
10	120	0.064	0.526
10	125	0.063	0.516
10	130	0.062	0.507
10	135	0.061	0.499
10	140	0.060	0.490
10	145	0.059	0.483
10	150	0.058	0.476
10	155	0.057	0.470
10	160	0.056	0.463
10	165	0.056	0.457
10	170	0.055	0.452
10	176	0.054	0.446
10	181	0.054	0.441
10	186	0.053	0.436
10	191	0.052	0.431
10	196	0.052	0.426

10	201	0.051	0.422
10	206	0.051	0.418
10	211	0.050	0.413
10	216	0.050	0.408
10	221	0.049	0.404
10	226	0.049	0.400
10	231	0.048	0.396
10	236	0.048	0.392
10	241	0.047	0.389
10	246	0.047	0.385
10	251	0.046	0.382
10	256	0.046	0.378
10	261	0.045	0.374
10	266	0.045	0.370
10	271	0.045	0.367
10	276	0.044	0.364
10	281	0.044	0.360
10	286	0.043	0.356
10	291	0.043	0.353
10	296	0.042	0.350
10	301	0.042	0.346
10	5	0.050	0.412
10	10	0.050	0.411
10	15	0.050	0.410
10	20	0.050	0.409
10	25	0.050	0.409
10	30	0.050	0.408
10	35	0.049	0.407
10	40	0.049	0.406
10	45	0.049	0.405
10	50	0.049	0.404
10	55	0.049	0.403
10	60	0.049	0.402
10	65	0.049	0.401
10	70	0.049	0.401
10	75	0.049	0.400
10	80	0.048	0.399
10	85	0.048	0.398
10	90	0.048	0.397
10	95	0.048	0.396
10	100	0.048	0.395

10	105	0.048	0.394
10	110	0.048	0.392
10	115	0.048	0.392
10	120	0.048	0.391
10	125	0.047	0.390
10	130	0.047	0.389
10	135	0.047	0.388
10	140	0.047	0.387
10	145	0.047	0.385
10	150	0.047	0.384
10	155	0.047	0.384
10	160	0.046	0.383
10	165	0.046	0.379
10	170	0.046	0.380
10	175	0.046	0.379
10	181	0.046	0.378
10	186	0.046	0.377
10	191	0.046	0.376
10	196	0.045	0.375
10	201	0.045	0.373
10	206	0.045	0.372
10	211	0.045	0.371
10	216	0.045	0.370
10	221	0.045	0.368
10	226	0.045	0.367
10	231	0.044	0.366
10	236	0.044	0.364
10	241	0.044	0.363
10	246	0.044	0.362
10	251	0.044	0.360
10	256	0.044	0.359
10	261	0.043	0.358
10	266	0.043	0.356
10	271	0.043	0.355
10	276	0.043	0.353
10	281	0.043	0.351
10	286	0.042	0.350
10	291	0.042	0.348
10	296	0.042	0.346
10	301	0.042	0.344
100	5	0.054	0.447

100	10	0.055	0.456
100	15	0.057	0.467
100	20	0.058	0.477
100	25	0.059	0.488
100	30	0.061	0.499
100	35	0.062	0.509
100	40	0.063	0.518
100	45	0.064	0.527
100	50	0.065	0.536
100	55	0.066	0.544
100	60	0.067	0.553
100	65	0.068	0.561
100	70	0.069	0.569
100	75	0.070	0.577
100	80	0.071	0.584
100	85	0.072	0.591
100	90	0.073	0.599
100	95	0.074	0.605
100	100	0.074	0.612
100	105	0.075	0.618
100	110	0.076	0.624
100	115	0.076	0.629
100	120	0.077	0.635
100	125	0.078	0.640
100	130	0.078	0.645
100	135	0.079	0.649
100	140	0.079	0.654
100	145	0.080	0.658
100	150	0.080	0.662
100	155	0.081	0.665
100	160	0.081	0.669
100	165	0.082	0.673
100	170	0.082	0.676
100	176	0.082	0.679
100	181	0.083	0.682
100	186	0.083	0.684
100	191	0.083	0.686
100	196	0.084	0.688
100	201	0.084	0.690
100	206	0.084	0.691
100	211	0.084	0.693

100	216	0.084	0.694
100	221	0.084	0.695
100	226	0.084	0.695
100	231	0.084	0.696
100	236	0.085	0.696
100	241	0.085	0.697
100	246	0.085	0.697
100	251	0.085	0.696
100	256	0.085	0.696
100	261	0.084	0.696
100	266	0.084	0.695
100	271	0.084	0.694
100	276	0.084	0.694
100	281	0.084	0.693
100	286	0.084	0.691
100	291	0.084	0.690
100	296	0.084	0.689
100	301	0.083	0.687
100	5	0.093	0.767
100	10	0.093	0.765
100	15	0.093	0.764
100	20	0.093	0.763
100	25	0.092	0.761
100	30	0.092	0.760
100	35	0.092	0.759
100	40	0.092	0.758
100	45	0.092	0.757
100	50	0.092	0.756
100	55	0.092	0.755
100	60	0.092	0.754
100	65	0.091	0.753
100	70	0.091	0.753
100	75	0.091	0.752
100	80	0.091	0.752
100	85	0.091	0.751
100	90	0.091	0.750
100	95	0.091	0.749
100	100	0.091	0.748
100	105	0.091	0.747
100	110	0.091	0.745
100	115	0.090	0.744

100	120	0.090	0.743
100	125	0.090	0.741
100	130	0.090	0.740
100	135	0.090	0.739
100	140	0.090	0.737
100	145	0.089	0.736
100	150	0.089	0.734
100	155	0.089	0.733
100	160	0.089	0.732
100	165	0.089	0.731
100	170	0.089	0.730
100	176	0.089	0.729
100	181	0.088	0.728
100	186	0.088	0.726
100	191	0.088	0.725
100	196	0.088	0.724
100	201	0.088	0.722
100	206	0.088	0.721
100	211	0.087	0.720
100	216	0.087	0.718
100	221	0.087	0.717
100	226	0.087	0.716
100	231	0.087	0.714
100	236	0.087	0.713
100	241	0.086	0.711
100	246	0.086	0.710
100	251	0.086	0.708
100	256	0.086	0.706
100	261	0.086	0.705
100	266	0.085	0.703
100	271	0.085	0.701
100	276	0.085	0.699
100	281	0.085	0.697
100	286	0.084	0.695
100	291	0.084	0.693
100	296	0.084	0.691
100	301	0.084	0.689
1000	5	0.200	1.647
1000	10	0.201	1.652
1000	15	0.201	1.657
1000	20	0.202	1.660

1000	25	0.202	1.663
1000	30	0.202	1.664
1000	35	0.202	1.665
1000	40	0.202	1.666
1000	45	0.202	1.667
1000	50	0.202	1.667
1000	55	0.202	1.667
1000	60	0.202	1.668
1000	65	0.203	1.668
1000	70	0.203	1.668
1000	75	0.203	1.668
1000	80	0.203	1.669
1000	85	0.203	1.668
1000	90	0.203	1.668
1000	95	0.203	1.668
1000	100	0.202	1.667
1000	105	0.202	1.667
1000	110	0.202	1.666
1000	115	0.202	1.666
1000	120	0.202	1.665
1000	125	0.202	1.664
1000	130	0.202	1.662
1000	135	0.202	1.662
1000	140	0.202	1.660
1000	145	0.201	1.659
1000	150	0.201	1.657
1000	155	0.201	1.656
1000	160	0.201	1.655
1000	165	0.201	1.654
1000	170	0.201	1.653
1000	176	0.201	1.652
1000	181	0.200	1.650
1000	186	0.200	1.649
1000	191	0.200	1.649
1000	196	0.200	1.648
1000	201	0.200	1.646
1000	206	0.200	1.645
1000	211	0.200	1.644
1000	216	0.199	1.642
1000	221	0.199	1.641
1000	226	0.199	1.639

1000	231	0.199	1.637
1000	236	0.199	1.635
1000	241	0.198	1.633
1000	246	0.198	1.631
1000	251	0.198	1.630
1000	256	0.198	1.628
1000	261	0.197	1.625
1000	266	0.197	1.623
1000	271	0.197	1.621
1000	276	0.197	1.619
1000	281	0.196	1.616
1000	286	0.196	1.614
1000	291	0.196	1.611
1000	296	0.195	1.608
1000	301	0.195	1.605
1000	5	0.206	1.699
1000	10	0.206	1.694
1000	15	0.205	1.691
1000	20	0.205	1.690
1000	25	0.205	1.689
1000	30	0.205	1.688
1000	35	0.205	1.687
1000	40	0.205	1.685
1000	45	0.205	1.684
1000	50	0.204	1.683
1000	55	0.204	1.682
1000	60	0.204	1.681
1000	65	0.204	1.680
1000	70	0.204	1.680
1000	75	0.204	1.679
1000	80	0.204	1.678
1000	85	0.204	1.677
1000	90	0.204	1.676
1000	95	0.203	1.676
1000	100	0.203	1.675
1000	105	0.203	1.674
1000	110	0.203	1.673
1000	115	0.203	1.671
1000	120	0.203	1.671
1000	125	0.203	1.669
1000	130	0.202	1.667

1000	135	0.202	1.666
1000	140	0.202	1.664
1000	145	0.202	1.663
1000	150	0.202	1.661
1000	155	0.202	1.660
1000	160	0.201	1.659
1000	165	0.201	1.658
1000	171	0.201	1.657
1000	176	0.201	1.656
1000	181	0.201	1.655
1000	186	0.201	1.653
1000	191	0.201	1.652
1000	196	0.200	1.651
1000	201	0.200	1.650
1000	206	0.200	1.648
1000	211	0.200	1.647
1000	216	0.200	1.645
1000	221	0.200	1.644
1000	226	0.199	1.642
1000	231	0.199	1.640
1000	236	0.199	1.638

Table 14: M(T) Data for GNTs.

Field (Oe)	Temperature (K)	Long Moment (emu)	emu/g
10	5	0.001	0.016
10	10	0.001	0.016
10	15	0.001	0.017
10	20	0.001	0.019
10	25	0.001	0.019
10	30	0.001	0.023
10	35	0.001	0.025
10	40	0.001	0.027
10	45	0.001	0.028
10	50	0.001	0.030
10	55	0.001	0.032
10	60	0.001	0.034
10	65	0.001	0.035

10	70	0.001	0.038
10	75	0.001	0.039
10	80	0.002	0.040
10	85	0.002	0.042
10	90	0.002	0.043
10	95	0.002	0.044
10	100	0.002	0.046
10	105	0.002	0.047
10	110	0.002	0.048
10	115	0.002	0.050
10	120	0.002	0.051
10	125	0.002	0.052
10	130	0.002	0.053
10	135	0.002	0.054
10	140	0.002	0.055
10	145	0.002	0.057
10	150	0.002	0.058
10	155	0.002	0.059
10	160	0.002	0.060
10	165	0.002	0.061
10	170	0.002	0.062
10	175	0.002	0.063
10	181	0.002	0.064
10	186	0.002	0.065
10	191	0.002	0.066
10	196	0.003	0.067
10	201	0.002	0.064
10	206	0.003	0.068
10	211	0.003	0.069
10	216	0.003	0.070
10	221	0.003	0.071
10	226	0.003	0.072
10	231	0.003	0.073
10	236	0.003	0.073
10	241	0.003	0.074
10	246	0.003	0.075
10	251	0.003	0.075
10	256	0.003	0.083
10	261	0.003	0.077
10	266	0.003	0.079
10	271	0.003	0.078

10	276	0.003	0.079
10	281	0.003	0.079
10	286	0.003	0.080
10	291	0.003	0.080
10	296	0.003	0.081
10	301	0.003	0.082
10	5	0.005	0.130
10	10	0.005	0.128
10	15	0.005	0.127
10	20	0.005	0.126
10	25	0.005	0.126
10	30	0.005	0.125
10	35	0.005	0.124
10	40	0.005	0.123
10	45	0.005	0.122
10	50	0.005	0.122
10	55	0.005	0.121
10	60	0.005	0.120
10	65	0.005	0.119
10	70	0.004	0.117
10	75	0.004	0.117
10	80	0.004	0.116
10	85	0.004	0.115
10	90	0.004	0.115
10	95	0.004	0.114
10	100	0.004	0.113
10	105	0.004	0.112
10	110	0.004	0.111
10	115	0.004	0.110
10	120	0.005	0.129
10	125	0.004	0.108
10	130	0.004	0.107
10	135	0.004	0.107
10	140	0.004	0.106
10	145	0.004	0.105
10	150	0.004	0.104
10	155	0.004	0.103
10	160	0.004	0.102
10	165	0.004	0.102
10	171	0.004	0.101
10	176	0.004	0.100

10	181	0.004	0.099
10	186	0.004	0.099
10	191	0.004	0.098
10	196	0.004	0.097
10	201	0.004	0.097
10	206	0.004	0.096
10	211	0.004	0.095
10	216	0.004	0.094
10	221	0.004	0.094
10	226	0.004	0.093
10	231	0.004	0.092
10	236	0.003	0.092
10	241	0.003	0.091
10	246	0.003	0.090
10	251	0.003	0.090
10	256	0.003	0.089
10	261	0.003	0.088
10	266	0.003	0.087
10	271	0.003	0.087
10	276	0.003	0.086
10	281	0.003	0.085
10	286	0.003	0.085
10	291	0.003	0.084
10	296	0.003	0.083
10	301	0.003	0.083
100	5	0.007	0.182
100	10	0.007	0.179
100	15	0.007	0.185
100	20	0.007	0.194
100	25	0.008	0.203
100	30	0.008	0.213
100	35	0.008	0.222
100	40	0.009	0.231
100	45	0.009	0.240
100	50	0.009	0.248
100	55	0.010	0.256
100	60	0.010	0.264
100	65	0.010	0.272
100	70	0.011	0.280
100	75	0.011	0.288
100	80	0.011	0.295

100	85	0.011	0.303
100	90	0.012	0.310
100	95	0.012	0.317
100	100	0.012	0.323
100	105	0.013	0.330
100	110	0.013	0.336
100	115	0.013	0.342
100	120	0.013	0.348
100	125	0.013	0.354
100	130	0.014	0.359
100	135	0.014	0.364
100	140	0.014	0.370
100	145	0.014	0.375
100	150	0.014	0.379
100	155	0.015	0.384
100	160	0.015	0.389
100	165	0.015	0.393
100	170	0.015	0.398
100	176	0.015	0.402
100	181	0.015	0.405
100	186	0.016	0.409
100	191	0.016	0.413
100	196	0.016	0.416
100	201	0.016	0.419
100	206	0.016	0.422
100	211	0.016	0.425
100	216	0.016	0.428
100	221	0.016	0.430
100	226	0.017	0.436
100	231	0.017	0.435
100	236	0.017	0.437
100	241	0.017	0.439
100	246	0.017	0.441
100	251	0.017	0.443
100	256	0.017	0.445
100	261	0.017	0.446
100	266	0.017	0.449
100	271	0.017	0.450
100	276	0.017	0.452
100	281	0.017	0.453
100	286	0.017	0.455

100	291	0.017	0.456
100	296	0.017	0.458
100	301	0.017	0.459
100	5	0.021	0.559
100	10	0.021	0.541
100	15	0.020	0.535
100	20	0.020	0.531
100	25	0.020	0.531
100	30	0.020	0.527
100	35	0.020	0.525
100	40	0.020	0.523
100	45	0.020	0.522
100	50	0.020	0.520
100	55	0.020	0.519
100	60	0.020	0.518
100	65	0.020	0.516
100	70	0.020	0.515
100	75	0.020	0.514
100	80	0.019	0.513
100	85	0.019	0.512
100	90	0.019	0.510
100	95	0.019	0.509
100	100	0.019	0.508
100	105	0.019	0.507
100	110	0.019	0.505
100	115	0.019	0.504
100	120	0.019	0.503
100	125	0.019	0.501
100	130	0.019	0.500
100	135	0.019	0.499
100	140	0.019	0.498
100	145	0.019	0.496
100	150	0.019	0.498
100	155	0.019	0.494
100	160	0.019	0.493
100	165	0.019	0.492
100	170	0.019	0.491
100	175	0.019	0.490
100	181	0.019	0.489
100	186	0.019	0.488
100	191	0.019	0.487

100	196	0.018	0.486
100	201	0.018	0.485
100	206	0.018	0.484
100	211	0.018	0.483
100	216	0.018	0.482
100	221	0.018	0.481
100	226	0.018	0.480
100	231	0.018	0.479
100	236	0.018	0.478
100	241	0.018	0.477
100	246	0.018	0.475
100	251	0.018	0.474
100	256	0.018	0.473
100	261	0.018	0.472
100	266	0.018	0.471
100	271	0.018	0.469
100	276	0.018	0.468
100	281	0.018	0.467
100	286	0.018	0.465
100	291	0.018	0.464
100	296	0.018	0.463
100	301	0.018	0.462
1000	5	0.067	1.767
1000	10	0.062	1.639
1000	15	0.061	1.597
1000	20	0.060	1.577
1000	25	0.059	1.566
1000	30	0.059	1.558
1000	35	0.059	1.553
1000	40	0.059	1.550
1000	45	0.059	1.548
1000	50	0.059	1.545
1000	55	0.059	1.544
1000	60	0.059	1.543
1000	65	0.059	1.542
1000	70	0.059	1.542
1000	75	0.059	1.541
1000	80	0.059	1.542
1000	85	0.059	1.541
1000	90	0.059	1.541
1000	95	0.059	1.541

1000	100	0.059	1.541
1000	105	0.059	1.541
1000	110	0.059	1.540
1000	115	0.058	1.539
1000	120	0.058	1.538
1000	125	0.058	1.537
1000	130	0.058	1.537
1000	135	0.058	1.536
1000	140	0.059	1.545
1000	145	0.058	1.533
1000	150	0.058	1.532
1000	155	0.058	1.531
1000	160	0.058	1.529
1000	165	0.058	1.528
1000	170	0.058	1.528
1000	176	0.058	1.527
1000	181	0.058	1.527
1000	186	0.058	1.526
1000	191	0.058	1.525
1000	196	0.058	1.525
1000	201	0.058	1.524
1000	206	0.058	1.523
1000	211	0.058	1.522
1000	216	0.058	1.521
1000	221	0.058	1.519
1000	226	0.058	1.518
1000	231	0.058	1.517
1000	236	0.058	1.515
1000	241	0.058	1.514
1000	246	0.057	1.512
1000	251	0.057	1.510
1000	256	0.057	1.509
1000	261	0.057	1.507
1000	266	0.057	1.505
1000	271	0.057	1.503
1000	276	0.057	1.500
1000	281	0.057	1.498
1000	286	0.057	1.495
1000	291	0.057	1.493
1000	296	0.057	1.490
1000	301	0.057	1.487

1000	5	0.070	1.840
1000	10	0.065	1.704
1000	15	0.063	1.656
1000	20	0.062	1.630
1000	25	0.061	1.614
1000	30	0.061	1.603
1000	35	0.061	1.595
1000	40	0.060	1.589
1000	45	0.060	1.584
1000	50	0.060	1.579
1000	55	0.060	1.575
1000	60	0.060	1.573
1000	65	0.060	1.570
1000	70	0.060	1.567
1000	75	0.059	1.565
1000	80	0.059	1.563
1000	85	0.059	1.561
1000	90	0.059	1.560
1000	95	0.059	1.558
1000	100	0.059	1.556
1000	105	0.059	1.555
1000	110	0.059	1.553
1000	115	0.059	1.552
1000	120	0.059	1.550
1000	125	0.059	1.548
1000	130	0.059	1.546
1000	135	0.059	1.544
1000	140	0.059	1.542
1000	145	0.059	1.541
1000	150	0.058	1.539
1000	155	0.058	1.537
1000	160	0.058	1.536
1000	165	0.058	1.535
1000	170	0.058	1.534
1000	176	0.058	1.533
1000	181	0.058	1.532
1000	186	0.058	1.531
1000	191	0.058	1.530
1000	196	0.058	1.528
1000	201	0.058	1.527
1000	206	0.058	1.526

1000	211	0.058	1.524
1000	216	0.058	1.523
1000	221	0.058	1.521
1000	226	0.058	1.520
1000	231	0.058	1.518
1000	236	0.058	1.517
1000	241	0.058	1.515
1000	246	0.057	1.513
1000	251	0.057	1.511
1000	256	0.057	1.509
1000	261	0.057	1.507
1000	266	0.057	1.505
1000	271	0.057	1.503
1000	276	0.057	1.500
1000	281	0.057	1.493
1000	286	0.057	1.495
1000	291	0.057	1.492
1000	296	0.057	1.490
1000	301	0.056	1.486

Table 15: M(H) Data for LNTs.

Field (Oe)	Temperature (K)	Long Moment (emu)	emu/g
10	5	0.001	0.009
10	10	0.002	0.016
10	15	0.002	0.021
10	20	0.003	0.025
10	25	0.003	0.028
10	30	0.003	0.030
10	35	0.003	0.031
10	40	0.003	0.032
10	45	0.003	0.032
10	50	0.003	0.032
10	55	0.003	0.032
10	60	0.003	0.031
10	65	0.003	0.031
10	70	0.003	0.031
10	75	0.003	0.030
10	80	0.003	0.030

10	85	0.003	0.030
10	90	0.003	0.029
10	95	0.003	0.029
10	100	0.003	0.028
10	105	0.003	0.028
10	110	0.003	0.027
10	115	0.003	0.027
10	120	0.003	0.026
10	125	0.003	0.026
10	130	0.003	0.026
10	135	0.003	0.025
10	140	0.003	0.025
10	145	0.003	0.024
10	150	0.002	0.024
10	155	0.002	0.023
10	160	0.002	0.023
10	165	0.002	0.023
10	170	0.002	0.022
10	176	0.002	0.022
10	181	0.002	0.022
10	186	0.002	0.021
10	191	0.002	0.021
10	196	0.002	0.021
10	201	0.002	0.020
10	206	0.002	0.020
10	211	0.002	0.020
10	216	0.002	0.020
10	221	0.002	0.019
10	226	0.002	0.019
10	231	0.002	0.019
10	236	0.002	0.019
10	241	0.002	0.018
10	246	0.002	0.018
10	251	0.002	0.018
10	256	0.002	0.018
10	260	0.002	0.017
10	266	0.002	0.017
10	271	0.002	0.017
10	275	0.002	0.017
10	281	0.002	0.017
10	286	0.002	0.016

10	291	0.002	0.016
10	296	0.002	0.016
10	301	0.002	0.016
10	5	0.010	0.093
10	10	0.009	0.090
10	15	0.009	0.087
10	20	0.009	0.083
10	25	0.008	0.079
10	30	0.008	0.075
10	35	0.007	0.072
10	40	0.007	0.069
10	45	0.007	0.066
10	50	0.007	0.063
10	55	0.006	0.060
10	60	0.006	0.058
10	65	0.006	0.055
10	70	0.006	0.053
10	75	0.005	0.051
10	80	0.005	0.050
10	85	0.005	0.048
10	90	0.005	0.046
10	95	0.005	0.045
10	100	0.005	0.043
10	105	0.004	0.042
10	110	0.004	0.041
10	115	0.004	0.039
10	120	0.004	0.038
10	125	0.004	0.037
10	130	0.004	0.036
10	135	0.004	0.035
10	140	0.004	0.034
10	145	0.003	0.033
10	150	0.003	0.032
10	155	0.003	0.032
10	160	0.003	0.031
10	165	0.003	0.030
10	170	0.003	0.029
10	176	0.003	0.029
10	181	0.003	0.028
10	186	0.003	0.027
10	191	0.003	0.026

10	196	0.003	0.026
10	201	0.003	0.025
10	206	0.003	0.025
10	211	0.003	0.024
10	216	0.002	0.024
10	221	0.002	0.023
10	226	0.002	0.022
10	231	0.002	0.022
10	236	0.002	0.021
10	241	0.002	0.021
10	246	0.002	0.021
10	251	0.002	0.020
10	256	0.002	0.020
10	261	0.002	0.019
10	266	0.002	0.019
10	271	0.002	0.018
10	276	0.002	0.018
10	281	0.002	0.018
10	285	0.002	0.017
10	291	0.002	0.017
10	296	0.002	0.016
10	301	0.002	0.016
100	5	0.010	0.098
100	10	0.015	0.147
100	15	0.020	0.188
100	20	0.023	0.219
100	25	0.025	0.240
100	30	0.026	0.254
100	35	0.028	0.268
100	40	0.028	0.269
100	45	0.028	0.271
100	50	0.028	0.271
100	55	0.028	0.270
100	60	0.028	0.268
100	65	0.028	0.266
100	70	0.027	0.264
100	75	0.027	0.261
100	80	0.027	0.258
100	85	0.026	0.255
100	90	0.026	0.252
100	95	0.026	0.248

100	100	0.025	0.245
100	105	0.025	0.241
100	110	0.025	0.238
100	115	0.024	0.234
100	120	0.024	0.231
100	125	0.024	0.228
100	130	0.023	0.224
100	135	0.023	0.221
100	140	0.023	0.217
100	145	0.022	0.214
100	150	0.022	0.211
100	155	0.022	0.208
100	160	0.021	0.205
100	165	0.021	0.202
100	170	0.021	0.201
100	176	0.020	0.196
100	181	0.020	0.193
100	186	0.020	0.190
100	191	0.019	0.188
100	196	0.019	0.185
100	201	0.019	0.182
100	206	0.019	0.180
100	211	0.018	0.177
100	216	0.018	0.175
100	221	0.018	0.172
100	226	0.018	0.170
100	231	0.017	0.168
100	236	0.017	0.166
100	241	0.017	0.163
100	246	0.017	0.161
100	251	0.017	0.159
100	256	0.016	0.157
100	261	0.016	0.155
100	266	0.016	0.153
100	271	0.016	0.151
100	276	0.015	0.149
100	281	0.015	0.147
100	286	0.015	0.145
100	291	0.015	0.144
100	296	0.015	0.142
100	301	0.015	0.140

100	5	0.059	0.572
100	10	0.058	0.560
100	15	0.057	0.545
100	20	0.055	0.529
100	25	0.053	0.511
100	30	0.051	0.494
100	35	0.050	0.477
100	40	0.048	0.461
100	45	0.046	0.446
100	50	0.045	0.431
100	55	0.043	0.417
100	60	0.042	0.404
100	65	0.041	0.392
100	70	0.040	0.380
100	75	0.038	0.369
100	80	0.037	0.359
100	85	0.036	0.349
100	90	0.035	0.340
100	95	0.034	0.331
100	100	0.033	0.322
100	105	0.033	0.314
100	110	0.032	0.306
100	115	0.031	0.298
100	120	0.030	0.291
100	125	0.030	0.284
100	130	0.029	0.277
100	135	0.028	0.271
100	140	0.028	0.265
100	145	0.027	0.259
100	150	0.026	0.253
100	155	0.026	0.248
100	160	0.025	0.242
100	165	0.025	0.237
100	171	0.024	0.232
100	176	0.024	0.227
100	181	0.023	0.223
100	186	0.023	0.218
100	191	0.022	0.214
100	196	0.022	0.210
100	201	0.021	0.205
100	206	0.021	0.201

100	211	0.021	0.197
100	216	0.020	0.194
100	221	0.020	0.190
100	226	0.019	0.186
100	231	0.019	0.183
100	236	0.019	0.179
100	241	0.018	0.176
100	246	0.018	0.173
100	251	0.018	0.169
100	256	0.017	0.166
100	261	0.017	0.163
100	266	0.017	0.160
100	271	0.016	0.157
100	276	0.016	0.154
100	281	0.016	0.151
100	286	0.015	0.149
100	291	0.015	0.146
100	296	0.015	0.143
100	301	0.015	0.141
1000	5	0.074	0.713
1000	10	0.084	0.809
1000	15	0.092	0.886
1000	20	0.098	0.946
1000	25	0.102	0.985
1000	30	0.105	1.010
1000	35	0.107	1.026
1000	40	0.108	1.035
1000	45	0.108	1.040
1000	50	0.108	1.041
1000	55	0.108	1.041
1000	60	0.108	1.039
1000	65	0.108	1.037
1000	70	0.107	1.033
1000	75	0.107	1.029
1000	80	0.106	1.025
1000	85	0.106	1.019
1000	90	0.105	1.014
1000	95	0.105	1.008
1000	100	0.104	1.001
1000	105	0.103	0.995
1000	110	0.103	0.988

1000	115	0.102	0.981
1000	120	0.101	0.974
1000	125	0.100	0.967
1000	130	0.100	0.960
1000	135	0.099	0.953
1000	140	0.098	0.946
1000	145	0.097	0.938
1000	150	0.097	0.931
1000	155	0.096	0.924
1000	160	0.095	0.916
1000	165	0.094	0.909
1000	170	0.094	0.902
1000	175	0.093	0.894
1000	181	0.092	0.887
1000	186	0.091	0.880
1000	191	0.091	0.873
1000	196	0.090	0.866
1000	201	0.089	0.858
1000	206	0.088	0.851
1000	211	0.088	0.844
1000	216	0.087	0.837
1000	221	0.086	0.830
1000	226	0.085	0.823
1000	231	0.085	0.816
1000	236	0.084	0.809
1000	241	0.083	0.802
1000	246	0.083	0.794
1000	251	0.082	0.787
1000	256	0.081	0.780
1000	261	0.080	0.772
1000	266	0.079	0.765
1000	271	0.079	0.758
1000	276	0.078	0.751
1000	281	0.077	0.743
1000	286	0.076	0.736
1000	291	0.076	0.729
1000	296	0.075	0.722
1000	301	0.074	0.714
1000	5	0.133	1.283
1000	10	0.133	1.277
1000	15	0.132	1.268

1000	20	0.131	1.259
1000	25	0.130	1.248
1000	30	0.128	1.236
1000	35	0.127	1.224
1000	40	0.126	1.213
1000	45	0.125	1.201
1000	50	0.124	1.189
1000	55	0.122	1.177
1000	60	0.121	1.165
1000	65	0.120	1.154
1000	70	0.119	1.143
1000	75	0.118	1.135
1000	80	0.116	1.120
1000	85	0.115	1.109
1000	90	0.114	1.098
1000	95	0.113	1.087
1000	100	0.112	1.076
1000	105	0.111	1.066
1000	110	0.110	1.055
1000	115	0.109	1.045
1000	120	0.107	1.035
1000	125	0.106	1.024
1000	130	0.105	1.014
1000	135	0.104	1.004
1000	140	0.103	0.994
1000	145	0.102	0.985
1000	150	0.101	0.975
1000	155	0.100	0.965
1000	160	0.099	0.956
1000	165	0.098	0.947
1000	171	0.097	0.937
1000	176	0.096	0.928
1000	181	0.095	0.919
1000	186	0.095	0.910
1000	191	0.094	0.901
1000	196	0.093	0.892
1000	201	0.092	0.883
1000	206	0.091	0.875
1000	211	0.090	0.866
1000	216	0.089	0.857
1000	221	0.088	0.849

1000	226	0.087	0.840
1000	231	0.086	0.832
1000	236	0.085	0.823
1000	241	0.085	0.814
1000	246	0.084	0.806
1000	251	0.083	0.798
1000	256	0.082	0.789
1000	261	0.081	0.781
1000	266	0.080	0.772
1000	271	0.079	0.764
1000	276	0.079	0.756
1000	281	0.078	0.747
1000	286	0.077	0.739
1000	291	0.076	0.731
1000	296	0.075	0.723
1000	301	0.074	0.715

APPENDIX IV: HYDROXYLATION OF GADONANOTUBES

"A thing long expected takes the form of the unexpected when at last it comes" ~ Mark Twain

INTRODUCTION

This appendix explores the effects of adding hydroxyl functional groups to the exterior sidewalls of the GNTs, as shown in **Figure 49**, and serves as an investigative study of relaxivity manipulation of the GNTs. This project originally began as an attempt to increase the water solubility of the GNTs while simultaneously increasing relaxivity (**Chapter 2**), as previously recorded for gadofullerenols.[220] While significant water-solubilization was never achieved, GNT relaxivity was greatly enhanced (ca. 25% increase). It should be noted that this project was abandoned upon realization that water-solubility was not significant enhanced following hydroxylation.

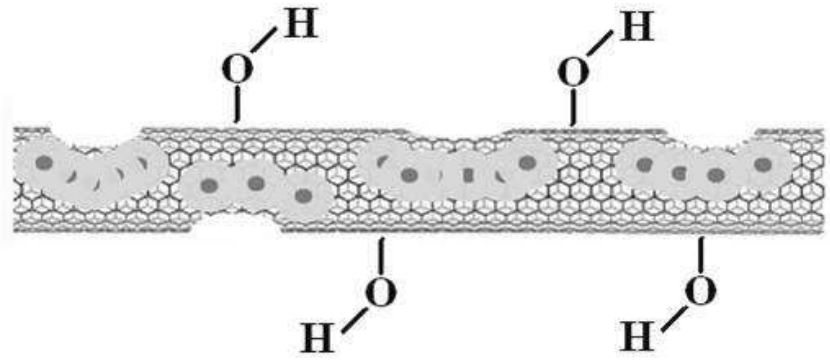

Figure 49. Pictorial representation of a hydroxylated Gadonanotube.

HYDROXYLATION

Hydroxyl Radical

It is important to start by acknowledging the misnomer of "hydroxylation." This term is traditionally reserved for the oxidative process converting a C-H bond to a C-OH bond; however, as the goal was to coat the carbon exterior of the US-tube nanocapsules with hydroxyl functional groups, the term seems both appropriate and descriptive.

As shown in **Table 16**, hydroxyl radical, or the neutral form of the hydroxide ion denoted •OH, is highly reactive. As such, the radical is very short lived and must be produced in the laboratory setting. Two common techniques for creation of the hydroxyl radical are the employment of Fenton chemistry and the photodissociation of H_2O_2 with UV-light.[221,222] Occasionally, the two will be coupled in what is known as a photoassisted Fenton reaction or Photo-Fenton reaction.[223]

Table 16. Oxidation potentials of some common chemical oxidants.[224]

Reactive Species	Oxidation Potential (V)
Fluorine	3.03
Hyroxyl radical	2.80
Singlet oxygen	2.42
Ferryl ion (FeO^{2+})	~2.0 [225]
H_2O_2	1.78
Permanganate	1.68
Chlorine dioxide	1.15
Cl_2 / Br_2 / I_2	1.00 / 0.80 / 0.54

A third hydroxylation technique specific for carbonaceous nanomaterials is a solid-phase mechanochemical reaction that involves a mechanical mill and sodium hydroxide.[226]

Fenton Chemistry

Previous, unpublished experiments employing a Fenton reaction resulted in a failure to significantly increase the water-solubility of the US-tube nanocapsules to eliminate the requisite surfactants and/or emulsifiers currently used prior to *in vivo* injection. These experiments were briefly repeated for both comparison and verification.

This century-old hydroxyl radical reaction is still not completely understood, and the once assumed reaction with a hydroxyl radical intermediate is currently being examined against a ferryl ion intermediate (see **Table 17**),[227] despite the hydroxyl radical having a higher oxidation potential than the ferryl ion (**Table 16**).[225]. Regardless of the intermediate step, the reaction is an established and efficient hydroxylating reaction.

Table 17. Two proposed key intermediates in Fenton reaction. [227]

Key Intermediate	**Hydroxyl radical (•OH)**	**Ferryl ion (FeO^{2+})**
Initiation Step	$H_2O_2 + Fe^{2+} \rightarrow Fe^{3+} + OH^- + \bullet OH$	$H_2O_2 + Fe^{2+} \rightarrow FeO^{2+} + H_2O$
Propagation Step(s)	$\bullet OH + H_2O_2 \rightarrow H_2O + \bullet OOH$ $\bullet OOH + Fe^{3+} \rightarrow O_2 + Fe^{2+} + H^+$	$FeO^{2+} + H_2O_2 \rightarrow Fe^{2+} + H_2O + O_2$
Termination Step	$\bullet OH + Fe^{2+} \rightarrow Fe^{3+} + OH^-$	$FeO^{2+} + Fe^{2+} + 2H^+ \rightarrow 2Fe^{3+} + H_2O$
Substrate Oxidation	$\bullet OH + RH \rightarrow R\bullet + H_2O \rightarrow$ **hydroxylated product**	$FeO^{2+} + RH \rightarrow$ **hydroxylated product**

pH is important for the reaction rate of Fenton's reagent. As shown in **Table 18**, the pH values of DI water and H_2O_2 at various strengths remain ca. 4.5 – 5.0 in pH strength. The optimum pH range, however, for the Fenton reaction is less than 3.0 or more than 6.0 (**Figure 50**).[228] Additionally, the reaction will not occur at pH values higher than 10.[229] As hydrogen peroxide is more stable at lower pHs, many producers add mineral acids (e.g., phosphoric or nitric acids) to further lower the pH. It is also important to obtain reagent grade hydrogen peroxide that won't contain acidic phosphonic acid, a common commercial stabilizer that will prevent the desired hydrogen peroxide degradation. Finally, it should be noted that the mixture of Fe^{2+} ions and H_2O_2 is known as Fenton's reagent.

Table 18. Hydrogen peroxide pH at various concentrations in water.[230]

% H_2O_2	0	10	20	30	40	50	60	70	80	90	100
pH @ 25 ^oC	7.0	5.3	4.9	4.7	4.6	4.5	4.5	4.5	4.6	4.9	6.2

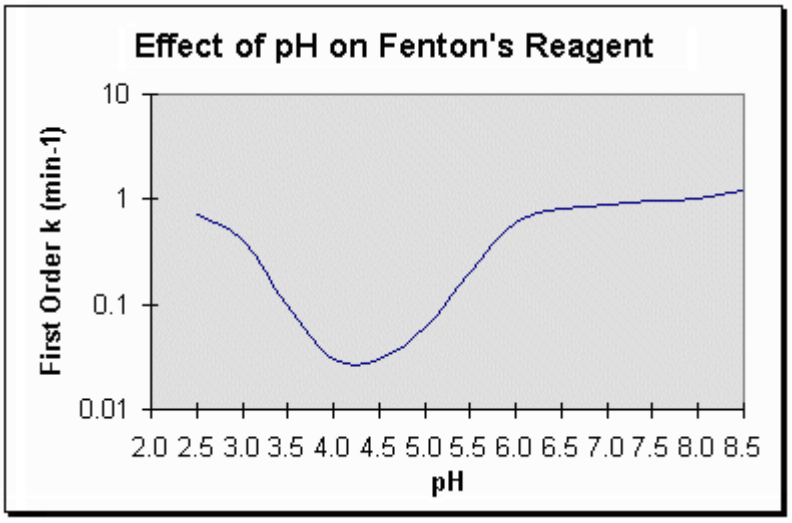

Figure 50. Effect of pH on Fenton's Reagent.[228]

Fenton's reagent has been used to previously functionalize MWNTs.[229] The MWNTs were functionalized with -OH, -COOH, and quinone groups, and the investigators proposed that the •OH attacked the MWNTs through electrophilic addition on defect sites and/or unsaturated C=C bonds. These authors did not report any increase in water solubility for the product.

UV Photolysis

Photolysis, also known as photodissociation or photodecomposition, of H_2O_2 is another common method employed for hydroxyl radical formation. The mechanism is simply:

$$H_2O_2 \xrightarrow{h\nu} 2 \cdot OH$$

For this reaction, the optimal wavelength for the UV light source is 206–270 nm,[227] with a high molar absorption coefficient of the peroxide anion at 253.7 nm ($\varepsilon_{253.7\ nm} = 18.6\ M^{-1}\ cm^{-1}$).[224] This high molar absorptivity is important as lower wattage light sources can be used, ultimately reducing the amount of heat added to the system. Heat produces the degradation of H_2O_2 according to:

$$2\ H_2O_2 \rightarrow 2\ H_2O + O_2$$

by a 2.2 factor increase for every 10 ^oC increase.[230] This degradation of hydrogen peroxide into oxygen and water is also seen at higher pH levels, however this is mitigated by the fact that more alkaline conditions also increase the photodecomposition efficiency.[224]

Mechanochemical Hydroxylation Reactions

The simplest form of mechanochemistry is the use of a mortar and pestle, yet the first reported mechanochemical hydroxylation reaction on carbonaceous nanomaterials employed the use of a high-speed vibration mill (HSVM), specifically a commercially-available Wig-L-Bug.[231] In short, a mixture of 45 mg of C_{60} and 900 mg of KOH in a stainless steel mill with milling ball was shaken for 1 h in the Wig-L-Bug at room temperature in air. The resulting brown homogenous solution was filtered and precipitated in methanol rendering 62 mg of $C_{60}(OH)_n$ (n=27.2), yield: 84%.

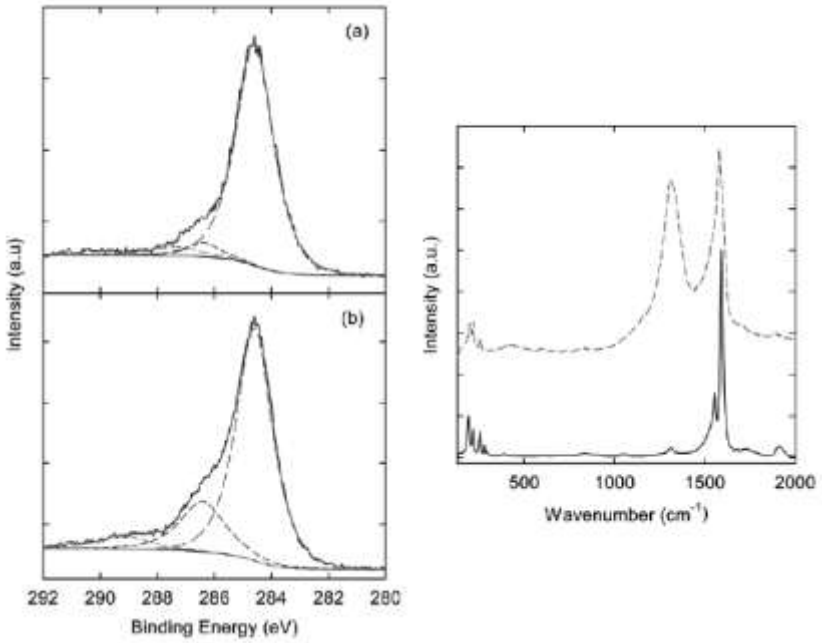

Figure 51. XPS and Raman spectra for "SWNTols" prepared through mechanochemical reaction. Left: XPS C 1s spectra of (a) the pristine SWNTs and (b) the SWNTols. (The dashed curve that peaks at 286.4 eV represents C-O) Right: Raman spectra of the pristine SWNTs (solid curve) and the SWNTols (dash curve).[232]

Later that year, the same group published similar results for forming "carbon nanotubols" or "SWNTols" (hydroxylated SWNTs) following a similar mechanochemical reaction

involving KOH and HiP_{CO} SWNTs.[232] While keeping the ratio of mass of carbon nanomaterial to KOH the same, yet doubling the reaction time to 2 hr, the workers were able to produce hydroxylated SWNTs with a solubility of 3 mg/mL in water and insoluble in organic solvents. The group verified the hydroxylation, in part, through an increase of percentage content of the C-O curve (286.4 eV) comprising the 1s electron configuration for carbon (C_{1s}) spectra from 3.4% to 14.9% (**Figure 51, left** [note increase of dashed curve peaking at 286.4 eV from a to b]); the increase of this left shoulder strongly suggests that the binding energy for the C_{1s} spectra is comprised of more alcohol groups (C-OH) than before. It should be noted that while this elemental scan renders information that the C_{1s} has more alcohol character, it is not a dependable method for quantification of alcohol groups as it depends on a user-biased peak-fitting.

The group further verified hydroxylation of the SWNTs using Raman spectroscopy. The D:G ratio on the Raman spectra decreased from 1:18 for HiP_{CO} SWNTs to 1:1.2 for SWNTols (**Figure 51, right**). This method has the advantage of being solvent free and adds approximately one -OH group per 10 carbon atoms.

MATERIALS AND METHODS

Materials

US-tube nanocapsules from electric-arc discharge SWNTs with Ni/Y catalyst (AP Grade, CarboLex, Inc., Lexington, Kentucky) were prepared as discussed in **Chapter 1**. Full-length SWNTs from the same batch were also used. Similarly, GNTs prepared from

these US-tube nanocapsules were prepared as discussed in **Chapter 2**. 30% H_2O_2 (TraceSELECT® Ultra for trace analysis, pH = 4.1, Fluka) was purchased for each round of experiments. All water was high-performance liquid chromatography (HPLC) grade (Amber glass, Fluka). Both ferrous chloride and titanium dioxide (or titania) samples were puriss. grade from Fluka (purris. grade ≥ 98.5% purity, purum ≥ 95.0% purity, technical grade ≥ 90% purity). Solutions of 0.01 mM, 0.10 mM, and 1.00 mM of both $FeCl_2$ (aq) and TiO_2 (aq) were prepared using HPLC-grade H_2O.

Fenton Chemistry

Four 10.0 mg samples of each material (US-tube nanocapsule and GNT, 8 samples in total) were dispersed in 10.0 mL of 30% H_2O_2 via 6 minutes of bath sonication. 1.0 mL of $FeCl_2$ at each concentration (0.01 mM, 0.10 mM, and 1.00 mM) was added to each sample with one sample receiving no $FeCl_2$ as a control. After 6 hours, the reaction was quenched by the addition of excess Na_3PO_4. All samples were then gravity-filtered over a coarse ('C') fritted glass filter. The filtered material was removed from the filter through pipette aspiration with DI water, collected on a watch glass, and dried overnight in a 40 ^oC oven. All samples were analyzed prior and post reaction via Raman spectroscopy (Renishaw Raman microscope, using a 633 nm laser). Additionally, the GNT sample filtrate was analyzed using inductively-coupled plasma optical emission spectrometry (ICP-OES, Perkin-Elmer Optima 3200V) for the presence of Gd. This procedure was repeated in triplicate, and then repeated in triplicate substituting titania for ferrous chloride.

Mechanochemistry

For this technique, a published method was followed.[232] In short, 10.0 mg of sample (both full-length SWNTs and US-tube nanocapsule, GNTs not tested) and 200.0 mg of KOH flakes were added to a Wig-L-Bug amalgamator (Bratt 3110-B) mill with a stainless steel milling ball. Samples were milled in air for 2 hours (8 cycles of 15 min on, 5 min off to prevent instrument overheating). Resulting mixture was dissolved in 10 mL of DI water and precipitated into 100 mL of methanol. Precipitation was repeated until the methanol solution became neutral (to ensure removal of potassium hydroxide residues). Following centrifugation, the upper layer of liquid was removed and the resulting black solid analyzed via Raman spectroscopy and TGA as described above.

UV Photolysis

Luzchem Photoreactor

In order to prevent the unwanted loading of metal ions, it was important to devise a method that would need no metal catalyst (such as a Fenton reagent) to create reactive hydroxyl radicals for US-tube nanocapsules sidewall derivitization. Initial experiments were performed in a Luzchem Photoreactor (LZC-4V). The photoreactor was comprised of fourteen UV bulbs (6 lining top, 8 on left and right, G8T5 Bulbs: 8W, 254 nm). Preliminary studies explored 10.0 mg of US-tube capsules in 10.0 mL of 30% H_2O_2 for 20 minutes in the photoreactor. The results suggested no increase in functionalization: (a) there was no measurable change prior to post-reaction via Raman spectroscopy D:G ratio, (b) there was no apparent change in solubility, and (c) a comparison of prior and post-reaction 30% H_2O_2 was titrated with potassium permanganate (0.5 M $KMnO_4$ *(aq)*)

and showed no difference according to:

$$2\ MnO^{4-} + 5\ H_2O_2 + 6\ H^+ \rightarrow 2\ Mn^{+2} + 5\ O_2 + 8\ H_2O$$

suggesting that the 30% H_2O_2 went unchanged for the duration of the experiment.

Custom Photolysis Apparatus

To better control the UV photolysis reaction conditions, an elementary photolysis apparatus (**Figure 52)** was constructed from a bass wood box, ca. 18 cm x 10 cm x 8 cm. This apparatus allowed an 8 W, 115 V, 254 nm UV light source to irradiate samples (an 8 W bulb was the minimum wattage commercially-available to minimize heat addition to the system; 254 nm was selected for the high molar absorption coefficient described in the section above). An inert gas inlet was also installed on the apparatus to permit flushing the system with argon gas. The aim of this feature was to prevent any unwanted chemistry where the mixture could interact with the native atmosphere. Also, it should be noted that common scintillation vials did *not* allow significant amounts of UV light to pass, despite being excellent with light transmission. For this reason, a container made of quartz (which did allow 254 nm UV light to pass) was utilized.

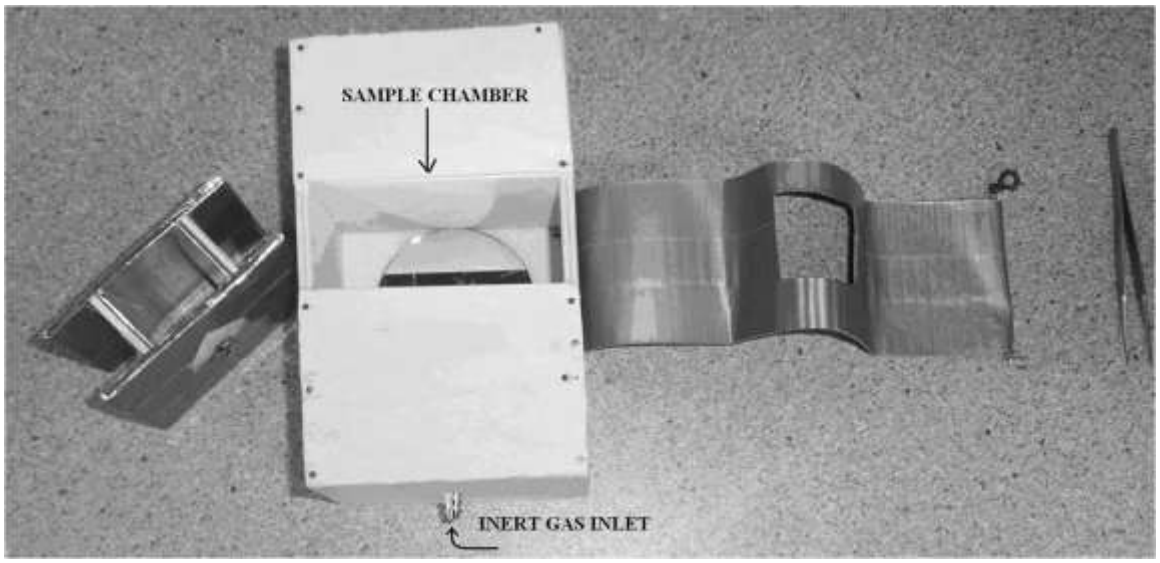

Figure 52: Photolysis Apparatus.

To ensure that the apparatus was functional, 10.0 mL of 30% H_2O_2 with 10.0 mg US-tube nanocapsules was introduced into the reaction chamber and flooded with Ar (g). The UV light source was placed atop, and photolysis was allowed to occur for 30 minutes. Following reaction, the nanocapsules were removed using a medium-grade fritted-glass filter, and 1.00 mL of the reacted H_2O_2 was titrated 0.5 M $KMnO_4$ *(aq)* to determine the concentration of H_2O_2.

This procedure was repeated lengthening the reaction time by 30 min for four time points (t = 30 min, 60 min, 90 min, and 120 min) and was compared to values of 10.0 mL of 30% H_2O_2 introduced to the reaction apparatus with a standard fluorescent 8 W bulb (to simulate the same heat addition). The entire procedure was then repeated by also bath sonicating the 30% H_2O_2 for 6 min prior to irradiation (both UV and fluorescent) to measure the effects of sonication on H_2O_2 degradation.

Reaction Conditions

A 10.0 mg of each sample (US-tube nanocapsule and GNT) were bath sonicated in 30% H_2O_2 for 6 min and irradiated for 12 hours in the photolysis apparatus. Prior to introducing the sample dispersed in H_2O_2 to the apparatus, the system was flushed with Ar (g). Additionally, Ar (g) was continuous added to the apparatus for the 12 hr duration. Once loaded, the sample chamber was covered with the duct-tape barrier and the UV light source placed atop the apparatus. Following 12 hours, all samples were filtered, dried, and analyzed as for the Fenton reactions above. As a control 10.0 mg of each sample underwent the same set-up, however a desk lamp with an 8 W incandescent light bulb (Federal Signal) replaced the UV light source to best simulate heat effects. XPS data was collected on all samples (prior and post reaction) pressed onto indium foil, using a PHI Quantera spectrometer. Raman spectra were also collected as described above. A pre- and post-treatment sample of the GNTs were lyophilized for 6 hours to dryness and shipped to Galbraith Laboratories for Karl Fisher titration analysis. This was repeated nine times for both US-tube nanocapsules and the GNTs (due to cost, only 3 samples were analyzed via Karl Fisher titration).

Relaxivity Measurements

A Bruker mq60 MiniSpec operating at 60 MHz (1.41 Tesla) and 37 °C was used to collect all relaxivity measurements, and an inversion recovery pulse sequence was used to measure the longitudinal relaxation time (T_1). Samples were prepared and analyzed for Gd^{3+}-ion content as described in **Chapter 2**. pH of samples were varied with the addition of HCl and NaOH to see pH effects on both the GNTs and the resulting Gadonanotubols.

Strange Occurrence

Very strange (yet reproducible, n=2) results occurred when using the above protocol for the photolysis reactor on full-length Arc (Carbolex) synthesized SWNTs that had been sonicated in 5.0 mM $GdCl_3$ (*aq.*) and gravity filtrated with HPLC-grade water prior to reaction in the reactor. These observations were never explored; the observations are described in detail in **Appendix V.**

RESULTS & DISCUSSION

Fenton Chemistry

The reaction was vigorous, instantly releasing O_2 (confirmed with flame test – glowing splint relit) upon addition of ferrous chloride or titania, and became increasingly more vigorous at higher concentrations. This method, however, was quickly abandoned upon analysis of the ICP-OES results showing US-tube nanocapsules retained Fe (1.6 ± 0.5 wt. %) and Ti (1.2 ± 0.5 wt. %) for ferrous chloride and titania respectively. This very undesirable side-effect ended further studies for the Fenton reaction. Furthermore, while the Raman spectra on the post-Fenton reaction GNTs did show a significant increase in D:G ratio for all samples, the increases were all less than the increase in D:G ratio results for US-tubes treated via UV photolysis. It should be noted, however, that the lowest concentrations of metal (0.01 mM) had the largest effects on increasing the D:G ratio; however, despite the lower concentration of metal in solution, the metal loading percentages were roughly the same. *No further analysis was attempted.*

Mechanochemistry

This method was attempted eleven times on three different HSVM devices, and none supported the documented 2 hour experimental run-time. All three HSVM devices acquired were designed for 60 second run-times – for this reason, the instruments encountered problems with overheating, as well as breaking the mechanical arms that support the mill (4 sets of arms, both plastic and steel, were broken attempting to allow the 2 hour milling – personal apologies to the Barron Group's instrument that sacrificed its metal arms in the name of science). A few years after this project was abandoned, curiosity drove me to test fullerenes in the apparatus, and in as little as 15 minutes, a brown solid formed that was soluble in water (indicating successful synthesis of fullerenols); this prompted further review of instrumentation, and an industrial grade amalgamator, with a 1 hour time frame (as opposed to the 1 minute time frame of the previously tested instruments) was discovered.

UV Photolysis

Apparatus

The reaction chamber showed a 3 fold increase in the rate of H_2O_2 decomposition via UV photolysis when compared to a control (fluorescent bulb) over the measured 2 hr period (as shown in **Figure 53**). Additionally, the reaction with the UV light source was bubbling; when a glowing (smoldering) wooden splint was introduced, it relit suggesting this released gas was O_2. Bath sonication of the H_2O_2 prior to reaction in the photolysis apparatus showed no measurable difference for both the UV and fluorescent light sources. These results suggest that the photolysis apparatus successfully decomposes

H_2O_2 with an 8W, 254 nm UV light source.

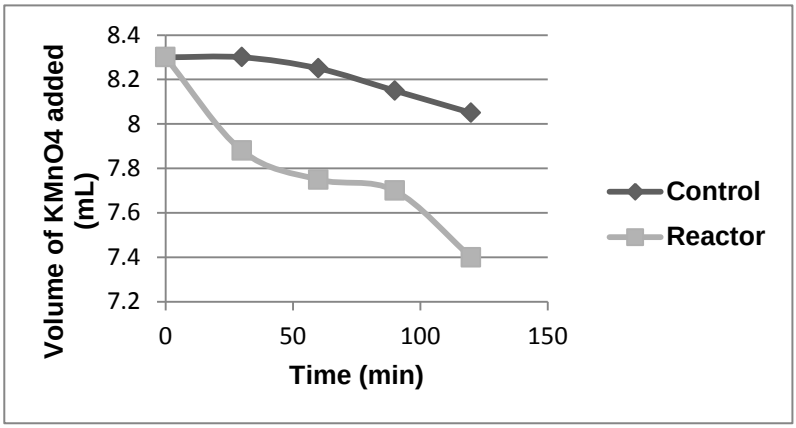

Figure 53: Effectiveness of Photolysis Apparatus (volume of 0.5 M $KMnO_4$ required to titrate treated H_2O_2 sample; dark diamonds represent 8W fluorescent bulb; gray squares represent 8W UV light source).

Raman Spectra

The Raman spectroscopy spectra were taken using a 633 nm laser attached to a Renishaw Raman microscope. Samples were in dried powder form atop a glass microscope slide. Representative spectra are displayed in **Figure 54**:

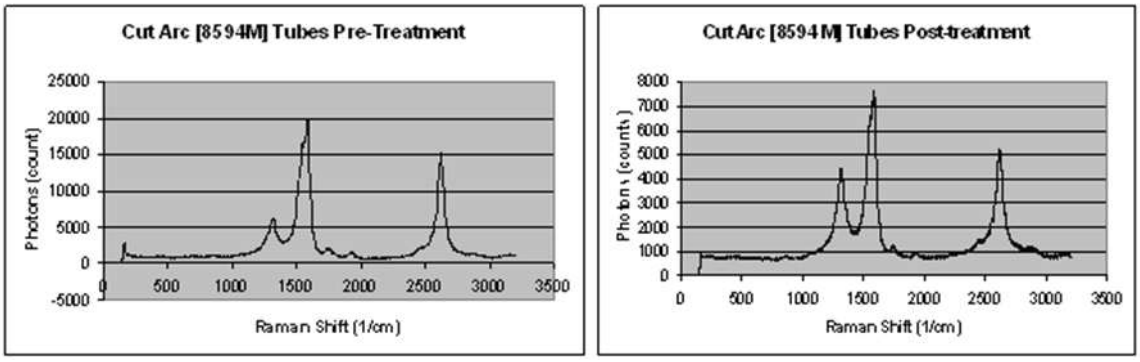

Figure 54: Raman spectra of US-tube nanocapsules pre- and post-UV treatment (633 nm laser).

Analysis of 5 different samples pre- and post treatment resulted in an average D:G ratio increase from 0.31 ± 0.02 to 0.57 ± 0.05. US-tube nanocapsules placed in H_2O_2 under the

8W fluorescence bulb showed a D:G ratio increase from 0.31 ± 0.02 to 0.34 ± 0.02. A sample calculation of the D:G ratio determination is shown in the **Table 19**. While the D:G ratio shouldn't be used for quantitative purposes, the significant D:G ratio increase strongly suggests a significant increase in the concentration and distribution of functional groups on the surface of the US-tube nanocapsules.

Table 19. D:G ratio increase of US-tube nanocapsules following UV photolysis reaction

	Pre-Treatment	Post-Treatment
Counts at Carbon sp^3 peak (D-band, ca. 1319 cm^{-1})	6211	4444
Counts at carbon sp^2 peak (G-band, ca. 1588 cm^{-1})	19791	7587
D:G ratio	0.3138	0.5857

XPS Spectra

Atomic concentrations were calculated for the XPS spectra using the following relative sensitivity factors determined for the XPS system: C_{1s} 0.314, O_{1s} 0.733. Atomic Concentration Percentage (C_{1s} and O_{1s} only) pre-treatment was 96.4 ± 0.8 % C and 3.6 ± 0.8 % O. Similarly, post-treatment was 83.0 ± 0.6 % C and 17.0 ± 0.6 % O. An example of the difference of pre- and post-treatment oxygen content can be seen in the overlay of **Figure 55**. (Please note that the survey scan of **Figure 55** was *not* used for data analysis. More focused XPS scans, such as shown in **Figure 56**, were used for data analysis).

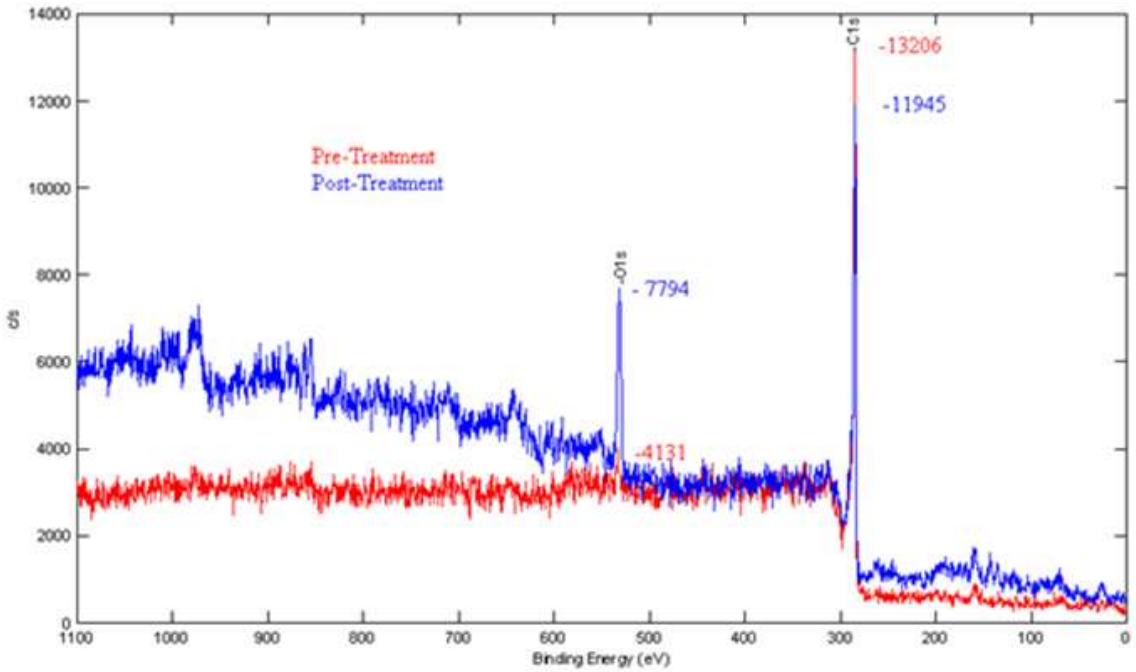

Figure 55: Overlay of XPS survey scans of US-tube nanocapsules pre- and post-treatment. Note: Not used for analysis, displayed to show increase in oxygen content.

Examination of the post-treatment nanocapsules via XPS (**Figure 56**) revealed a significant increase of a left shoulder, which strongly suggested that the binding energy for the C_{1s} spectra is comprised of more alcohol groups (C-OH) than before. Normalizing the best-fit area of the shoulder pre- and post-treatment showed an increase in the ratio of C-O-R bonding to C-C bonding of 0.072 pre-treatment to 0.230 post-treatment. This again suggested that the nanocapsules had been functionalized with –OR functional groups.

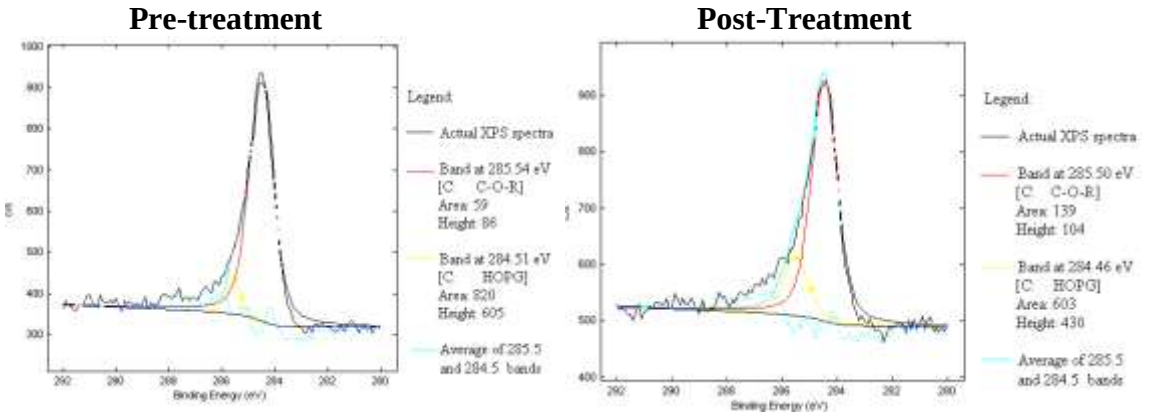

Figure 56. XPS C 1s spectra of US-tube nanocapsules pre-treatment (left) and post-treatment (right).

This XPS data coupled with Karl Fisher titration results acquired by Galbraith Laboratories to determine the water content inside oven-dried GNTs shows that there is approximately one oxygen atom for every 6-8 carbon atoms, suggesting a high degree of hydroxylation occurred.

CONCLUSIONS

The main conclusions from this chapter are simply (a) hydroxylation can be achieved through UV-photolysis of hydrogen peroxide and (b) this hydroxylation does not significantly alter the solubility of GNTs and/or US-tube nanocapsules. Again, the final relaxivity measurements came after this project was abandoned because hydroxylation did not increase water solubility (the primary motivation behind this series of experiments).

APPENDIX V: A STRANGE OCCURRENCE

Very strange results occurred when using the photolysis reactor on full-length Arc synthesized SWNTs that had been bath sonicated in 5.0 mM $GdCl_3$ (*aq.*). As strange results can often be scientifically-interesting, the results are summarized here:

Method

5.0 mg of full-length arc-ablation synthesized SWNTs (Carbolex, Batch 8594 M) were bath sonicated for 60 min in a 5.0 mM $GdCl_3$ solution prepared in HPLC-grade water. Following sonication, the resultant SWNTs were gravity-filtered over a coarse-grade fritted glass filter with 500 mL of HPLC-grade water. The filtered SWNTs were dried overnight in an 80 ^{o}C oven. 3.6 mg of the resultant SWNTs were suspended in 10.0 mL of 30% H_2O_2 in a test tube (10 min), then poured the full volume into the weighing dish base of the photolysis apparatus for a 6 hour reaction. This was repeated in duplicate with a fresh $GdCl_3$ solution and fresh H_2O_2.

Results

The blackish/grey solution turned a flesh tone (pink/purple in color). This purple solution was reduced to dryness using a rotary evaporator which produced a dry layer of grey/brownish material. Upon removing the vacuum, this layer instantly turned yellow. ICP-OES results of the SWNTs prior to reaction in the photolysis apparatus showed less than 0.2 % Gd by mass (remember, the US-tube nanocapsules load Gd^{3+} ions to

approximately 2-5 % by mass). This low Gd^{3+}-ion percentage is not surprising consider full-length SWNTs lack the sidewall defects and open ends of the US-tube nanocapsules. No further analysis was attempted.

Conclusions

The most-likely explanation is contamination. A duplicate-only study (n=2) is not reliable enough to truly draw conclusions. However, these preliminary results are included in this appendix should others decide to repeat these experiments in the future.

APPENDIX VI: PROPERTIES OF GADOLINIUM

Gadolinium lies in the section of elements on the periodic table commonly referred to as the *rare earth metals*;[233] while not incredibly rare, the element is found within the earth (metallic oxide) known as gadolinia (Gd_2O_3). Gadolinium is both malleable and ductile. Additionally, gadolinium has strong paramagnetic properties (7 unpaired *f* electrons) and the highest thermal neutron capture cross-section of any tested element. The metal will form both hydroxides and carbonates from CO_2 and H_2O absorption; chlorides are formed from heating in a solution of ammonia chloride at 300^oC. Most gadolinium metal is obtained from reduction of $GdCl_3$; this metal is silvery-white and very reactive. The trivalent state is the most common of all the lanthanides.[233]

By far, the most stable and common gadolinium complexes involve chelating ligands.[233] Under highly basic conditions, anionic catecholate complexes ($[Gd(cat)_4]^{5-}$ and $[Gd_2(cat)_6]^{6-}$ with coordination numbers 8 and 7 respectively) can be obtained as crystalline salts. Gadolinium will also form sesquichlorides ($[Gd_4^{6+}(Cl^-)_6]_n$), which are infinite chains of gadolinium atoms in octahedral,[234] as shown in **Figure 54**:

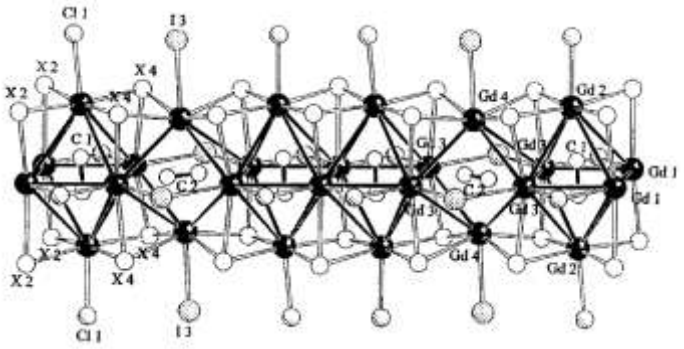

Figure 54: Gadolinium sesquichloride ($[Gd_4^{6+}(Cl^-)_6]_n$, adapted from [234]).

APPENDIX VII: PROPERTIES OF COPPER

Elemental copper is unique in that it has a single *s* electron outside a filled 3*d* shell;[233] while this may be reminiscent of alkali metals, the electrons of the *d* shell electrons are directly involved in metallic bonding. Because of the *d* shell electron's interactions, Cu compounds tend to be more covalent and have higher lattice energies than closely related alkali metals (atomic radii: Cu^{+} ion is 0.93 Å and Na^{+} ion is 0.95 Å). The majority of copper is refined via electrolysis, resulting in a tough, soft, ductile metal with a reddish color. This elemental copper is second only to silver in electrical conductivity at room temperature. Considering the relative costs of the two metals, copper wiring's prevalence becomes readily apparent. Elemental copper reacts with molecular oxygen to yield CuO and, at higher temperatures, Cu_2O, rendering the two most common oxidative states of copper: copper(I) and the more stable copper(II).

The copper(I) compounds range from mononuclear, binuclear with halide bridges, polynuclear, or even in infinite chains;[233] however, as these compounds are readily oxidized to Cu^{2+} compounds (and this thesis involves $CuCl_2$ as a precursor), the chemistry of copper(II) will be the focus of this section. Typically, comparison via electron paramagnetic resonance (EPR) [also known as electron spin resonance (ESR)], between Cu^{1+} and Cu^{2+} compounds is vividly clear, as Cu^{1+} is diamagnetic and Cu^{2+} is paramagnetic (making only the Cu^{2+} ion visible via EPR);[235] unfortunately, preliminary study in collaboration between the Wilson and Palmer Groups at Rice University, carbon nanotubes demonstrate significant signal over a wide range of magnetic field rendering

electronic-state determination difficult; the literature suggests that this large amount of field results from superparamagnetic catalyst presence in the tubes.[236,237]

Bridging Ligands and Copper

Bridged copper ions are well established, the most common being simply dihydroxo-bridged copper(II) species.[238] In 1978, the first single hydroxyl-bridged binuclear copper(II) species was discovered.[239] As more complicated organic ligand structures were discovered, such as the N3S-type ligand with phenylthioether of **Figure 58, left**,[234] dihydroxo-bridged copper (II) species began taking on novel configurations, as shown in the square planar configuration of **Figure 58, right.**

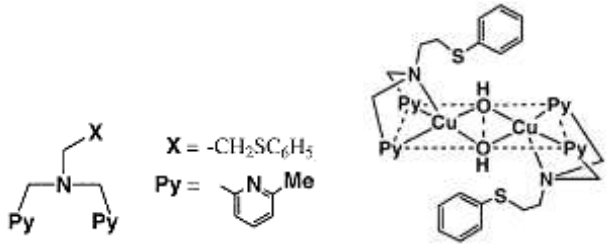

Figure 58: Dihydroxyl-bridged, binuclear copper (II) complex (right) formed from N3S-type ligand with phenylthioether (left, adapted from [234]).

Furthermore, this hydroxyl-bridging has been witnessed beyond simple binuclear species; in once case, a copper(II) ion was conjugated to a nucleoside (glycosamine precursors to the phosphorylated nucleotide building blocks of both DNA and RNA) creating infinite chains of hydroxyl-bridged copper(II).[240]

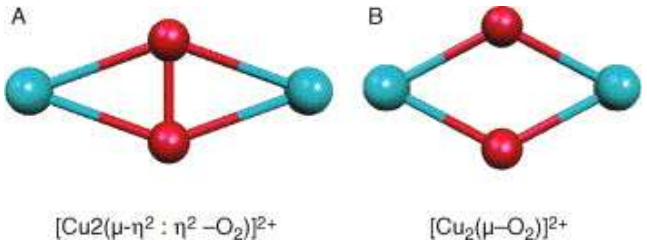

Figure 59: Two principle arrangements of peroxo-bridged copper(II) [adapted from [241]].

Finally, oxo-bridging is not limited to hydroxyl-bridging. Molecular oxygen has been demonstrated to bridge copper(I) ions, effectively oxidizing them to their copper(II) state.[241] Peroxo bridging between copper(II) has been witnessed,[242] as shown in **Figure 59**, and these species exist in equilibrium as established via kinetic, spectroscopic, and crystallographic studies.[243] Peroxido complexes, like those in **Figure 60**, have also been established, [244] being the only other stable oxo-bridged copper complexes in the literature (note: superoxo complexes are incredibly short lived).[241]

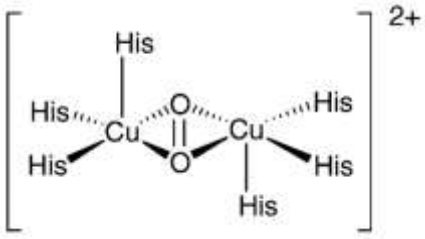

Figure 60: Dinuclear side-on peroxido-bridged copper(II) cluster (His = histidine, adapted from [244]).

Gadolinium/Copper Complexes

Gadolinium/copper complexes took over the literature with the push for high T_c superconductors and *rare earth* copper oxides. Prior to this push, most coupling of gadolinium and copper use very elaborate organic ligands developed to successfully

chelate both copper and gadolinium ions. The modified DOTA chelate in **Figure 61** is used for copper ion detection, as the gadolinium ion will form seven (7) bonds to the DOTA segment of the ligand, using its final bond to one of the terminal carboxylic acids attached to the amino group.[245] However, as soon as copper ions are present, the carboxylic acids chelate the Cu^{2+} ions, causing an open site on the Gd^{3+} ion. This free site will then bind to water from the aqueous environment, and, through spin cohesion, decrease the time it takes for surrounding water protons to relax in solution. This decrease in T_1 can then be monitored via an MRI instrument.

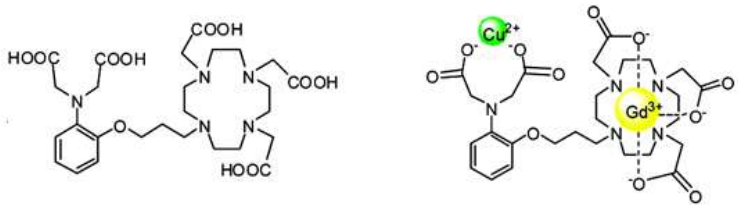

Figure 61: Organic ligand (left) based on DOTA for chelation of both Cu^{2+} and Gd^{3+} ions (right, adapted from [245]).

Copper has been shown to bind to gadolinium in non-high T_c superconductors via oxo-bridges.[245] This cation forces a distorted pentagonal bipyramid conformation on the gadolinium ion. This particular ion, $[(CuHAPen)_2Gd(H_2O)_3]^{3+}$, was originally formed to study magnetic interactions between transition metals and rare earths. The gadolinium to copper coupling was shown to be both ferromagnetic and fairly substantial. Finally, copper has been shown to bind directly with gadolinium.[246] The thermochemistry of the copper-gadolinium interface has been determined via valance-band photoemission, showing that the copper binds strongly to the gadolinium. By coating Gd sheets with Cu, the binding energy of the 3d electrons increases over 0.7 eV.

APPENDIX VIII: U.T.M.D. ^{64}Cu LOADING PROTOCOL

This appendix contains the original ^{64}Cu loading protocol established at the Department of Experimental Diagnostic Imaging in the U. T. M. D. Anderson Cancer Center on 15 July 2008.

SUBJ: STANDARD OPERATING PROCEDURE (SOP) FOR *IN VIVO* $^{64}Cu^{3+}$ LOADING WITHIN GADONANOTUBES

1. Purpose: The purpose of this memorandum is to present a SOP following Good Laboratory Practices (GLP) to the Department of Experimental Diagnostic Imaging at the U. T. M. D. Anderson Cancer Center (UTMD).

2. Scope: The scope of this memorandum will be studies aimed for preliminary investigations on $^{64}CuCl_3$ loading and retention under simulated physiological challenge within ultra-short carbon nanotubes with internalized gadolinium ions (gadonanotubes).

3. Outline of Procedures:

- 3-2. Ensure that all Personal Protective Equipment (PPE) is in place and worn as according to UTMB's safety protocols
- 3-3. Add 5 mCi $^{64}CuCl_3$ to "US-Tube Solution"
  - 3-3.1. US-tube solution will be provided by Rice University in a disposable centrifuge tube marked "US-Tube Solution"
  - 3-3.2. US-tube solution will contain ~3mg of reduced, cut, open, debundled SWNTs in 3.0 mL of 18 MΩ deionized water
- 3-4. Bath sonicate the US-Tube/$^{64}CuCl_3$solution for 20 minutes.
- 3-5. Add 1.0 mL of 15 mM $GdCl_3$ (aq)
  - 3-5.1. 15 mM $GdCl_3$ (aq) will be provided by Rice
- 3-6. Bath sonicate the US-Tube/ $^{64}CuCl_3$ / $GdCl_3$ solution for 20 minutes.
- 3-7. Filter the solution using a coarse grade fritted glass filter.
  - 3-7.1. Coarse grade filter will be provided by Rice.
  - 3-7.2. Collect each filtrate in a disposal centrifuge tube to analyze activity.
  - 3-7.3. Continue filtration until filtrate shows no activity, but no less than a minimum of 8 washings.
- 3-8. Add collected tubes to 1% F108 Pluronic solution.
  - 3-8.1. Bath sonicate for 20 minutes
- 3-9. Sample ready for injection – dosage determined by UTMD staff

APPENDIX IX: 1.5 T AND 3.0 T MRI PHANTOM RAW DATA

Table 20. 1.5 T and 3.0 T MRI phantom raw data for 3 concentrations (200 μCi/mL, 100 μCi/mL, and 50 μCi/mL) of ^{64}CGNTs compared to 1% Tween control phantom.

T_1 or T_2	200 μCi/mL	100 μCi/mL	50 μCi/mL	1 % Tween-20	TR (ms)	TE (ms)
T_1 (3T) (ms)	2362	2166	2135	2107	9000	20
	2008	2094	1928	1531		
	2717	2239	2342	2683		
	0.9791	0.9989	0.9909	0.9322		
T_2 (3T) (ms)	88	159	267	1097	9000	25
	81	149	263	988		
	94	169	271	1205		
	0.995	0.995	0.9997	0.9831		
T_1 (1.5T) (ms)	1822	1757	1726	1878	6500	10
	1793	1715	1668	1794		
	1851	1798	1784	1963		
	0.9999	0.9997	0.9995	0.999		
T_2 (1.5T) (ms)	94	171	295	1780	9000	35
	90	162	289	1670		
	98	180	302	1890		
	0.9987	0.997	0.9993	0.9943		

APPENDIX X: RAW DATA FOR ^{124}I EXPERIMENT

Table 21. Raw data for ^{124}I experiment summarized in **Chapter 4** and displayed in **Figure 44**.

Time Points	1hr	4hr	24hr
Free ^{124}I			
Mouse 1	2.52875	4.037594	1.003942
Mouse 2	3.693727	4.166462	1.397997
Mouse 3	3.289859	3.021809	1.182813
Avg.	3.170778	3.741955	1.194917
Std Dev.	0.591547	0.626984	0.197306
$^{124}I_2$@US-tube Nanocapsules			
Mouse 1	2.949897	1.526432	2.088905
Mouse 2	2.004826	2.080629	1.008427
Mouse 3	1.561098	1.835249	1.550329
Avg.	2.17194	1.814103	1.54922
Std Dev.	0.709321	0.277703	0.54024

LIST OF REFERENCES

(1) Matson, M. L.; Wilson, L. J. *Future Med. Chem.* **2010**, *2*, 491-502.

(2) Matson, M. L.; Ananta, J. S.; Wilson, L. J. In *Nanobiomaterials Handbook*; Sitharaman, B., Ed.; CRC Press: New York, 2011; Vol. 1.

(3) Picard, F. J.; Bergeron, M. G. *Drug Discov. Today* **2002**, *7*, 1092-1101.

(4) Gilham, I. *Drug Discov. World* **2002**, 17-23.

(5) Gu, Z.; Peng, H.; Hauge, R. H.; Smalley, R. E.; Margrave, J. L. *Nano Lett.* **2002**, *2*, 1009-1013.

(6) McDevitt, M. R.; Chattopadhyay, D.; Kappel, B. J.; Jaggi, J. S.; Schiffman, S. R.; Antczak, C.; Njardarson, J. T.; Brentjens, R.; Scheinberg, D. A. *J. Nucl. Med.* **2007**, *48*, 1180.

(7) Ashcroft, J. M.; Hartman, K. B.; Mackeyev, Y.; Hofmann, C.; Pheasant, S.; Alemany, L. B.; Wilson, L. J. *Nanotechnology* **2006**, *17*, 5033-5037.

(8) Hassan, A. A.; Chan, B. T. Y.; Tran, L. A.; Hartman, K. B.; Ananta, J. S.; Mackeyev, Y.; Hu, L.; Pautler, R. G.; Wilson, L. J.; Lee, A. V. *Contrast Media Mol. Imaging* **2009**, *5*, 34-38.

(9) Sitharaman, B.; Kissell, K. R.; Hartman, K. B.; Tran, L. A.; Baikalov, A.; Rusakova, I.; Sun, Y.; Khant, H. A.; Ludtke, S. J.; Chiu, W.; Laus, S.; Toth, E.; Helm, L.; Merbach, A. E.; Wilson, L. J. *Chem. Commun.* **2005**, 3915-3917.

(10) Ashcroft, J. M.; Hartman, K. B.; Kissell, K. R.; Mackeyev, Y.; Pheasant, S.; Young, S.; Van der Heide, P. A. W.; Mikos, A. G.; Wilson, L. J. *Adv. Mater.* **2007**, *19*, 573-575.

(11) Hartman, K. B.; Hamlin, D. K.; Wilbur, D. S.; Wilson, L. J. *Small* **2007**, *3*, 1496-1499.

(12) Contributors in *Wikipedia* 2011; Vol. 2011.

(13) Kroto, H. W.; Heath, J. R.; Obrien, S. C.; Curl, R. F.; Smalley, R. E. *Nature* **1985**, *318*, 162-163.

(14) Eckroth, D. *J. Chem. Educ.* **1993**, *70*, 609.

(15) Tarnai, T. *Philosophical Transactions of the Royal Society A* **1993**, *343*, 145-154.

(16) Dresselhaus, M. S.; Dresselhaus, G.; Eklund, P. C.; San Diego, EUA : Academic Press: 1996.

(17) Powell, W.; Cozzi, F.; Moss, G.; Thilgen, C.; Hwu, R. J. R.; Yerin, A. *Pure Appl. Chem.* **2002**, *74*, 629-695.

(18) Thévenet, C. Terre des Hommes, Île Sainte-Hélène, Montréal, Québec, Canada., 2001.

(19) Buseck, P. R.; Tsipursky, S. J.; Hettich, R. *Science* **1992**, *257*, 215-217.

(20) Heymann, D.; Wolbach, W. S.; Chibante, L. P. F.; Brooks, R. R.; Smalley, R. E. *Geochimica Et Cosmochimica Acta* **1994**, *58*, 3531-3534.

(21) Daly, T. K.; Buseck, P. R.; Williams, P.; Lewis, C. F. *Science* **1993**, *259*, 1599-1601.

(22) Becker, L.; Bada, J. L.; Winans, R. E.; Hunt, J. E.; Bunch, T. E.; French, B. M. *Science* **1994**, *265*, 642-645.

(23) Dietz, T. G.; Duncan, M. A.; Powers, D. E.; Smalley, R. E. *J. Chem. Phys.* **1981**, *74*, 6511-6512.

(24) Heath, J. R.; Obrien, S. C.; Zhang, Q.; Liu, Y.; Curl, R. F.; Kroto, H. W.; Tittel, F. K.; Smalley, R. E. *J. Am. Chem. Soc.* **1985**, *107*, 7779-7780.

(25) Kratschmer, W.; Lamb, L. D.; Fostiropoulos, K.; Huffman, D. R. *Nature* **1990**, *347*, 354-358.

(26) Diederich, F.; Ettl, R.; Rubin, Y.; Whetten, R. L.; Beck, R.; Alvarez, M.; Anz, S.; Sensharma, D.; Wudl, F.; Khemani, K. C.; Koch, A. *Science* **1991**, *252*, 548-551.

(27) Koch, A. S.; Khemani, K. C.; Wudl, F. *J. Org. Chem.* **1991**, *56*, 4543-4545.

(28) Parker, D. H.; Wurz, P.; Chatterjee, K.; Lykke, K. R.; Hunt, J. E.; Pellin, M. J.; Hemminger, J. C.; Gruen, D. M.; Stock, L. M. *J. Am. Chem. Soc.* **1991**, *113*, 7499-7503.

(29) Chibante, L. P. F.; Thess, A.; Alford, J. M.; Diener, M. D.; Smalley, R. E. *Journal of Physical Chemistry* **1993**, *97*, 8696-8700.

(30) Taylor, R.; Langley, G. J.; Kroto, H. W.; Walton, D. R. M. *Nature* **1993**, *366*, 728-731.

(31) Peters, G.; Jansen, M. *Angew. Chem.* **1992**, *31*, 223-224.

(32) Yeretzian, C.; Hansen, K.; Diederich, F.; Whetten, R. L. *Nature* **1992**, *359*, 44-47.

(33) Alford, J. M.; Bernal, C.; Cates, M.; Diener, M. D. *Carbon* **2008**, *46*, 1623-1625.

(34) Murr, L. E.; Garza, K. M. *Atmospheric Environment* **2009**, *43*, 2683-2692.

(35) Iijima, S. *Nature* **1991**, *354*, 56-58.

(36) Iijima, S.; Ichihashi, T. *Nature* **1993**, *363*, 603-605.

(37) Ebbesen, T. W.; Ajayan, P. M. *Nature* **1992**, *358*, 220-222.

(38) Ajayan, P. M. *Chem. Rev.* **1999**, *99*, 1787-1800.

(39) Saito, S. *Science* **1997**, *278*, 77-78.

(40) Dai, H. *Acc. Chem. Res.* **2002**, *35*, 1035-1044.

(41) Wong, S. S.; Joselevich, E.; Woolley, A. T.; Cheung, C. L.; Lieber, C. M. *Nature* **1998**, *394*, 52-55.

(42) de Heer, W. A.; Châtelain, A.; Ugarte, D. *Science* **1995**, *270*, 1179-1180.

(43) Guo, T.; Nikolaev, P.; Thess, A.; Colbert, D. T.; Smalley, R. E. *Chem. Phys. Lett.* **1995**, *243*, 49-54.

(44) Kong, J.; Cassell, A. M.; Dai, H. *Chem. Phys. Lett.* **1998**, *292*, 567-574.

(45) Thess, A.; Lee, R.; Nikolaev, P.; Dai, H.; Petit, P.; Robert, J.; Xu, C.; Lee, Y. H.; Kim, S. G.; Rinzler, A. G.; Colbert, D. T.; Scuseria, G. E.; Tomanek, D.; Fischer, J. E.; Smalley, R. E. *Science* **1996**, *273*, 483-487.

(46) Kebes; English Wikipedia: 2005.

(47) Bethune, D. S.; Klang, C. H.; de Vries, M. S.; Gorman, G.; Savoy, R.; Vazquez, J.; Beyers, R. *Nature* **1993**, *363*, 605-607.

(48) Journet, C.; Maser, W. K.; Bernier, P.; Loiseau, A.; delaChapelle, M. L.; Lefrant, S.; Deniard, P.; Lee, R.; Fischer, J. E. *Nature* **1997**, *388*, 756-758.

(49) Dai, H.; Rinzler, A. G.; Nikolaev, P.; Thess, A.; Colbert, D. T.; Smalley, R. E. *Chem. Phys. Lett.* **1996**, *260*, 471-475.

(50) Peigney, A.; Laurent, C.; Dobigeon, F.; Rousset, A. *J. Mater. Res.* **1997**, *12*, 613-615.

(51) Tibbetts, G. G.; Bernardo, C. A.; Gorkiewicz, D. W.; Alig, R. L. *Carbon* **1994**, *32*, 569-576.

(52) Cheng, H. M.; Li, F.; Su, G.; Pan, H. Y.; He, L. L.; Sun, X.; Dresselhaus, M. S. *Appl. Phys. Lett.* **1998**, *72*, 3282

(53) Cheng, H. M.; Li, F.; Sun, X.; Brown, S. D. M.; Pimenta, M. A.; Marucci, A.; Dresselhaus, G.; Dresselhaus, M. S. *Chem. Phys. Lett.* **1998**, *289*, 602-610.

(54) Resasco, D. E.; Alvarez, W. E.; Pompeo, F.; Balzano, L.; Herrera, J. E.; Kitiyanan, B.; Borgna, A. *Journal of Nanoparticle Research* **2002**, *4*, 131-136.

(55) Nikolaev, P.; Bronikowski, M. J.; Bradley, R. K.; Rohmund, F.; Colbert, D. T.; Smith, K. A.; Smalley, R. E. *Chem. Phys. Lett.* **1999**, *313*, 91-97.

(56) Bronikowski, M. J.; Willis, P. A.; Colbert, D. T.; Smith, K. A.; Smalley, R. E. *J. Vac. Sci. Technol., A* **2001**, *19*, 1800-1805.

(57) Park, T.-J.; Banerjee, S.; Hemraj-Benny, T.; Wong, S. S. *J. Mater. Chem.* **2006**, *16*.

(58) Tohji, K.; Goto, T.; Takahashi, H.; Shinoda, Y.; Shimizu, N.; Jeyadevan, B.; Matsuoka, I.; Saito, Y.; Kasuya, A.; Ohsuna, T.; Hiraga, K.; Nishina, Y. *Nature* **1996**, *383*, 679-679.

(59) Bandow, S.; Rao, A. M.; Williams, K. A.; Thess, A.; Smalley, R. E.; Eklund, P. C. *J. Phys. Chem. B* **1997**, *101*, 8839-8842.

(60) Niyogi, S.; Hu, H.; Hamon, M. A.; Bhowmik, P.; Zhao, B.; Rozenzhak, S. M.; Chen, J.; Itkis, M. E.; Meier, M. S.; Haddon, R. C. *J. Am. Chem. Soc.* **2001**, *123*, 733-734.

(61) Chattopadhyay, D.; Lastella, S.; Kim, S.; Papadimitrakopoulos, F. *J. Am. Chem. Soc.* **2002**, *124*, 728-729.

(62) Zhao, B.; Hu, H.; Niyogi, S.; Itkis, M. E.; Hamon, M. A.; Bhowmik, P.; Meier, M. S.; Haddon, R. C. *J. Am. Chem. Soc.* **2001**, *123*, 11673-11677.

(63) Farkas, E.; Elizabeth Anderson, M.; Chen, Z.; Rinzler, A. G. *Chem. Phys. Lett.* **2002**, *363*, 111-116.

(64) Thien-Nga, L.; Hernadi, K.; Ljubovic, E.; Garaj, S.; Forro, L. *Nano Lett.* **2002**, *2*, 1349-1352.

(65) Mizoguti, E.; Nihey, F.; Yudasaka, M.; Iijima, S.; Ichihashi, T.; Nakamura, K. *Chem. Phys. Lett.* **2000**, *321*, 297-301.

(66) Zhang, M.; Yudasaka, M.; Nihey, F.; Iijima, S. *Chem. Phys. Lett.* **2000**, *328*, 350-354.

(67) Zimmerman, J. L.; Bradley, R. K.; Huffman, C. B.; Hauge, R. H.; Margrave, J. L. *Chem. Mater.* **2000**, *12*, 1361-1366.

(68) Sen, R.; Rickard, S. M.; Itkis, M. E.; Haddon, R. C. *Chem. Mater.* **2003**, *15*, 4273-4279.

(69) Nagasawa, S.; Yudasaka, M.; Hirahara, K.; Ichihashi, T.; Iijima, S. *Chem. Phys. Lett.* **2000**, *328*, 374-380.

(70) Rinzler, A. G.; Liu, J.; Dai, H.; Nikolaev, P.; Huffman, C. B.; Rodriguez-Macias,

F. J.; Boul, P. J.; Lu, A. H.; Heymann, D.; Colbert, D. T.; Lee, R. S.; Fischer, J. E.; Rao, A. M.; Eklund, P. C.; Smalley, R. E. *Applied Physics a-Materials Science & Processing* **1998**, *67*, 29-37.

(71) Liu, J.; Rinzler, A. G.; Dai, H.; Hafner, J. H.; Bradley, R. K.; Boul, P. J.; Lu, A.; Iverson, T.; Shelimov, K.; Huffman, C. B.; Rodriguez-Macias, F.; Shon, Y.-S.; Lee, T. R.; Colbert, D. T.; Smalley, R. E. *Science* **1998**, *280*, 1253-1256.

(72) Chiang, I. W.; Brinson, B. E.; Huang, A. Y.; Willis, P. A.; Bronikowski, M. J.; Margrave, J. L.; Smalley, R. E.; Hauge, R. H. *J. Phys. Chem. B* **2001**, *105*, 8297-8301.

(73) Donaldson, K.; Aitken, R.; Tran, L.; Stone, V.; Duffin, R.; Forrest, G.; Alexander, A. *Toxicol. Sci.* **2006**, *92*, 5-22.

(74) Kolosnjaj-Tabi, J.; Hartman, K. B.; Boudjemaa, S.; Ananta, J. S.; Morgant, G.; Szwarc, H.; Wilson, L. J.; Moussa, F. *ACS Nano* **2010**, *4*, 1481-1492.

(75) Mackeyev, Y.; Bachilo, S.; Hartman, K. B.; Wilson, L. J. *Carbon* **2007**, *45*, 1013-1017.

(76) Dresselhaus, M. S.; Jorio, A.; Hofmann, M.; Dresselhaus, G.; Saito, R. *Nano Lett.* **2010**, *10*, 751-758.

(77) Rao, A. M.; Bandow, S.; Richter, E.; Eklund, P. C. *Thin Solid Films* **1998**, *331*, 141-147.

(78) Dresselhaus, M. S.; Dresselhaus, G.; Jorio, A. *Annu. Rev. Mater. Res.* **2004**, *34*, 247-278.

(79) Bachilo, S. M.; Strano, M. S.; Kittrell, C.; Hauge, R. H.; Smalley, R. E.; Weisman, R. B. *Science* **2002**, *298*, 2361-2366.

(80) O'Connell, M. J.; Bachilo, S. M.; Huffman, C. B.; Moore, V. C.; Strano, M. S.; Haroz, E. H.; Rialon, K. L.; Boul, P. J.; Noon, W. H.; Kittrell, C.; Ma, J.; Hauge, R. H.; Weisman, R. B.; Smalley, R. E. *Science* **2002**, *297*, 593-596.

(81) Ghosh, S.; Bachilo, S. M.; Weisman, R. B. *Nat. Nanotechnol.* **2010**, *5*, 443-450.

(82) Venema, L. C.; Wildoer, J. W. G.; Tuinstra, H. L. J. T.; Dekker, C.; Rinzler, A. G.; Smalley, R. E. *Appl. Phys. Lett.* **1997**, *71*, 2629-2631.

(83) Rubio, A.; Apell, S. P.; Venema, L. C.; Dekker, C. *The European Physical Journal B - Condensed Matter and Complex Systems* **2000**, *17*, 301-308.

(84) Ziegler, K. J.; et al. *Nanotechnology* **2005**, *16*, S539.

(85) Chen, J.; Hamon, M. A.; Hu, H.; Chen, Y.; Rao, A. M.; Eklund, P. C.; Haddon, R. C. *Science* **1998**, *282*, 95-98.

(86) Price, B. K.; Lomeda, J. R.; Tour, J. M. *Chem. Mater.* **2009**, *21*, 3917-3923.

(87) Mickelson, E.; Chiang, I.; Zimmerman, J.; Boul, P.; Lozano, J.; Liu, J.; Smalley, R.; Hauge, R.; Margrave, J. *J. Phys. Chem. B* **1999**, *103*, 4318-4322.

(88) Khabashesku, V. N.; Billups, W. E.; Margrave, J. L. *Acc. Chem. Res.* **2002**, *35*, 1087-1095.

(89) Dresselhaus, M. S.; Pimenta, M. A.; Eklund, P. C.; Dresselhaus, G. *Springer Ser. Mater. Sci.* **2000**, *42*, 314-364.

(90) Osuna, S. l.; Torrent-Sucarrat, M.; Solaì€, M.; Geerlings, P.; Ewels, C. P.; Lier, G. V. *J. Phys. Chem. C*, *114*, 3340-3345.

(91) Kelly, K. F.; Chiang, I. W.; Mickelson, E. T.; Hauge, R. H.; Margrave, J. L.; Wang, X.; Scuseria, G. E.; Radloff, C.; Halas, N. J. *Chem. Phys. Lett.* **1999**, *313*, 445-450.

(92) Kissell, K. R.; Hartman, K. B.; Van der Heide, P. A. W.; Wilson, L. J. *J. Phys. Chem. B* **2006**, *110*, 17425-17429.

(93) Hartman Keith, B.; Laus, S.; Bolskar Robert, D.; Muthupillai, R.; Helm, L.; Toth, E.; Merbach Andre, E.; Wilson Lon, J. *Nano Lett* **2008**, *8*, 415-9.

(94) Sheng, H. P.; Huggins, R. A. *Am J Clin Nutr* **1979**, *32*, 630-47.

(95) Merbach, A. E. *The Chemistry of Contrast Agents in Medical Magnetic Resonance Imaging*; John Wiley & Sons, LTD: Chichester, 2001; Vol. 1.

(96) Pautler, R. G. *Physiology* **2004**, *19*, 168-175.

(97) Mai, W.; Badea Cristian, T.; Wheeler Charles, T.; Hedlund Laurence, W.; Johnson, G. A. *Magn Reson Med* **2005**, *53*, 858-65.

(98) Hämisch, Y. *Medicamundi* **2003**, *47*, 18-27.

(99) Månsson S, B. In *The Chemistry of Contrast Agents in Medical Magnetic Resonance Imaging*; Merbach AE, T. É., Ed.; John Wiley & Sons: Chichester, UK, 2001, p 1-43

(100) de Bazelaire, C. M.; Duhamel, G. D.; Rofsky, N. M.; Alsop, D. C. *Radiology* **2004**, *230*, 652-9.

(101) Ribot, E.; Bouzier-Sore, A. K.; Bouchaud, V.; Miraux, S.; Delville, M. H.; Franconi, J. M.; Voisin, P. *Cancer Gene Ther.* **2007**, *14*, 724-737.

(102) Engh Johnathan, A.; Flickinger John, C.; Niranjan, A.; Amin Devin, V.; Kondziolka Douglas, S.; Lunsford, L. D. *Stereotact Funct Neurosurg* **2007**, *85*, 162-8.

(103) Ludemann, L.; Grieger, W.; Wurm, R.; Wust, P.; Zimmer, C. *Magn Reson Imaging* **2005**, *23*, 833-41.

(104) Zimmerman, C. F.; Schatz, N. J.; Glaser, J. S. *Magnetic resonance imaging of optic nerve meningiomas. Enhancement with gadolinium-DTPA*, Bascom Palmer Eye Institute, Department of Ophthalmology, University of Miami, 1990.

(105) Nagele, T.; Petersen, D.; Klose, U.; Grodd, W.; Opitz, H.; Voigt, K. *Neuroradiology* **1994**, *36*, 303-7.

(106) Lin, Y.-J.; Koretsky, A. P. *Magn. Reson. Med.* **1997**, *38*, 378-388.

(107) Bolskar, R. D.; Benedetto, A. F.; Husebo, L. O.; Price, R. E.; Jackson, E. F.; Wallace, S.; Wilson, L. J.; Alford, J. M. *J. Am. Chem. Soc.* **2003**, *125*, 5471-5478.

(108) Caravan, P.; Ellison, J. J.; McMurry, T. J.; Lauffer, R. B. *Chem. Rev.* **1999**, *99*, 2293-2352.

(109) Fukuda, Y.; Ando, K.; Ishikura, R.; Kotoura, N.; Tsuda, N.; Kato, N.; Yoshiya, S.; Nakao, N. *Magn Reson Med Sci* **2006**, *5*, 191-6.

(110) *Latest IMV market report shows MRI procedure growth slowing to 3% per year*, **2008.**

(111) Hendrick, R. E.; Haacke, E. M. *J. Magn. Reson. Imaging* **1993**, *3*, 137-148.

(112) Bean, C. P.; Livingston, J. D. *J. Appl. Phys.* **1959**, *30*, 120-129.

(113) Lauffer, R. B. *Chem. Rev.* **1987**, *87*, 901-27.

(114) Månsson, S.; Bjørnerud In *The chemistry of contrast agents in medical magnetic resonance imaging*; Merbach, A. E. a. T., Éva, Ed.; Wiley: Chichester ; New York, 2001, p 1-43.

(115) Bulte, J. W. M.; Kraitchman, D. L. *NMR Biomed.* **2004**, *17*, 484-499.

(116) Liu, W.; Frank, J. A. *Eur. J. Radiol.* **2009**, *70*, 258-264.

(117) Cacheris, W. P.; Quay, S. C.; Rocklage, S. M. *Magn. Reson. Imaging* **1990**, *8*, 467-481.

(118) Olsvik, O.; Popovic, T.; Skjerve, E.; Cudjoe, K. S.; Hornes, E.; Ugelstad, J.; Uhlen, M. *Clin. Microbiol. Rev.* **1994**, *7*, 43-54.

(119) Holt, J. K.; Park, H. G.; Wang, Y.; Stadermann, M.; Artyukhin, A. B.; Grigoropoulos, C. P.; Noy, A.; Bakajin, O. *Science* **2006**, *312*, 1034-1037.

(120) Ananta, J. S.; Matson, M. L.; Tang, A. M.; Mandal, T.; Lin, S.; Wong, K.; Wong, S. T.; Wilson, L. J. *J. Phys. Chem. C* **2009**, *113*, 19369-19372.

(121) Ananta, J. S.; Matson, M. L.; Tang, A. M.; Mandal, T.; Lin, S.; Wong, S. T.; Wong, K.; Wilson, L. J. *J. Phys. Chem.C.* **2009**, *113*, 19369-19372.

(122) Sithararnan, B.; Wilson, L. J. *Int. J. Nanomedicine* **2006**, *1*, 291-295.

(123) Laus, S.; Sitharaman, B.; Toth, E.; Bolskar, R. D.; Helm, L.; Wilson, L. J.; Merbach, A. E. *J. Phys. Chem. C* **2007**, *111*, 5633-5639.

(124) Sitharaman, B.; Bolskar, R. D.; Rusakova, I.; Wilson, L. J. *Nano Lett.* **2004**, *4*, 2373-2378.

(125) Toth, E.; Bolskar, R. D.; Borel, A.; Gonzalez, G.; Helm, L.; Merbach, A. E.; Sitharaman, B.; Wilson, L. J. *J. Am. Chem. Soc.* **2005**, *127*, 799-805.

(126) Bertini, I.; Galas, O.; Luchinat, C.; Parigi, G. *Journal of Magnetic Resonance Series A* **1995**, *113*, 151-158.

(127) Sitharaman, B.; Tran, L. A.; Pham, Q. P.; Bolskar, R. D.; Muthupillai, R.; Flamm, S. D.; Mikos, A. G.; Wilson, L. J. *Contrast Media Mol. Imaging* **2007**, *2*, 139-146.

(128) Stevenson, S.; Stephen, R. R.; Amos, T. M.; Cadorette, V. R.; Reid, J. E.; Phillips, J. P. *J. Am. Chem. Soc.* **2005**, *127*, 12776-12777.

(129) Lu, J.; Sabirianov, R. F.; Mei, W. N.; Gao, Y.; Duan, C. G.; Zeng, X. C. *J. Phys. Chem. B* **2006**, *110*, 23637-23640.

(130) Stevenson, S.; Phillips, J. P.; Reid, J. E.; Olmstead, M. M.; Rath, S. P.; Balch, A. L. *Chem. Commun.* **2004**, 2814-2815.

(131) MacFarland, D. K.; Walker, K. L.; Lenk, R. P.; Wilson, S. R.; Kumar, K.; Kepley, C. L.; Garbow, J. R. *J. Med. Chem.* **2008**, *51*, 3681-3683.

(132) Hartman, K. B.; Laus, S.; Bolskar, R. D.; Muthupillai, R.; Helm, L.; Toth, E.; Merbach, A. E.; Wilson, L. J. *Nano Lett.* **2008**, *8*, 415-419.

(133) Tannock, I. F.; Rotin, D. *Cancer Res.* **1989**, *49*, 4373-4384.

(134) Sitharaman, B.; Wilson, L. J. *J. Biomed. Nanotechnol.* **2007**, *3*, 342-352.

(135) Striolo, A. *Nano Lett.* **2006**, *6*, 633-639.

(136) Jankovski, A.; Raftopoulos, C.; Vaz, G.; Hermoye, L.; Cosnard, G.; Francotte, F.; Duprez, T. *JBR-BTR* **2007**, *90*, 249-251.

(137) McDermott, R.; Lee, S. K.; ten Haken, B.; Trabesinger, A. H.; Pines, A.; Clarke, J. *Proc. Natl. Acad. Sci. U. S. A.* **2004**, *101*, 7857-7861.

(138) Mansfield, P. *Angewandte Chemie-International Edition* **2004**, *43*, 5456-5464.

(139) Mackeyev, Y.; Hartman, K. B.; Ananta, J. S.; Lee, A. V.; Wilson, L. J. *J. Am. Chem. Soc.* **2009**, *131*, 8342-8345.

(140) Langer, M.; Kratz, F.; Rothen-Rutishauser, B.; Wunderli-Allenspach, H.; Beck-Sickinger, A. G. *J. Med. Chem.* **2001**, *44*, 1341-1348.

(141) Mackeyev, Y.; Hartman, K. B.; Ananta, J. S.; Lee, A. V.; Wilson, L. J. *J. Am. Chem. Soc.* **2009**, *131*, 8342-8343.

(142) Hassan, A. A.; Chan, B. T.; Tran, L. A.; Hartman, K. B.; Ananta, J. S.; Mackeyev, Y.; Hu, L.; Pautler, R. G.; Wilson, L. J.; Lee, A. V. *Contrast Media Mol. Imaging* **2009**, (accepted).

(143) Moskowitz, B. M. In *Environmental Magnetism Workshop* Institute for Rock Magnetism, **1991**; Vol. 1.

(144) McElfresh, M.; 1 ed.; Quantum Design, Inc.: San Diego, CA, 1994; Vol. 1.

(145) Kittel, C. *Reviews of Modern Physics* **1949**, *21*, 541.

(146) Jiles, D.; Atherton, D. *Magnetics, IEEE Transactions on* **1983**, *19*, 2183-2185.

(147) Neel, L. *Ann. Geophys* **1949**, *5*, 99.

(148) Sitharaman, B.; Kissell, K. R.; Hartman, K. B.; Tran, L. A.; Baikalov, A.; Rusakova, I.; Sun, Y.; Khant, H. A.; Ludtke, S. J.; Chiu, W.; Laus, S.; Toth, E.; Helm, L.; Merbach, A. E.; Wilson, L. J. *Chem. Commun. (Cambridge, U. K.)* **2005**, 3915-3917.

(149) Kumar, D.; Narayan, J.; Kvit, A.; Sharma, A.; Sankar, J. *J. Magn. Magn. Mater.* **2001**, *232*, 161-167.

(150) Wen, J. Z.; Richter, H.; Green, W. H.; Howard, J. B.; Treska, M.; Jardim, P. M.; Vander Sande, J. B. *J. Mater. Chem.* **2008**, *18*, 1561-1569.

(151) Choi, J. H.; Nguyen, F. T.; Barone, P. W.; Heller, D. A.; Moll, A. E.; Patel, D.; Boppart, S. A.; Strano, M. S. *Nano Lett.* **2007**, *7*, 861-867.

(152) Jung, C. W.; Jacobs, P. *Magn. Reson. Imaging* **1995**, *13*, 661-674.

(153) Shen, T.; Schwarz, R.; Thompson, J. *J. Appl. Phys.* **1999**, *85*, 4110.

(154) Bowles, J.; Jackson, M.; Chen, A.; Solheid, P. *The IRM Quarterly* **2009**, *19*, 12.

(155) Mitric, M.; Onnerud, P.; Rodic, D.; Tellgren, R.; Szytula, A.; Napijalo, M. L. *J. Phys. Chem. Solids* **1993**, *54*, 967-972.

(156) Kato, H.; Kanazawa, Y.; Okumura, M.; Taninaka, A.; Yokawa, T.; Shinohara, H. *J. Am. Chem. Soc.* **2003**, *125*, 4391-4397.

(157) Funasaka, H.; Sugiyama, K.; Yamamoto, K.; Takahashi, T. *J. Phys. Chem.C* **1995**, *99*, 1826-1830.

(158) Hifumi, H.; Yamaoka, S.; Tanimoto, A.; Citterio, D.; Suzuki, K. *J. Am. Chem. Soc.* **2006**, *128*, 15090-15091.

(159) Rieter, W. J.; Taylor, K. M. L.; An, H.; Lin, W. *J. Am. Chem. Soc.* **2006**, *128*, 9024-9025.

(160) Grobner, T. *Nephrol. Dial. Transplant.* **2006**, *21*, 1104-1108.

(161) Administration, U. S. F. a. D., Ed. 2006.

(162) Cowper, S. E.; Robin, H. S.; Steinberg, S. M.; Su, L. D.; Gupta, S.; LeBoit, P. E. *The Lancet* **2000**, *356*, 1000-1001.

(163) Pering, C. Gaithersburg, MD, **2009**.

(164) Administration, U. S. F. a. D., Ed. **2006**.

(165) In *FDA News Release*; U. S. Food and Drug Administration: **2007**.

(166) Kanal, E.; Broome, D. R.; Martin, D. R.; Thomsen, H. S. *Radiology* **2008**, *246*, 11-14.

(167) Idée, J.-M.; Port, M.; Raynal, I.; Schaefer, M.; Le Greneur, S.; Corot, C. *Fundam. Clin. Pharmacol.* **2006**, *20*, 563-576.

(168) Cacheris, W. P.; Nickle, S. K.; Sherry, A. D. *Inorg. Chem.* **1987**, *26*, 958-960.

(169) Medicines and Healthcare products Regulatory Agency (MHRA): **2007**; Vol. 2011.

(170) Lahiri, S.; Mukhopadhyay, B.; Das, N. *J. Radioanal. Nucl. Chem.* **1997**, *221*, 167-171.

(171) Sveshnikova, E.; Lanin, V.; Krutineva, E.; Ermolaev, V. *Optics and Spectroscopy* **2000**, *89*, 360-368.

(172) Zhang, D. S.; Ma, B. Q.; Jin, T. Z.; Gao, S.; Yan, C. H.; Mak, T. C. W. *New J. Chem.* **2000**, *24*, 61-62.

(173) Cornia, A.; Gatteschi, D.; Hegetschweiler, K.; Hausherr-Primo, L.; Gramlich, V. *Inorg. Chem.* **1996**, *35*, 4414-4419.

(174) Ferrari, M. *Nat. Rev. Cancer* **2005**, *5*, 161-171.

(175) Freeman, A.; Mayhew, E. *Cancer* **1986**, *58*, 573 - 583.

(176) Mulford, D. A.; Scheinberg, D. A.; Jurcic, J. G. *J. Nucl. Med.* **2005**, *46*, 199S.

(177) Goldenberg, D. M. *J. Nucl. Med.* **2002**, *43*, 693.

(178) Hirsch, A. *Angewandte Chemie* **2002**, *41*, 1853-1859.

(179) Bahr, J. L.; Yang, J.; Kosynkin, D. V.; Bronikowski, M. J.; Smalley, R. E.; Tour, J. M. *J. Am. Chem. Soc.* **2001**, *123*, 6536-6542.

(180) Georgakilas, V.; Kordatos, K.; Prato, M.; Guldi, D. M.; Holzinger, M.; Hirsch, A. *J. Am. Chem. Soc.* **2002**, *124*, 760-761.

(181) Georgakilas, V.; Tagmatarchis, N.; Pantarotto, D.; Bianco, A.; Briand, J.-P.; Prato, M. *Chem. Commun.* **2002**, 3050-3051.

(182) Ballangrud, Å. M.; Yang, W. H.; Palm, S.; Enmon, R.; Borchardt, P. E.; Pellegrini, V. A.; McDevitt, M. R.; Scheinberg, D. A.; Sgouros, G. *Clin. Cancer Res.* **2004**, *10*, 4489.

(183) Milenic, D. E.; Brechbiel, M. W. *Cancer Biol. Ther.* **2004**, *3*, 361-370.

(184) Humm, J. *International Journal of Radiation Oncology* **1987**, *13*, 1767-1773.

(185) Deal, K. A.; Davis, I. A.; Mirzadeh, S.; Kennel, S. J.; Brechbiel, M. W. *J. Med. Chem.* **1999**, *42*, 2988-2992.

(186) Cole, W. C.; DeNardo, S. J.; Meares, C. F.; McCall, M. J.; DeNardo, G. L.; Epstein, A. L.; O'Brien, H. A.; Moi, M. K. *J. Nucl. Med.* **1987**, *28*, 83.

(187) Kelly, M. P.; Lee, F. T.; Smyth, F. E.; Brechbiel, M. W.; Scott, A. M. *J. Nucl. Med.* **2006**, *47*, 716-725.

(188) Davis, I.; Glowienka, K.; Boll, R.; Deal, K.; Brechbiel, M.; Stabin, M.; Bochsler, P.; Mirzadeh, S.; Kennel, S. *Nucl. Med. Biol.* **1999**, *26*, 581-589.

(189) Choppin, G. R.; Rizkalla, E. N. *Handbook on the Physics and Chemistry of Rare Earths* **1994**, *18*, 559-590.

(190) Fantini, C.; Pimenta, M.; Strano, M. *J. Phys. Chem.C.* **2008**, *112*, 13150-13155.

(191) Hamisch, Y. *Medica Mundi* **2003**, *47*, 18-27.

(192) Levin, C. S.; Hoffman, E. J. *Phys Med Biol* **1999**, *44*, 781-99.

(193) Qaim, S. M.; Bisinger, T.; Hilgers, K.; Nayak, D.; Coenen, H. H. *Radiochim. Acta* **2007**, *95*, 67-73.

(194) Budinger, T. F.; Derenzo, S. E.; Huesman, R. H. *Ann. Neurol.* **1984**, *15*, 35-43.

(195) Cherry, S. R.; Louie, A. Y.; Jacobs, R. E. *Proc. IEEE* **2008**, *96*, 416-438.

(196) Schoder, H.; Gonen, M. *J. Nucl. Med.* **2007**, *48*, 4S-18S.

(197) Tidwell, A. S.; Jones, J. C. *Clin Tech Small Anim Pract* **1999**, *14*, 65-111.

(198) Sharma, T. *J. Clin. Invest.* **2003**, *112*, 10-18.

(199) Jacobs, R. E.; Cherry, S. R. *Curr. Opin. Neurobiol.* **2001**, *11*, 621-629.

(200) Service, R. F. *Science* **1996**, *272*, 1423.

(201) Hayakawa, N.; Uemura, K.; Ishiwata, K.; Shimada, Y.; Ogi, N.; Nagaoka, T.; Toyama, H.; Oda, K.; Tanaka, A.; Endo, K.; Senda, M. *Nucl Med Biol* **2000**, *27*, 121-5.

(202) Agger, R.; Petersen Mikkel, S.; Petersen Charlotte, C.; Hansen Soren, B.; Stodkilde-Jorgensen, H.; Skands, U.; Blankenstein, T.; Andersen Tom, E.; Hulgaard Egil, F.; Jorgensen Jan, T.; Marqversen, J.; Gundersen Hans, J. G.; Hokland Marianne, E. *J Immunother* **2007**, *30*, 29-39.

(203) Agger, R.; Petersen, M. S.; Petersen, C. C.; Hansen, S. B.; Stødkilde-Jørgensen, H.; Skands, U.; Blankenstein, T.; Andersen, T. E.; Hulgaard, E. F.; Jørgensen, J. T. *J. Immunother.* **2007**, *30*, 29.

(204) Cherry, S. R. *Annu. Rev. Biomed. Eng.* **2006**, *8*, 35-62.

(205) Raylman, R. R.; Hammer, B. E.; Christensen, N. L. *Nuclear Science, IEEE Transactions on* **1996**, *43*, 2406-2412.

(206) Shen, D.; Liu, D.; Cao, Z.; Acton Paul, D.; Zhou, R. *Mol Imaging Biol* **2007**, *9*, 24-31.

(207) Babinec, P.; Babincova, M. *Med. Hypotheses* **2007**, *69*, 703-704.

(208) Cherry, S. R.; Louie, A. Y.; Jacobs, R. E. *Proceedings of the IEEE* **2008**, *96*, 416-438.

(209) Mackeyev, Y. A.; Marks, J. W.; Rosenblum, M. G.; Wilson, L. J. *J. Phys. Chem. B* **2005**, *109*, 5482-5484.

(210) Campbell, M. M.; Johnson, G. *Chem. Rev.* **1978**, *78*, 65-87.

(211) Cherukuri, P.; Gannon, C. J.; Leeuw, T. K.; Schmidt, H. K.; Smalley, R. E.; Curley, S. A.; Weisman, R. B. *Proc. Natl. Acad. Sci. U. S. A.* **2006**, *103*, 18882-18886.

(212) Zavaleta, C.; de la Zerda, A.; Liu, Z.; Keren, S.; Cheng, Z.; Schipper, M.; Chen, X.; Dai, H.; Gambhir, S. S. *Nano Lett.* **2008**, *8*, 2800-2805.

(213) Liu, Z.; Cai, W.; He, L.; Nakayama, N.; Chen, K.; Sun, X.; Chen, X.; Dai, H. *Nat*

Nano **2007**, *2*, 47-52.

(214) Yang, S.; Guo, W.; Lin, Y.; Deng, X.; Wang, H.; Sun, H.; Liu, Y.; Wang, X.; Wang, W.; Chen, M. *J. Phys. Chem.C.* **2007**, *111*, 17761-17764.

(215) Wang, H.; Wang, J.; Deng, X.; Sun, H.; Shi, Z.; Gu, Z.; Liu, Y.; Zhaoc, Y. *J. Nanosci. Nanotechnol.* **2004**, *4*, 1019-1024.

(216) Singh, R.; Pantarotto, D.; Lacerda, L.; Pastorin, G.; Klumpp, C.; Prato, M.; Bianco, A.; Kostarelos, K. *Proc. Natl. Acad. Sci. U. S. A.* **2006**, *103*, 3357.

(217) Iyer, A. K.; Khaled, G.; Fang, J.; Maeda, H. *Drug Discov. Today* **2006**, *11*, 812-818.

(218) Obata, A.; Kasamatsu, S.; McCarthy, D. W.; Welch, M. J.; Saji, H.; Yonekura, Y.; Fujibayashi, Y. *Nucl. Med. Biol.* **2003**, *30*, 535-539.

(219) Obata, A.; Yoshimi, E.; Waki, A.; Lewis, J. S.; Oyama, N.; Welch, M. J.; Saji, H.; Yonekura, Y.; Fujibayashi, Y. *Ann. Nucl. Med.* **2001**, *15*, 499-504.

(220) Husebo Lars, O.; Sitharaman, B.; Furukawa, K.; Kato, T.; Wilson Lon, J. *J Am Chem Soc* **2004**, *126*, 12055-64.

(221) Fenton, H. J. H. *Journal of the Chemical Society, Transactions* **1894**, *65*, 899-910.

(222) Vaghjiani, G. L.; Turnipseed, A. A.; Warren, R. F.; Ravishankara, A. R. *Photodissociation of H2O2 at 193 and 222 nm: Products and quantum yields*; AIP, 1992; Vol. 96.

(223) Katsumata, H.; Kawabe, S.; Kaneco, S.; Suzuki, T.; Ohta, K. *Journal of Photochemistry and Photobiology A: Chemistry* **2004**, *162*, 297-305.

(224) Legrini, O.; Oliveros, E.; Braun, A. M. *Chem. Rev.* **1993**, *93*, 671-698.

(225) Koppenol, W. H.; Liebman, J. F. *The Journal of Physical Chemistry* **1984**, *88*, 99-101.

(226) Pan, H.; Liu, L.; Guo, Z.-X.; Dai, L.; Zhang, F.; Zhu, D.; Czerw, R.; Carroll, D. L. *Nano Lett.* **2002**, *3*, 29-32.

(227) López-Cueto, G.; Ostra, M.; Ubide, C.; Zuriarrain, J. *Anal. Chim. Acta* **2004**, *515*, 109-116.

(228) Walling, C. *Acc. Chem. Res.* **1975**, *8*, 125-131.

(229) Li, W.; Bai, Y.; Zhang, Y.; Sun, M.; Cheng, R.; Xu, X.; Chen, Y.; Mo, Y. *Synth. Met.* **2005**, *155*, 509-515.

(230) U.S. Peroxide, L.; U.S. Peroxide, LLC: October 21 2009; Vol. 2011.

(231) Zhang, P.; Pan, H.; Liu, D.; Guo, Z. X.; Zhang, F.; Zhu, D. *Synth. Commun.* **2003**, *33*, 2469-2474.

(232) Pan, H.; Liu, L.; Guo, Z.-X.; Dai, L.; Zhang, F.; Zhu, D.; Czerw, R.; Carroll, D. L. *Nano Lett.* **2003**, *3*, 29-32.

(233) Cotton, F. A.; Wilkinson, G.; Murillo, C.; Bochmann, M. *Advanced Inorganic Chemistry*; 6 ed.; John Wiley: New York City, New York, 2003.

(234) Kodera, M.; Kita, T.; Miura, I.; Nakayama, N.; Kawata, T.; Kano, K.; Hirota, S. *J. Am. Chem. Soc.* **2001**, *123*, 7715-7716.

(235) Ottaviani, M. F.; Bossmann, S.; Turro, N. J.; Tomalia, D. A. *J. Am. Chem. Soc.* **1994**, *116*, 661-671.

(236) Corzilius, B.; Dinse, K. P.; Hata, K. *Phys. Chem. Chem. Phys.* **2007**, *9*, 6063-6072.

(237) Tarabek, J.; Kavan, L.; Kalbac, M.; Rapta, P.; Zukalová, M.; Dunsch, L. *Carbon* **2006**, *44*, 2147-2154.

(238) Hodgson, D. J. *Prog. Inorg. Chem.* **1975**, 173-241.

(239) Haddad, M.; Hendrickson, D. *Inorg. Chim. Acta* **1978**, *28*, 121-122.

(240) Nelson Juan, F.; Harold, C. *Journal of Inorganic and Nuclear Chemistry* **1979**, *41*, 1643-1645.

(241) Karlin, K. D.; Wei, N.; Jung, B.; Kaderli, S.; Niklaus, P.; Zuberbuehler, A. D. *J. Am. Chem. Soc.* **1993**, *115*, 9506-9514.

(242) Piquemal, J. P.; Pilmé, J. *Journal of Molecular Structure: THEOCHEM* **2006**, *764*, 77-86.

(243) Halfen, J. A.; Mahapatra, S.; Wilkinson, E. C.; Kaderli, S.; Young, V. G.; Que, L.; Zuberbühler, A. D.; Tolman, W. B. *Science* **1996**, *271*, 1397.

(244) Diedrich, C.; Deeth, R. J. *Inorg. Chem.* **2008**, *47*, 2494-2506.

(245) Bencini, A.; Benelli, C.; Caneschi, A.; Carlin, R. L.; Dei, A.; Gatteschi, D. *J. Am. Chem. Soc.* **1985**, *107*, 8128-8136.

(246) LaGraffe, D.; Dowben, P. A.; Onellion, M. *Phys. Rev. B* **1989**, *40*, 3348.